11/4-12-94 SD

CONTRACTOR REPORT

SAND94—0095
Unlimited Release
UC—237

Detail Design of A 10.4-m Stretched-Membrane Dish

Phase II, Final Report

Solar Kinetics, Inc.
10635 King William Drive
Dallas, TX 10635

Prepared by Sandia National Laboratories Albuquerque, New Mexico 87185 and Livermore, California 94550 for the United States Department of Energy under Contract DE-AC04-94AL85000

Printed January 1994

Issued by Sandia National Laboratories, operated for the United States Department of Energy by Sandia Corporation.

Printed in the United States of America. This report has been reproduced directly from the best available copy.

Available to DOE and DOE contractors from
Office of Scientific and Technical Information
PO Box 62
Oak Ridge, TN 37831

Prices available from (615) 576-8401, FTS 626-8401

Available to the public from
National Technical Information Service
US Department of Commerce
5285 Port Royal Rd
Springfield, VA 22161

NTIS price codes
Printed copy: A08
Microfiche copy: A01

Distribution
Category UC-237

SAND94-0095
Unlimited Release
Printed January 1994

DETAIL DESIGN OF A 10.4-m STRETCHED-MEMBRANE DISH

Phase II, Final Report

Solar Kinetics, Inc.
10635 King William Drive
Dallas, TX 10635

Sandia Contract 55-2465

ABSTRACT

This report describes efforts conducted under Tasks 3 and 4 of the second phase of the project to develop a single-element stretched-membrane dish concept to reduce the cost of a high-performance concentrating solar collector. We completed the detailed design for such a collector suitable to drive a 25-kWe Stirling motor generator. The design includes the collectors, optical element, the drive, and support systems. The aperture of the optical element was sized to provide the required energy to the engine based on test data and analytical models of the concentrator receiver, and engine. The design of the optical element was improved based on experience gained from the design, fabrication, and testing of several prototypes.

ACKNOWLEDGMENT

This work was funded by the Department of Energy (DOE) through Sandia national Laboratories (SNL) under contract number 55-2495. Solar Kinetics, Inc. (SKI) would like to thank the many individuals who provided assistance at various stages of this project. In particular, we would like to thank Dr. Thomas Mancini for his support, guidance, and patience during the conduct of this work. His vision and perseverance during all previous phases of this effort materially contributed to the advancement of stretched-membrane technology for solar concentrators.

Timothy Wendelin of the National Renewable Energy Laboratories (NREL) was also very helpful in the analysis of SKI's development work.

Table of Contents

(Section 6.0 - Continued)

List of Figures

(Section 6.0 - Continued)

List of Tables

1.0 Introduction

1.1 Purpose and Goals

The single-element, stretched-membrane dish concept has been proposed as a means to reduce the cost of high-performance concentrating solar collectors. Sandia National Laboratories (SNL) first contracted with Solar Kinetics, Inc. (SKI) in 1986 to begin evaluation of issues relevant to implementing this approach. This investigation has included initial analytical and small-scale experiments, fabrication of a scaled operational optical element, and a complete, detailed design for a 60 kW thermal collector.

This report describes efforts conducted under Tasks 3 and 4 of the second phase of the project. The goal of these tasks was to complete a design for a stretched-membrane, single-element concentrating collector suitable for driving a 25 kWe Stirling motor generator. This work included design of both the optical element and its drive and support systems. The optical-element aperture was sized to provide the required energy to the engine based upon test data and analytical models of the concentrator, receiver, and engine. The design of the optical element was improved based upon experience gained from the design, fabrication, and testing of the previous prototypes. The drive and support systems were conceptualized, refined, and designed in detail.

1.2 Prior Work on Stretched-Membrane Concentrating Dishes

In Phase I and the first two tasks of Phase II, considerable fundamental development was accomplished to define the important relationships necessary to design and fabricate a stretched-membrane concentrating mirror (1, 2). Suitable materials for the membranes and support structure were investigated and tested. Many critical approaches to the design of the optical element and the tooling used to build it were conceptualized, analyzed, and demonstrated.

Five major technical issues were successfully addressed.

1. The technique of free-forming a large-scale membrane was shown to be predictable, accurate, and repeatable. This was demonstrated at three scales: 1.4-m, 3.7-m, and 7-m diameter. This forming process results in a controlled and repeatable membrane contour by independently controlling uniform and non-uniform forming loads on the membrane.

2. A tensioned hub-and-spoke structure to support the formed membrane was designed and demonstrated. The innovative, bicycle-wheel-like structure achieved both high stiffness and manufacturing simplicity.

3. The use of a separate reflective polymer membrane was demonstrated. It is intended that this membrane be readily replaceable in the field. This will allow periodic renewal of the reflective surface properties and improve performance and the cost-effectiveness of the dish.

4. A technique to ship parabolic membranes by rolling them onto a custom contoured mandrel was developed. This allows the critical forming operation to be performed in the controlled environment of a factory. The mandrel with the membrane is then shippable by standard container to the field assembly site.

5. High levels of optical performance of the 7-m optical element were demonstrated by measurements taken at the National Solar Thermal Test Facility (NSTTF). Peak concentration of 5200 suns and effective RMS slope error of 2.3 mrad were measured (3).

In Phase I and the first half of Phase II, all work involved only formed membranes and membranes fabricated at reduced scale. No tracking drive mechanism, controls, or support structure were developed beyond preliminary conceptual approaches.

In Task 2, a 7-m diameter operational prototype was designed and built. The optical element's size was selected as limited primarily by available manufacturing facilities. The unit was built and tested in SKI's Dallas facility and then disassembled and re-erected at the NSTTF. Three 7-m membranes were fabricated, formed, and tested in this effort. The optical element is mounted on a modified heliostat drive by means of a prototypical adapter assembly. This approach was intended for testing purposes only.

1.3 Limitations and Assumptions

Some specific limitations on the scope of the current work were defined when work began. The successful design of the 7-m optical element was to be used as a baseline for design of the larger dish. Substantial design changes, which would require major development efforts, would be avoided if possible. No new wind load data would be generated by scale-model testing or full-size dish instrumentation. Existing published data would be reviewed and the best source of wind load information selected for the dish design.

The fabrication would adhere to the AISC code for member sizing. All weld joints would have a minimum safety factor of 5, per SNL requirement. Factors of safety greater than those specified in the AISC code would be applied to specific components whose loads were less well defined. This limitation was derived from the perceived uncertainty of the wind load data as applied to this specific structure.

The design would utilize processes and techniques that are common to the metal fabricating industry wherever possible. Attention would be continually paid to minimizing the field time and labor required to assemble and erect the dish.

The foundation design would be calculated for soil conditions at the NSTTF. Existing soil test data would be utilized.

1.4 Design Description

The design for a 60 kWe dish collector has a reflective aperture diameter of 10.4-m (85 sq.m.). Total thermal power of 60 kW will be concentrated at the focal point based upon anticipated optical performance. Information from researchers at SNL and developers of Stirling Thermal Motors' kinematic Stirling motor indicates that this will be adequate to provide 25 kWe of electrical power.

The systems, which make up the collector, are the optical element, the Power Conversion Assembly (PCA), the PCA support, the drive, the support pylon, the foundation, and the tracking and focus controls (see Figure 1.1). The design specifications are summarized in Table 1.1.

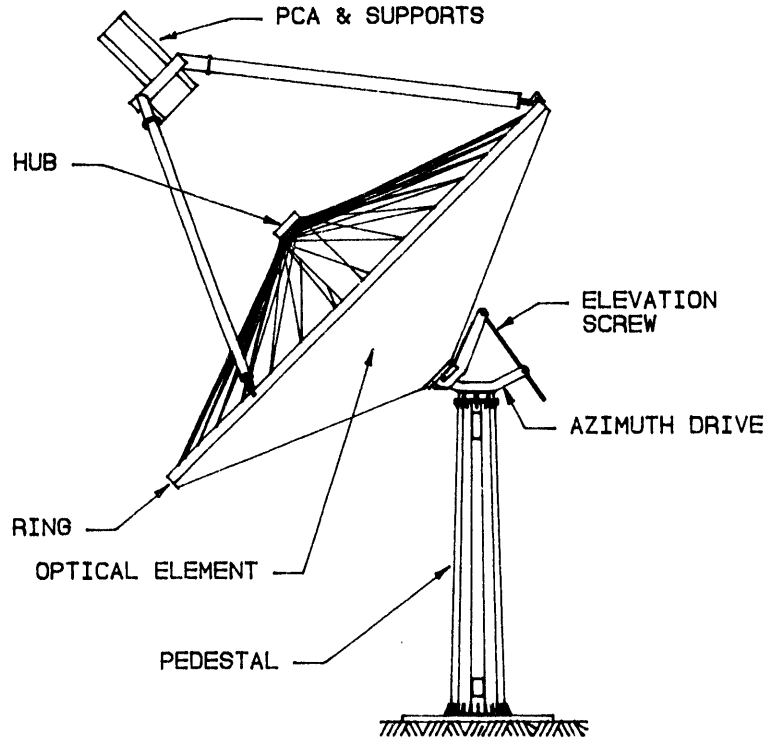

Figure 1.1 Complete 10.4 M Stretched-Membrane Collector System.

The support pylon consists of a single-hollow steel pedestal with a flange at its top and bottom. The bottom flange fastens to anchors in the concrete foundation. The top flange supports a drive mechanism consisting of an azimuth stage under a separate elevation drive.

When referring to components of the stretched-membrane dish, the references to "front" and "rear" will mean towards the sun and away from the sun, respectively.

The optical element design is patterned very closely after the successful 7-m prototype optical element developed by SKI (2, 3). The structure is similar to a bicycle wheel. Refer to Figure 1.2 for an exploded view of the optical element. There are two sets of pretensioned spokes (32 front and 32 rear) with one end attached to a central hub and the other ends attached to a large circular rim or ring. A parabolic, contoured membrane is attached at its periphery to the ring. The membrane is stretched across the space in between the two sets of spokes. The central hub passes through a hole in the center of this membrane. A rear membrane is draped across the outside of the rear set of spokes. The two membranes form a hollow plenum, which is evacuated with a small blower. The light, negative pressure creates a pressure differential across both membranes. The front membrane is stabilized in the parabolic shape to which it was originally formed. The rear membrane is drawn taught over the rear spokes causing a catenary spoke displacement in each rear spoke.

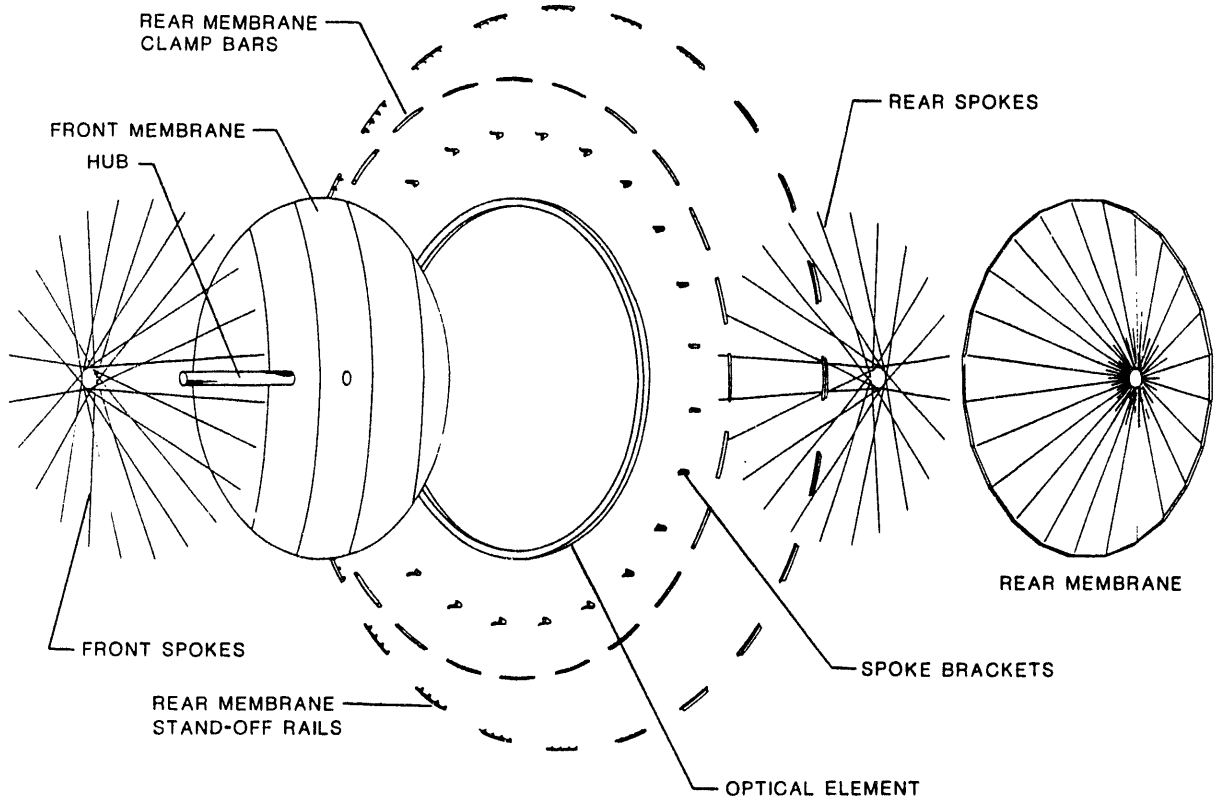

Figure 1.2 Optical-Element Construction, Exploded View.

The drive is similar to the heliostat drive developed by Peerless-Winsmith for SNL (4). The greater overturning loads for the stretched-membrane dish require a larger diameter casting than that used for the heliostat drive. A plano-centric gear reducer is used for the azimuth stage that supports the elevation stage. The elevation drive is a motorized ball screw attached directly to a lever arm on the optical-element hub.

The support pylon and foundation designs are similar to those used for the faceted stretched-membrane dish (5). The pylon is a tapered, faceted tube of plain carbon steel with top and bottom flanges. Handholes for service access are included. The foundation is a poured-in-place concrete pier with a monolithic apron at ground level. The concrete is steel reinforced with anchor bolts cast-in-place to secure the pylon base flange.

Controls are required for maintaining the stabilization vacuum in the optical-element plenum and to operate the tracking motors for pointing the dish at the sun. The vacuum is maintained with a small, variable speed fan controlled by a differential pressure transducer. The tracking control uses DC servo motors with encoder feedback. Dish position is determined by ephemeral calculations based on the time of day, time of year, and geographic location of the dish. The tracking control logic was developed at SNL and is licensed for commercial manufacture (6). The logic includes compensation for support structure misalignment and gravity deflections, which are often a function of the elevation angle of the dish.

1.5 Reflective Membrane Field Replacement

In parallel with the design work, some additional development and demonstration of reflective membrane field replacement was also completed in this part of the project. A dual-film membrane was fabricated and installed on the dish in the field. The planning and the implementation of the installation procedures were educational as to the types of difficulties that should be anticipated for future operations. The membrane was successfully installed after surmounting several unanticipated field problems. The reflective film suffered a seam failure only a few weeks after installation, (unrelated to the installation difficulties). Improved techniques for membrane installation have been defined. Additional work is still required in specifying and demonstrating suitable materials for long-lived reflective films, however.

This report describes the detailed design of a commercial-scale, single-element stretched-membrane dish. This dish builds on the experience gained in earlier stages where the membrane forming technique was developed and a 7-m prototype optical element was successfully demonstrated. The dish support concept has been reviewed; the entire dish has been designed; and production costs have been estimated.

Table 1.1
Design Specifications for 10.4-M
Stretched-Membrane Collector System

PERFORMANCE		
Electrical Power Rating	25 kW	
Thermal power into receiver (net)	60 kW	
GEOMETRY		
Reflective aperture outer diameter	10.4 m	
Gross aperture area	85 sq.m.	
f:d ratio	0.6	
Stow position	facing zenith	
Predicted receiver aperture diameter	0.26 m	
ENVIRONMENT		
Peak design wind speed, stow position	145 km/hr	(90 mph)
Peak design wind speed, any orientation	80 km/hr	(50 mph)
Maximum wind speed with no performance effect	43 km/hr	(27 mph)
MEMBRANES		
Formed-metal membrane	0.3 mm (0.012") thick, stainless steel	
Reflective-membrane fixturing	vacuum retained	
Reflective-membrane material	front-surface silver metallized PET w/ acrylic over coat.	
Top transparent film	0.05 mm (0.002") thick FEP Teflon (TM)	
Rear membrane	PVC coated polyester cloth.	
MATERIALS OF CONSTRUCTION		
structure material	low carbon structural steel	
spokes	4140 alloy steel	
finish	hot dip galvanizing	
CONTROLS		
Open Loop		
CODES		
AISC		
Factor of safety on welds	>5.0	

COMPONENT WEIGHTS

Optical element	3876 kg	(8547 lbs)
PCA support structure	1069 kg	(2358 lbs)
PCA	635 kg	(1400 lbs)
Drive	1043 kg	(2300 lbs)
Support pylon	1218 kg	(2685 lbs)
Total excluding Drive & PCA	6163 kg	(13590 lbs)
	72.5 kg/m^2	(14.9 lbs/ft^2)

2.0 Design Criteria

The goal of the Single-Element Stretched-Membrane Dish Program is to develop a 25 kWe dish Stirling engine generating system. As the name implies, this effort has focused on developing a concentrating collector employing a monolithic reflector surface as opposed to a faceted design. The reflector surface is made of a plastically formed membrane instead of the more conventional glass-metal panels. The optical surface is provided by a separate, reflective polymer membrane.

2.1 General Design Criteria

Performance specifications of the engine/receiver system defined many of the performance goals that the concentrator had to achieve. Information concerning these values was obtained from SNL and Stirling Thermal Motors.

Generator output	25 kWe	
Engine efficiency, peak	40%	
Receiver operating temperature	750 °C	
Engine and receiver weight	635 kg	(1400 lbs)

Performance specifications common to several types of solar thermal systems have been developed by SNL and the solar industry. The following common requirements were adopted for this dish system:

Survival wind speed, stow position.	145 km/hr	(90 mph)
Survival wind speed, any orientation.	80 km/hr	(50 mph)
Operating wind speed w/o significant degradation of performance.	43 km/hr	(27 mph)

These specifications were adopted without analysis of their effect on levelized energy costs. To perform such an analysis on only a portion of the total system (i.e. the concentrator), would not have been informative because there are many interactive effects between the engine, receiver, and the concentrator that must be considered. (This is discussed further in Section 9.0 of this report.)

Structural requirements of the dish design were considered from two perspectives: deflection at operational conditions and stress at survival conditions. Where specific component deflections did not contribute to performance degradation, only stress was considered. Some components, once sized to withstand survival loads, were more than sufficiently stiff for operational conditions. Other components had to be sized to limit deflections to prevent degraded performance. The AISC code was used to define allowable

stresses in the structure. It was also used to check aspect ratios of compression members. In addition to this, a safety factor of at least 5 was used on all welds.

2.2 Wind Loads

Solar collector design must anticipate the effects of wind loads on the large areas they present from both an operational and a survival perspective. The prediction of wind loads on such complicated structures as parabolic concentrators does not lend itself to straight analytical solutions. Load measurements made on instrumented full- size collectors are not available. Measurements have been made on models in wind tunnels by researchers in the solar community and in the radar and telecommunication industry. Two sources of information were available to SKI from these industries, the Colorado State University (CSU) study (7) and the research performed by LTV (8). Because there are significant differences in the loads that these approaches predict, it was necessary to evaluate these carefully before selecting the design concentrator loads.

The LTV study used a scale model of a parabolic antenna with a back up structure. The structure was typical of a telecommunication antenna rather than the enclosed spokes of the stretched-membrane optical element. The consultant who assisted in reducing the wind tunnel data and applying it to the stretched-membrane dish suggested that the LTV results are likely conservative compared to the loads that the dish would actually see because of the differences in back-up structures (9). This consultant had several wind tunnel test results to choose from, all for telecommunication antennas. He recommended use of the LTV data because its rear structure was the most similar to the stretched-membrane dish. Details of the various wind tunnel models were not available. The consultant's opinion was based on many years of applying this data to various antenna structures. The LTV data is based on a uniform flow rather than a boundary layer profile. The LTV data are considered conservative by some designers because of the history of successful antenna designs based on them.

The CSU model was a parabolic dish with no rear structure other than the mounting strut. The rear surface followed a parabolic contour parallel to the front surface. The wind tunnel used by CSU was different than most in that it intentionally created a boundary layer along the surface the model was mounted to. This was intended to more realistically model the true conditions a collector experiences.

2.2.1 Comparison and Discussion of Wind Tunnel Data

Wind loads are necessary to select the dish mounting geometry even before the structural design is considered. To help select a wind load prediction approach, the forces and moments acting on the dish at various elevation and azimuth orientations were plotted and compared for the two methods.

Drag loads predicted with the two approaches are similar at low elevation angles (see Figure 2.1). Drag loads while pointed near the zenith are considerably different (LTV data 400% higher than CSU). This could be significant for a vertical stow orientation. The differences are likely to be due to the different rear structures and the wind velocity profiles. This difference indicates a design sensitivity to the rear structure configuration. This is even more significant because neither model's rear structure is the same as the stretched-membrane dish.

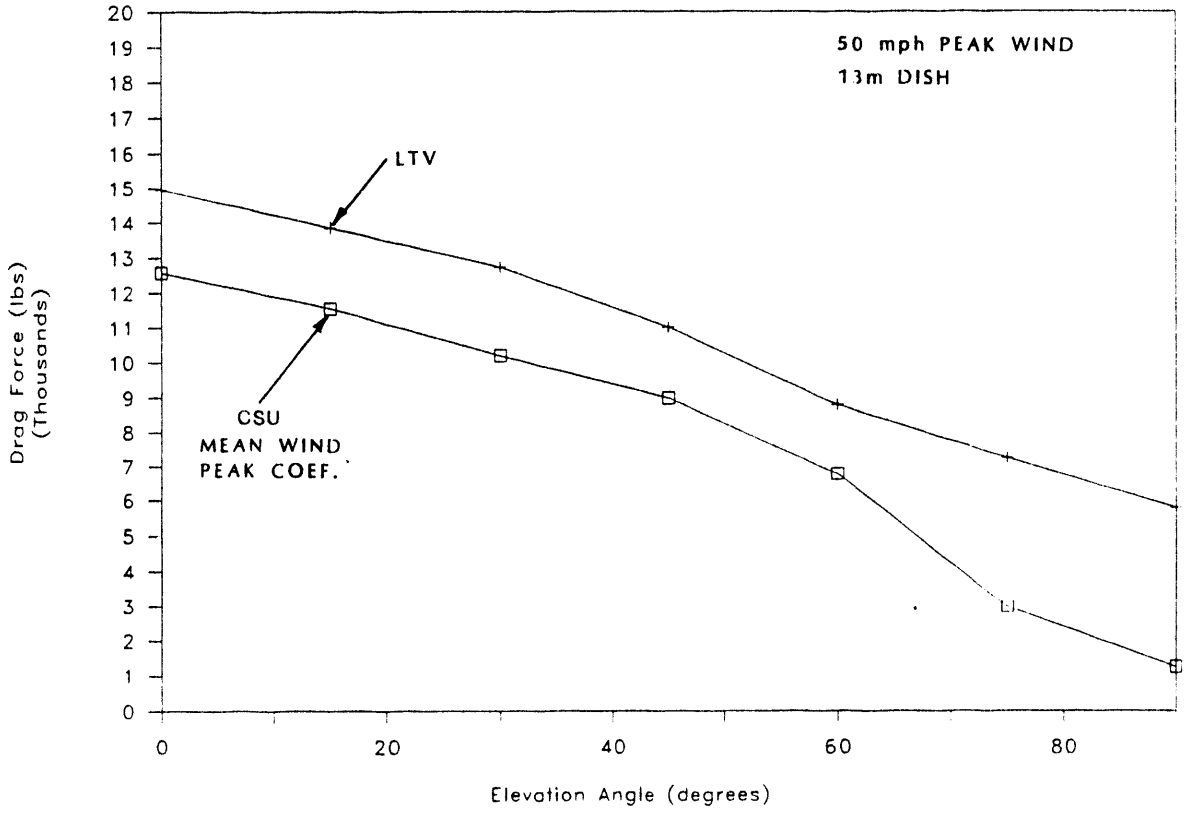

Figure 2.1 Comparison of CSU & LTV Predicted Drag Force at Dish Face.

Lift loads, as predicted with the two approaches, are again similar at low elevation angles, but considerably different as the dish faces the zenith. They are of equal magnitude, but of opposite sign when the dish faces the zenith (see Figure 2.2). This is not significant to the design because the magnitudes are low, however.

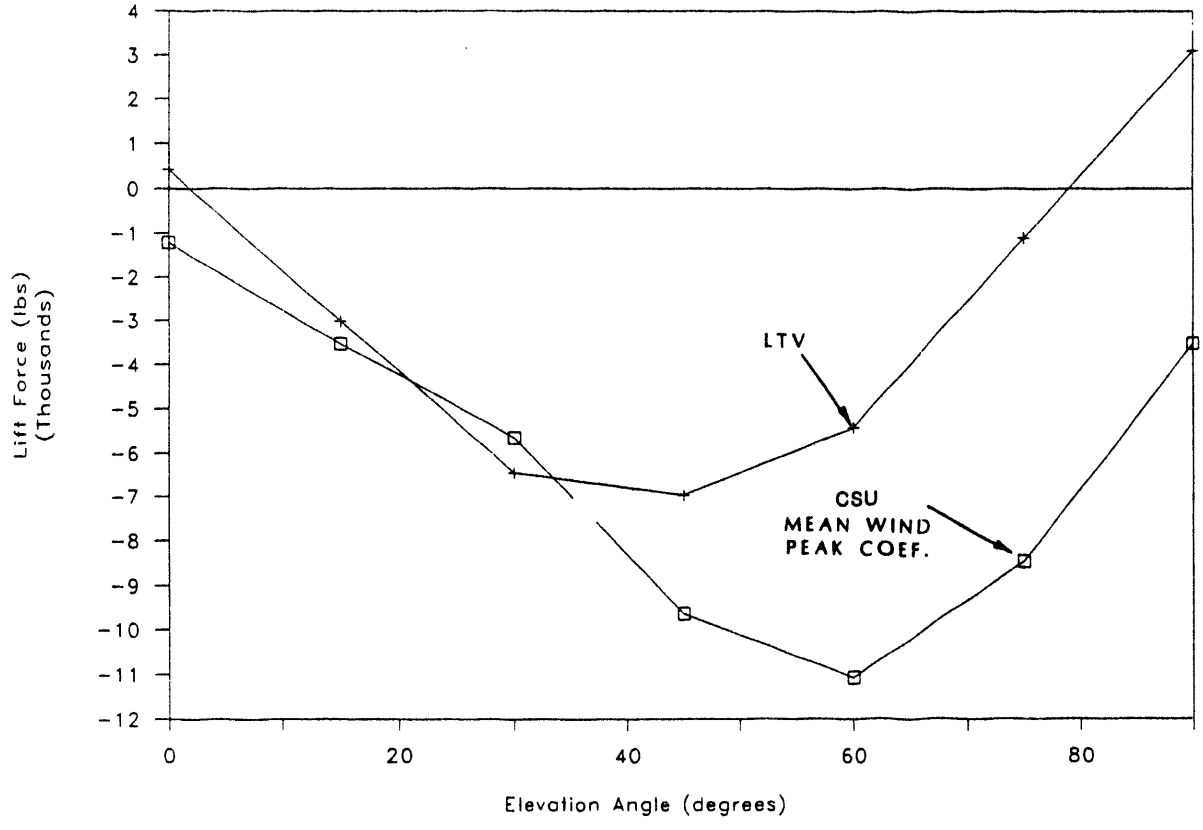

Figure 2.2 Comparison of CSU & LTV Predicted Elevation Force at Dish Face.

The moment loads are significant to the design, however, the two approaches predicted widely different loads. These loads were compared to loads predicted by several other studies to determine if one of the two selected approaches was inappropriate. This comparison is presented in Figures 2.3 and 2.4. The figures show a tremendous variation in loads between the studies. This is likely caused by variations in rear structure, dish f/D, and other aspects of the test. Rather than clarify the loads appropriate for design, this comparison emphasizes the large uncertainty of the design loads.

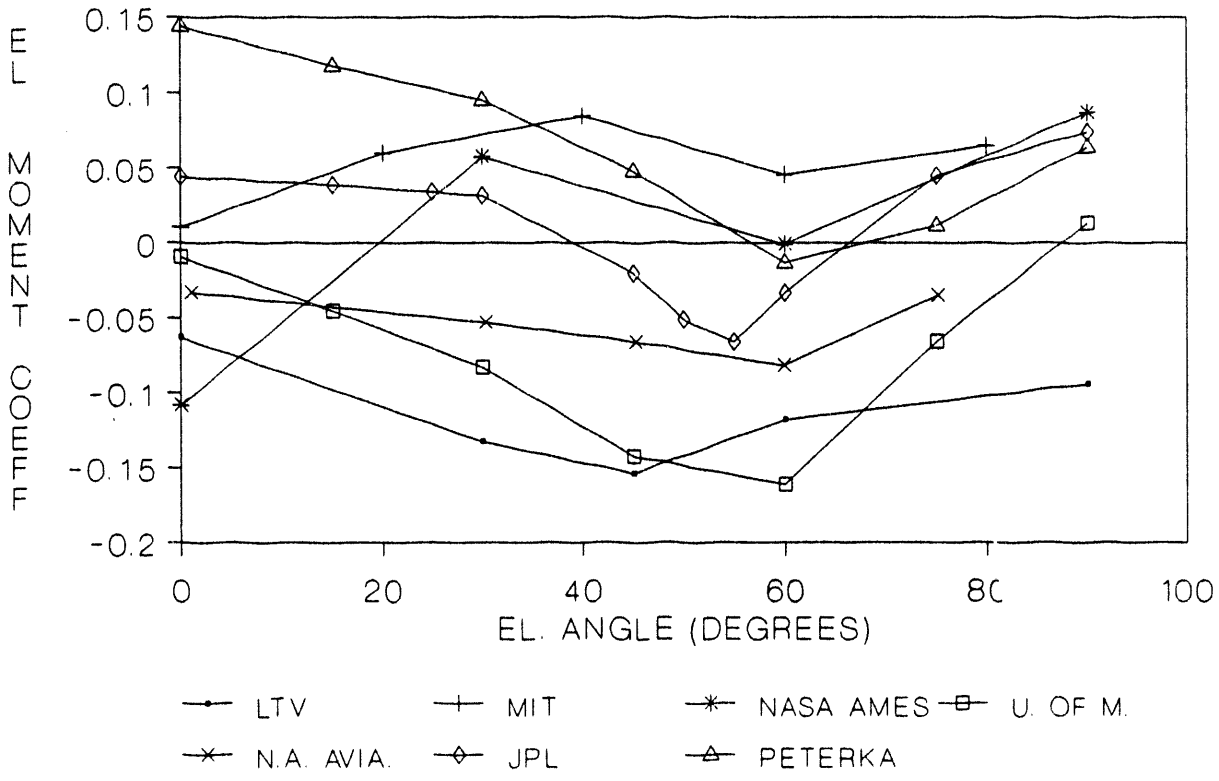

Figure 2.3 Comparison of Predicted Elevation Moments at Dish Face.

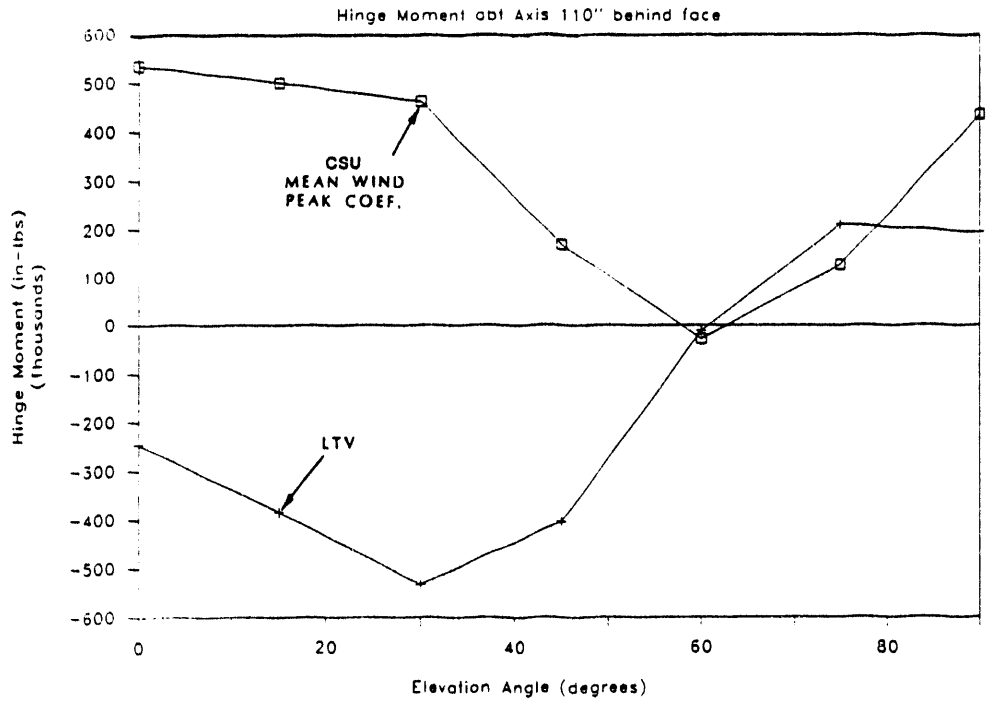

Figure 2.4 Comparison of CSU & LTV Predicted Elevation Moments at Drive Axis.

It is not clear from a review of this data which approach is more correct or even more conservative. CSU's boundary layer wind tunnel is unusual, and SKI is unaware of any similar structures that have been designed by this approach and subsequently built. The LTV report, however, does not include the raw data from which the values were calculated. It also does not fully describe the wind tunnel model. The consultant's software code for summarizing actual loads on a dish presumably has these values coded into it.

Many telecommunication dishes have reportedly been built according to the loads predicted by the LTV wind tunnel testing. However, since most of these designs are deflection driven, it is not clear that inadequacies in the predicted loads would have resulted in noticeable failures.

2.2.2 Selection of Wind Load Data

The LTV data was selected for the design of the dish largely because of its application to structures in the telecommunication antenna industry. The consultant used his proprietary software code to apply the wind tunnel results to the dish which he supplied in a P.E. stamped report. The output was spot checked against the moment and force curves in the LTV report.

Within the scope of this work, we could not reduce the risk by further analysis or investigation. Therefore, we accepted this risk and took mitigating action where appropriate. The following paragraphs summarize this action:

Issue: Smooth reverse curvature of rear structure may have significant aerodynamic effect.

Response: Expert opinion is that this will cause loads to be lower than models predict. Therefore, we will maintain an extra safety factor on highly stressed components where the wind loads contribute a large proportion of the stress.

Issue: LTV wind data does not include complete description of model geometry. Complete checking of model is not possible.

Response: Expert opinion is that this data has been confirmed by its use on many telecommunication antennas with no known failures. Therefore, this data should provide a conservative estimate of stresses.

The AISC code permits a reduction in the peak loads by 1/3 where their source is either from high winds or seismic loading. This was not done in the optical element or drive design because of the uncertainty associated with the predicted wind loads. The philosophy applied here is to allow this additional safety margin because this is the first-of-a-kind solar concentrator design.

2.2.3 Loads on the Dish

The loads and moments are shown in Table 2.1 and Figure 2.5. The coordinate system used in the figure is consistent with that used by the original wind tunnel researchers. This coordinate system is not a conventional right-hand system. It was retained to avoid confusion in translating the raw data to the design geometry. Note that the azimuth angle is the angle between the wind and the projection of the dish axis on the ground plane. The drag and yaw forces always act in a horizontal plane, parallel and perpendicular to the wind, respectively. Lift is always straight up. Elevation angles are measured from the horizon, (ie, El = 0).

The method for predicting the loads on the dish is described in detail in Appendix A. This data and the curves in Figures 2.1, 2.2, and 2.3 are taken at the center of the ring plane. The wind speed for the tabulated data is 32 km/hr (20 mph). Forces and moments for similar dishes of varying diameters and at other wind speeds may be predicted from this data as described in the Appendix.

Table 2.1
Wind Loads at Dish Face

Peak Survival Loads ..... 145 km/hr(90 mph)

Load	Force		Moment		El	Az.
	(kN)	(lbs)	(kN-m)	(ft-lbs)	---(degrees)---	
Drag	142	(32000)			0	0
Lift	19	(4300)			0	70
Yaw	84	(19000)			0	40
Elevation			73	(54000)	0	40
Azimuth			73	(54000)	0	50

Peak Loads Any Orientation ..... 80 km/hr (50 mph)

Load	Force		Moment		El	Az.
	(kN)	(lbs)	(kN-m)	(ft-lbs)	---(degrees)---	
Drag	44	(10000)			0	0
Lift	-22	(-5000)			45	0
Yaw	-27	(-6000)			0	40
Elevation			-45	(-33000)	45	0
Azimuth			-23	(-17000)	0	50

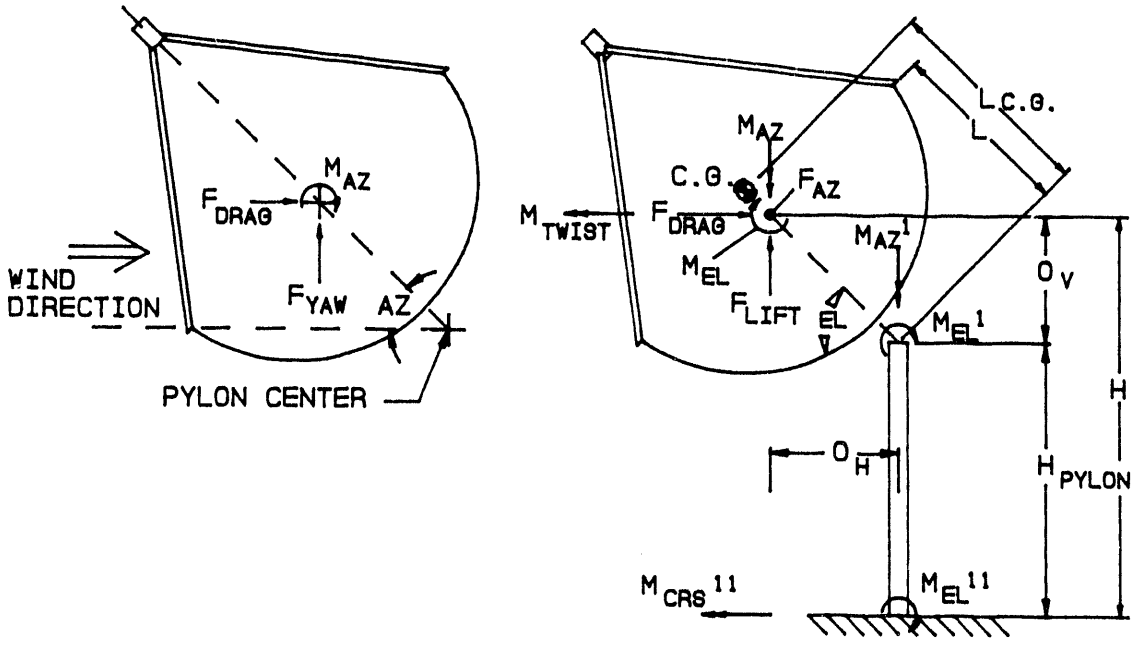

Figure 2.5 Wind Load and Moment Coordinate System Definition. (Viewed from the Side.)

2.2.4 Loads on the Drive

The selected drive configuration has the elevation axis positioned 2.59 m behind the ring face, along the axis of the dish. The moment loads at this point differ from those taken at the dish face. The drag, yaw and lift forces contribute to both the elevation and azimuth moments at some orientations. The moments for these forces are a function of both the elevation and azimuth angles (see Appendix B). Figure 2.6 shows how the forces combine into the net azimuth moment. Figure 2.7 and 2.8 show how the gravity loads also contribute significantly to the elevation moment. At operating wind speeds, the wind load is a very small portion of the total elevation load. At survival conditions, the wind load is still only 22% of the total elevation moment.

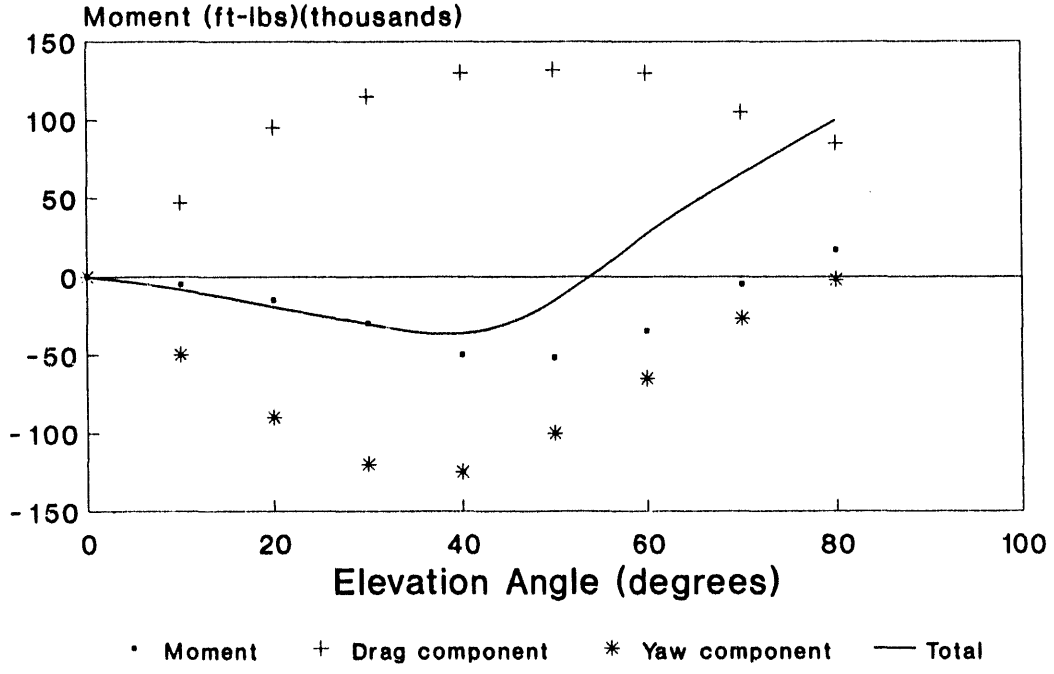

Figure 2.6 Typical Dish Drive Azimuth Moment Components, (80 km/hr [50 mph] wind speed).

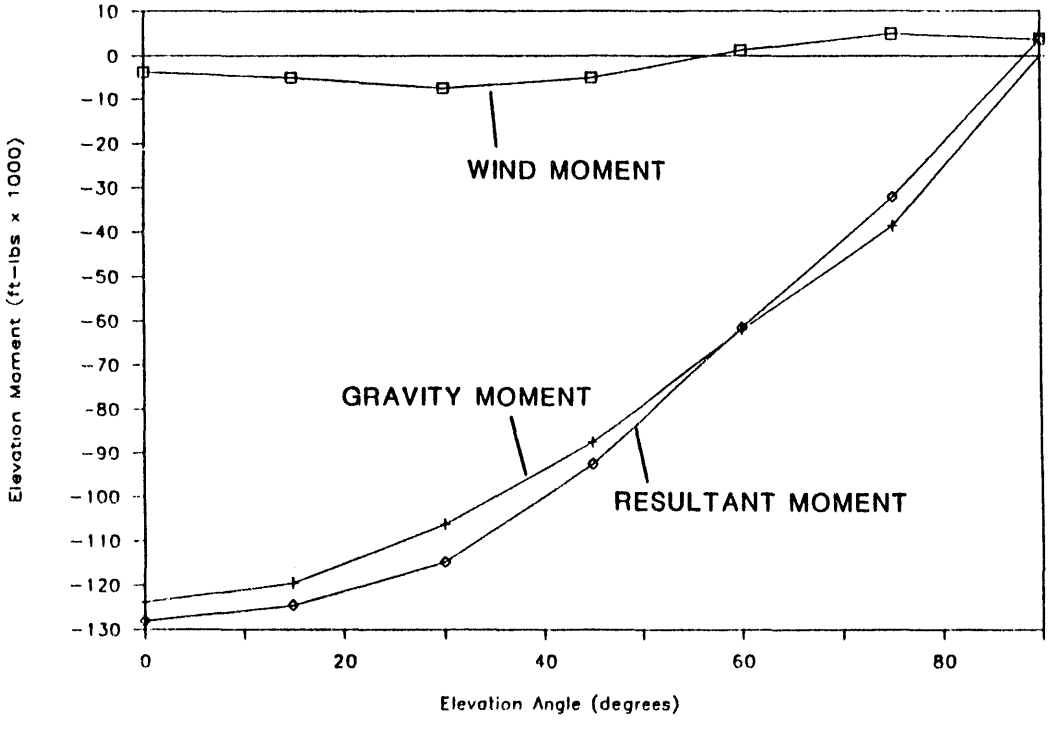

Figure 2.7 Typical Dish Drive Elevation Moment Components, (43 km/hr [27 mph] Wind Speed).

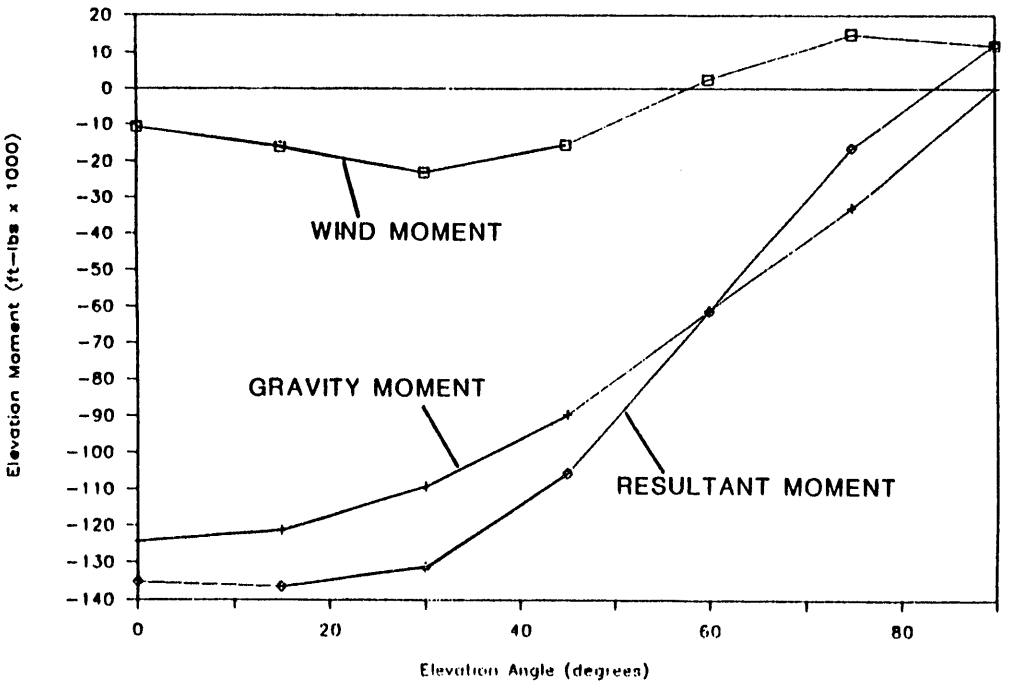

Figure 2.8 Typical Dish Drive Elevation Moment Components, (80 km/hr[50 mph] Wind Speed).

As the design developed, the weight and the location of the center of gravity continually changed causing the predicted moments to change. The loads shown in Table 2.2 are the result of the final design iteration. These values were used to size the hub, the elevation drive, the azimuth bearing, the support pylon, and the foundation.

Table 2.2
Wind Loads at Elevation Axis

Peak Survival Loads..... 145 km/hr (90 mph)

Load	Force (kN)	Force (lbs)	Moment (kN-m)	Moment (ft-lbs)	El (degrees)	Az. (degrees)
Drag	142	(32000)			0	0
Lift	19	(4300)			0	70
Yaw	84	(19000)			0	40
Elev. (total)			-224	(-165000)	0	20
Elev. (grav. only)			-168	(-124000)	0	na
Azimuth			-73	(-54000)	0	50

Peak Loads Any Orientation..... 80 km/hr(50 mph)

Load	Force (kN)	Force (lbs)	Moment (kN-m)	Moment (ft-lbs)	El (degrees)	Az. (degrees)
Drag	44	(10000)			0	0
Lift	-22	(-5000)			45	0
Yaw	-27	(-6000)			0	40
Elevation			-186	(-137000)	15	0
Azimuth			42	(31000)	0	90

2.2.5 Foundation Loads

The loads on the foundation are translated from the loads on the dish. For the elevation and cross elevation moments, the height from the pylon base to the dish center at the specific elevation angle being considered must also be accounted for (see Appendix C). Vertical forces must also include the weight of the support pylon and drive. The resulting forces at the pylon-base foundation interface are shown in Table 2.3.

Table 2.3
Foundation to Pylon Interface Loads

Peak Survival Loads..... 145 km/hr(90 mph)

Load	Force (kN)	Force (lbs)	Moment (kN-m)	Moment (ft-lbs)	El (degrees)	Az. (degrees)
Drag	142	(32000)			0	0
Lift	-53	(-12000)			0	0
Yaw	84	(19000)			0	40
Elev. (total)			675	(500000)	0	20
Elev. (grav. alone)			200	(148000)	0	na
Azimuth			-73	(-54000)	0	50

Selecting wind loads for dish design is far from an exact science. There are wide variations in existing data and corresponding uncertainty in the selected loads. This is mitigated to some extent because the selected wind tunnel results have been successfully used in the design of many commercial antenna structures.

3.O Dish Drive and Support

The dish drive is the mechanism that points the optical element to face the sun. It must provide two degrees of freedom, elevation and azimuth, to accomplish this. The drive also provides a load path to transmit wind and gravity loads from the optical element to the structural support and foundation. A range of configurations was considered for the drive and support of the 25 kWe system.

The selected approach is an elevation over azimuth design (see Figure 3.1) mounted on a single, support pylon. The optical element is attached to the drive at the rear end of its central hub. This attachment point is pinned to permit adjustment of the elevation angle. The elevation axis is actuated by a motorized jackscrew attached to a stub lever also on the back of the hub. The azimuth stage is a plano-centric gear drive from Peerless-Winsmith based on their existing heliostat drive. The drive casting was increased in size to accommodate a larger main bearing for the greater overturning loads of this dish. The support pylon is a tapered welded steel tube with a flanged base that mounts to a cast-in-place, reinforced concrete pier with an integral apron at ground level.

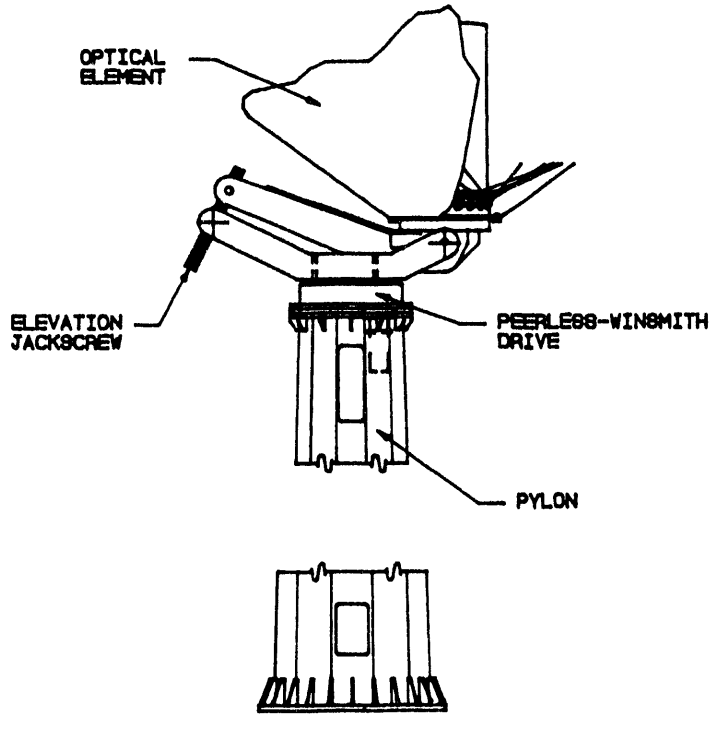

Figure 3.1 Selected Drive Configuration.

The overall requirements of the drive considered both performance and manufacturability issues. The performance goals were as follows:

Acceptable stiffness in 43 km/hr (27 mph) winds to prevent significant power output degradation resulting from drive deflections. Stiffness must also be adequate to assure no performance degradation from gravity induced deflections at various collector orientations. A specific total error budget was not available when this work was initiated.

The drive must be strong enough to withstand survival loads (145 km/hr or 90 mph wind speeds) in stow position and to be able to operate at any orientation up to 80 km/hr (50 mph). It is assumed that the collector will be directed to go to stow before wind speeds reach 80 km/hr, but it is possible that the wind could rise to 80 km/hr prior to the collector reaching stow position. Both the structure and the drive train must be designed to withstand the loads resulting from this condition.

The drive must operate at any latitude. For a point-focus dish, this can be accommodated by either "over-the-shoulder" operation or by permitting greater than 360 degrees rotation. The over-the-shoulder approach requires a greater than 90 degree range of travel on the elevation drive. With this arrangement, as the sun passes north of the collector, the collector can still point at the sun as it rotates in azimuth from east to south to west. Alternately, if the collector can rotate more than 360 degrees, when the sun passes north of the collector, normal azimuth rotation is from east to north to west. For some times of the year, the collector must also travel east to south to west. Therefore, more than 360 degree travel in azimuth is required.

The drive must exhibit no significant "backlash" in its gear train to provide accuracy.

When the stiffness and mass of the optical element, the drive, and the support are combined, the natural structural resonance must be >0.5 Hz, preferably >2 Hz. This is intended to prevent wind turbulence and variations in wind velocity from exciting the structure at a resonant frequency.

The design must also be manufacturable. The design must be practical to fabricate in low early market quantities. This means set up costs and special tooling costs should be minimized.

3.1 Support Configuration Concepts

3.1.1 Phase I Drive Concept

A drive concept was conceived in Phase I that supported the dish at two points on the rim and at the rear of the central hub. (See Figure 3.2). This approach was modeled at the 1.4 m (54") scale. Later, the 7-m optical element was supported at these same three points,

but the reactions had slightly different restraints. This approach was perceived to have five main advantages.

1. The optical element stowed low in the boundary layer of wind flow. This should reduce actual peak loads on the dish and drive.
2. The rear of the optical element could be latched to a secondary support when in the stow position. This would create a secondary path to ground for reacting peak wind loads that did NOT conduct the loads through the drive mechanisms.
3. A single-pedestal drive could be used saving foundation and installation costs.
4. The support structure would be potentially light-weight and low cost because of the peak load limiting and reduced structure.
5. Two of the PCA support legs could be connected directly to a support member instead of the optical element ring, reducing loads and potentially deflections in the membrane support.

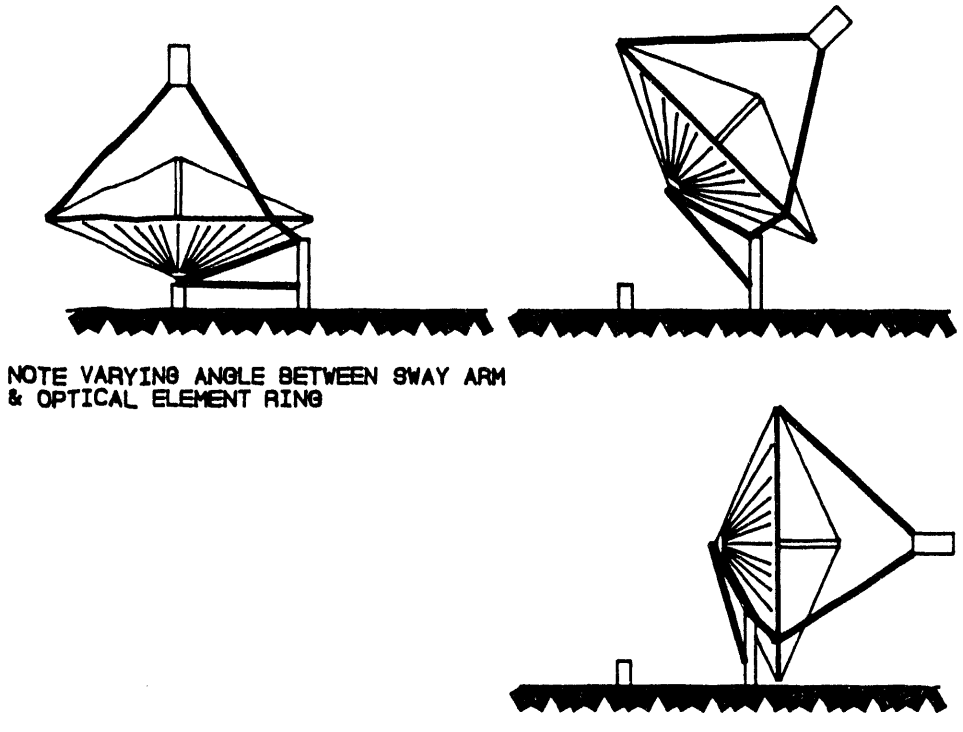

Figure 3.2 Phase I Drive Concept.

When considered in detail, the approach also had disadvantages that ultimately lead to its elimination. The disadvantages were as follows:

1. The driven link of the elevation drive utilized a long jackscrew at a fairly acute angle to its driven moment arm. This caused high forces in the screw and its moment arm, thus, increasing their mass and cost.

2. The poor mechanical advantage of the jackscrew geometry resulted in inadequate stiffness in this direction.
3. The stow position exposed the membrane continuously to potential soiling and weather damage.
4. At some geographical locations, if the dish were stowed, the sun would periodically move into a position to unintentionally focus the dish, endangering the receiver and its support.

No suitable geometry was found tc limit the high jackscrew and moment arm compression loads.

Additional consideration of potential weather damage and the limited soiling experience with the 7-m prototype, suggested that an inverted or sheltered stow position was worth investigating.

No simple and reliable solution to the occasional inadvertent focusing of the stowed dish was found.

3.1.2 Sheltered Stow Configurations

A sheltered stow maintains an inoperative dish facing at or somewhat below the horizon. This provides several advantages:

1. The membranes are protected from hail in almost all wind orientations.
2. The membrane does not collect rain or snow. Draining requirements are less critical.
3. The PCA is in a serviceable position whenever the dish is stowed. This allows simpler scheduling of engine servicing.
4. The dish's hub front end or the PCA can be set into a cradle in the stow position to reduce forces transmitted through the drive during high wind conditions.
5. Soiling of the membrane is reduced.
6. Accidental focusing of a stowed dish can be avoided.

Configurations considered in some detail included a polar drive, a pivoted drive adapter, a yoke support, and the selected cantilever design. These concepts were considered in light of how they could affect the optical element design as well as how effective they were as drives. This was important because the optical element is a unique structure with inherent advantages such as low weight, simplicity, and uniform distribution of loads. Large support reactions applied to the wrong component in the optical element could require inefficient local reinforcement of the optical element.

3.1.3 Tilted-Axis Drive

The tilted-axis drive (see Figure 3.3) offered advantages of sheltered stow, limited travel of one axis, and reduced bending loads in the pedestal. First approximation weight estimates showed it to be one of the lighter configurations. Wind induced deflections estimates were also low. Disadvantages included multiple foundations and a support structure not standardized for all geographic locations. More significantly, the load path for wind and gravity loads on the optical element was completely different from that considered in previous analysis. Two large point loads would be imposed on the ring elimirating the uniform loading of the rim that the spoke structure is so effective at resisting. This approach was determined to be too large a departure from the original approach to consider at this time.

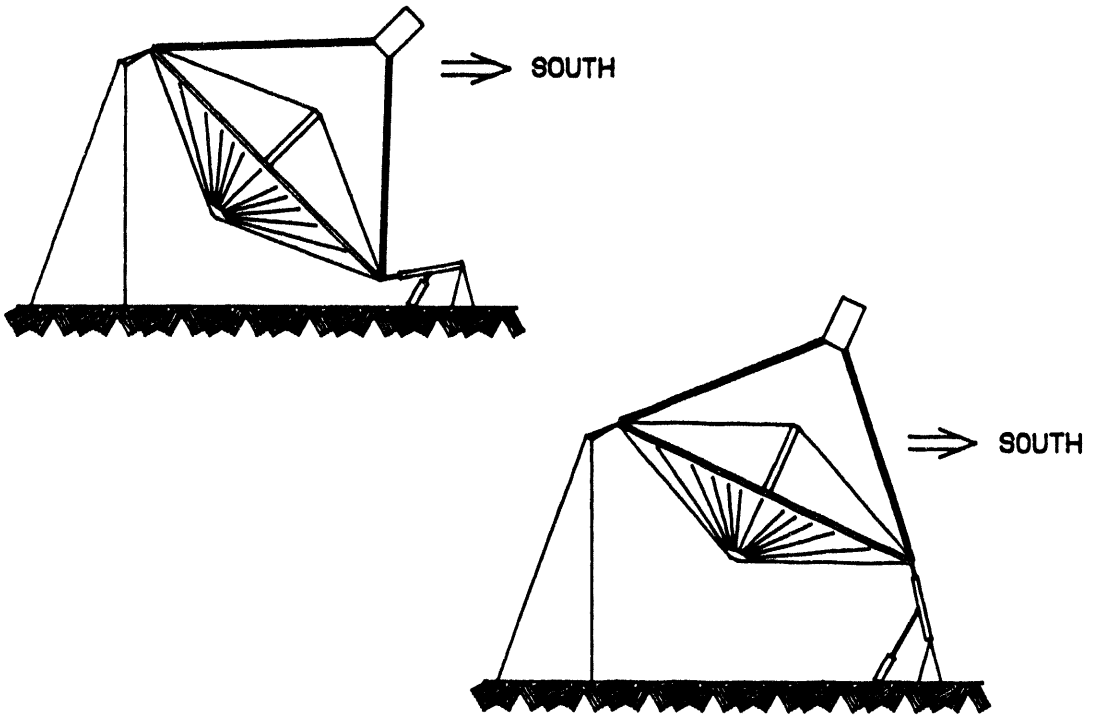

Figure 3.3 Tilted-Axis Drive Configuration.

3.1.4 Pivoted-Drive Adapter

The pivoted adapter supports the optical element at the rear of the hub and at two points on the lower half of the ring (see Figure 3.4). Two of the PCA support legs are also supported at these same two points, reducing the point loads on the ring. The entire adapter is pivoted to achieve the elevation angle required. This approach was implemented on the 7-m prototype. Advantages of this approach are as follows:

1. By supporting the optical element at three places, point load forces and stresses are reduced.
2. Forces required to resist moment loads are reduced because the reaction positions are separated, increasing the moment arms through which they work.
3. The pivot point for the adapter can be selected to minimize jackscrew loads.

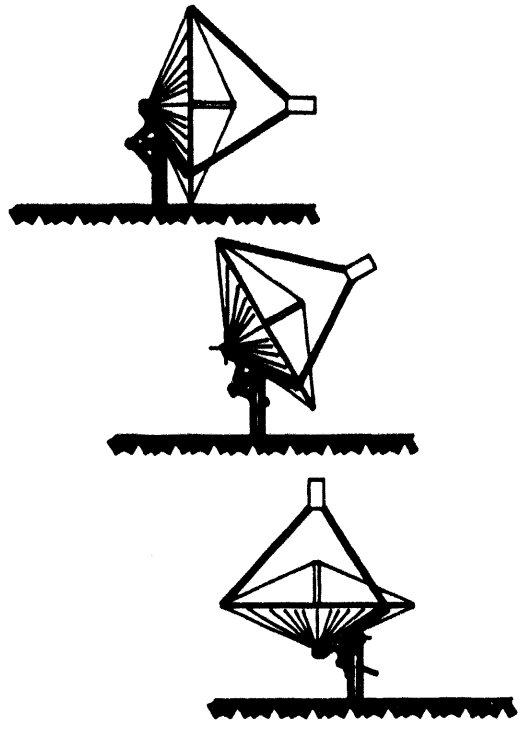

Figure 3.4 Pivoted-Drive Adapter Configuration.

The length of the load path, from the ring support points and from the PCA support to the azimuth drive, is greater than for the cantilevered design. The longer this load path is; the more material is required to maintain the same deflections under load. The inherent stiffness of the optical element is not utilized if these loads are transferred from the ring through an adaptor to the drive. The additional mass of the adapter also lowers the natural frequency of the entire system.

3.1.5 The Cantilever Drive

The cantilever drive is so named because the entire optical element is supported from the rear of the central hub (see Figure 3.5). The elevation axis crosses the rear of the hub at this support point. The hub extends away from the drive carrying the optical element and the PCA. This configuration takes full advantage of the inherent stiffness of the optical element. No redundant structural components are added to carry the PCA loads or resist gravity and wind loads on the optical element. A conventional az/el drive configuration may

be used. Counter weighting to reduce gravity moments about the elevation axis can be considered as a trade-off against a larger elevation actuator and larger azimuth bearing. The perceived advantages are as follows:

1. Efficient structure with fewer parts and less material usage.
2. Can use existing az/el drives.
3. Can provide sheltered stow.
4. Uses cost-effective, single-pier foundation.
5. Can be used with stow saddle to reduce peak loads through drive.
6. Stow position avoids accidental dish focusing.

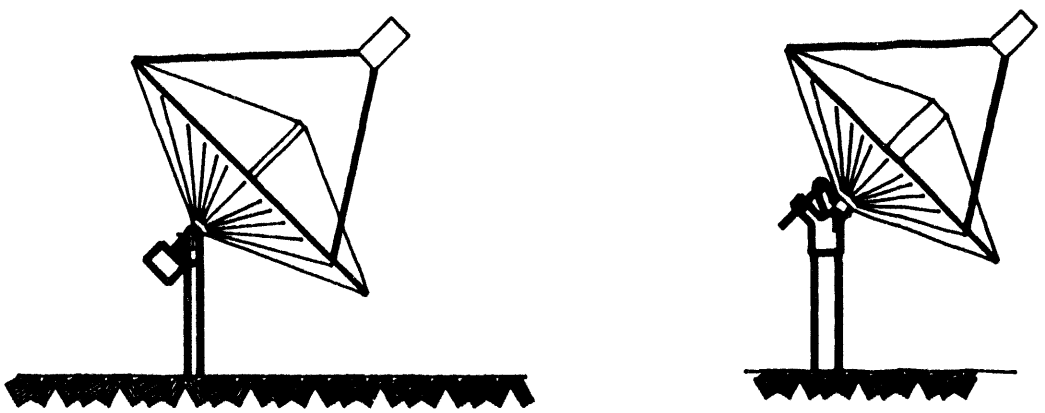

Figure 3.5 Cantilevered Drive Configurations.

This concept requires careful engineering to avoid potential problem areas. Some possible disadvantages include:

1. High loads at the rear of the central hub due to high gravity overturning moment on drive and pylon, and wind loads acting through long moment arm from drive.
2. PCA forces carried as concentrated loads directly on ring.
3. Large polar moment of inertia about azimuth axis at high elevation angles.

3.1.6 Concept Selection

During the conceptual design phase, a comparison of the drive concepts was made based on preliminary estimates of structure size and performance. The tilted-axis drive, although possibly lightweight and accurate, was not considered further for the reasons described previously. The pivoted drive adapter was not pursued because it was judged that it could not be cost competitive because of the redundant structure inherent in the concept. Experience with the 7-m prototype supported this conclusion. An additional concern was that the high mass of the adapter would create too great a polar moment and too low a structural natural frequency.

The Phase I four-bar link concept was not pursued further because of a combination of disadvantages. Its weight is greater than the alternatives, suggesting a higher manufactured cost. There are more major assemblies and components in this drive than the cantilever approach. Actuator loads are very high, which increases cost and can affect reliability. The stow position exposes the reflective membrane to soiling and potential weather damage. The stow position can cause accidental focusing of the dish on the PCA. Finally, service access to the PCA is not practical in the stow position.

The cantilever approach was selected for the final design.

3.2 Drive Selection

After the selection of the cantilevered support, the azimuth and elevation actuators were considered. The size of the dish combined with the cantilevered geometry resulted in large overturning loads, which no existing solar drive could accommodate. The existing drives considered came from heliostat applications where the gravity loads were almost balanced, even on large area units. Several alternative drive approaches were investigated. The goal of these investigations was to utilize technologies developed for other applications. This would reduce development costs and risks. This would also gain production volume cost reductions resulting from the devices' sales to other industries.

3.2.1 Azimuth Drive

Three azimuth drive configurations were considered: a larger Peerless-Winsmith heliostat drive, a king-post drive and a large-diameter roller bearing.

The Peerless-Winsmith company reviewed the application and estimated the required resizing of their plano-centric heliostat drive. This approach already demonstrated the desireable characterization of high torque and high precision in large structure drives. The increased overturning moment for the 25-kWe dish requires a larger diameter azimuth

bearing and housing. The gear train requires little change to accommodate the expected azimuth loads.

A king-post drive could be adapted from the material handling industry among others. It is an old design wherein a rotating cap is set on top of a stationary post (see Figure 3.6). The center of the cap is supported on a thrust bearing. Thrust bearings can carry very high loads, so an unusually large bearing is not required. Overturning moments are reacted horizontally by the thrust bearing in a radial direction plus an additional bearing at the open bottom of the cap. The lower bearing runs on the stationary post. This assembly can be a weldment thereby reducing tooling and setup cost compared to the castings used in the Peerless-Winsmith drive. This is particularly suited to low-to-medium volume production. The manufacturing costs are further reduced because the machining required for this design does not require very tight tolerances. The thrust bearing could be of a self-aligning type. The lower reaction bearings may be spring loaded. The major overturning load is always in the same direction, so zero free-play is not required. These bearings may be either non-metallic plain bearings or sealed bearing idlers for low cost and low maintenance.

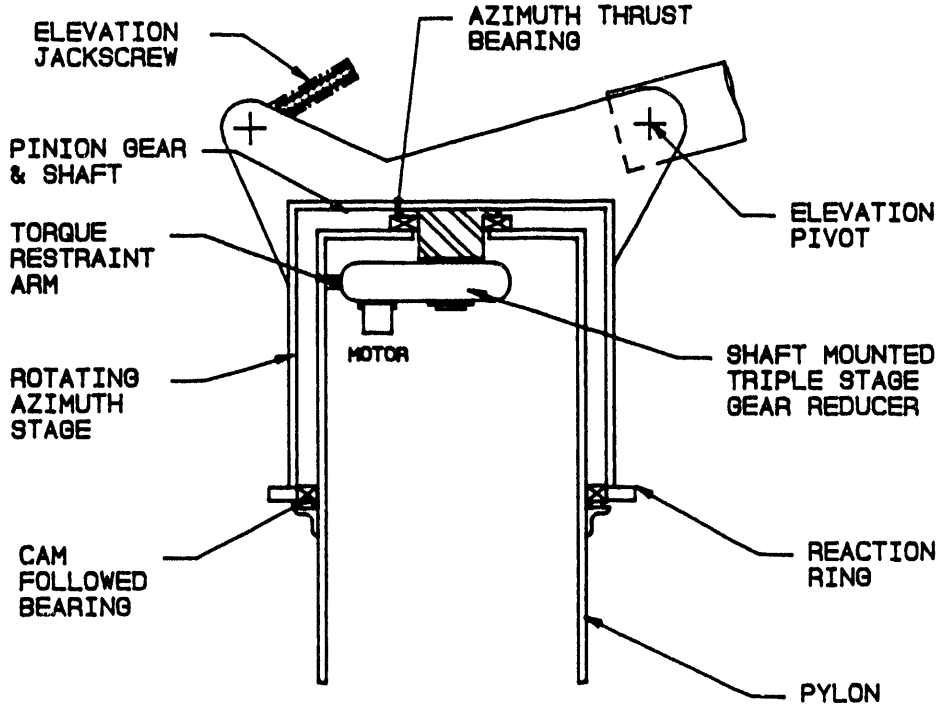

Figure 3.6 King-Post Azimuth Drive Configuration.

Large diameter roller bearings replace king posts today in many applications such as crane turrets, machine tools, and special fixtures. A commercially available combination internal ring gear and large diameter bearing was readily identified. A drive configuration employing this element is shown in Figure 3.7. Note that a single-spur gear may be used to drive the azimuth stage about the ring gear. The dominant consideration in sizing the gear/bearing is the azimuth torque requirement. A ring gear/bearing capable of withstanding the rated torque has an overturning moment several times the required load.

A motor drive is required to turn the king-post or the large combination ring gear/bearing. The conceptual design of the king-post drive kept the motor and drive inside the post for increased weather protection and simple factory assembly. A speed reducer with high stiffness and high torque output is required. Backlash in the drive train must also be minimized or controlled. All the speed reducers considered were standard, commercially available units. Types of drive trains considered were:

1. Multi-stage planetary gear reducer.
2. Plano-centric gear drive.
3. Multi-strand chain final reduction with gear motor primary drive.
4. Dual-shaft, mounted-spur gear reducers counter loaded to eliminate backlash.
5. Multi-stage, helical-gear reducer primary with open-spur gear secondary drive to large diameter combination ring gear/bearing.

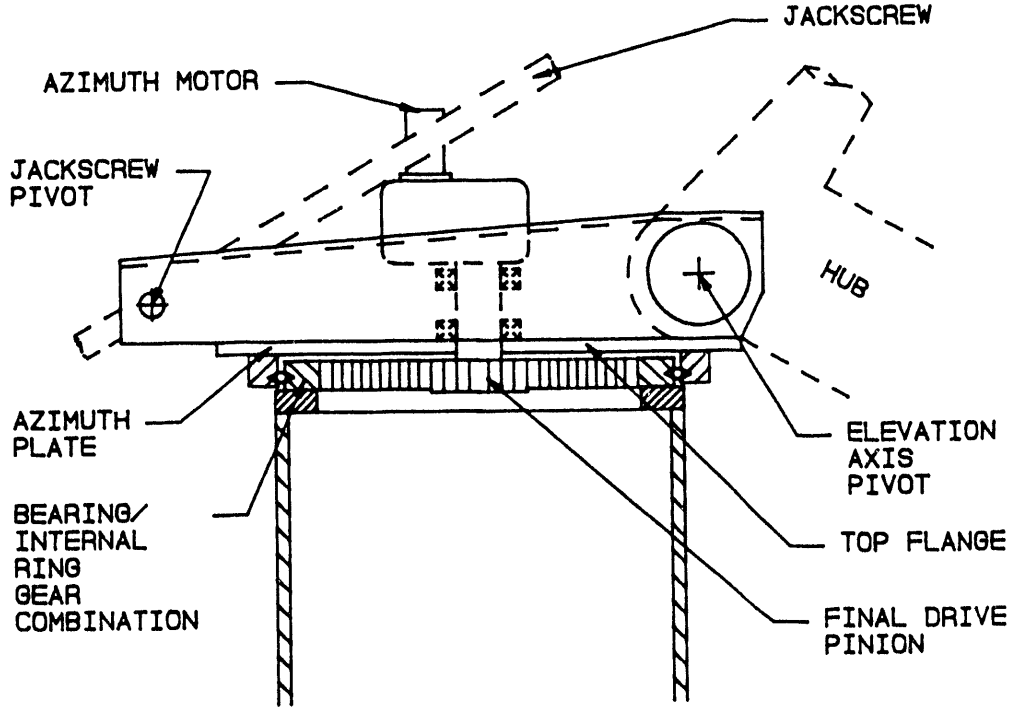

Figure 3.7 Combination Ring Gear and Large Diameter Bearing Azimuth Drive Configuration.

The large commercial gear boxes were not cost-effective (see Table 3.1). Recommended units were actually oversized because units with adequate torque capabilities had much higher horsepower capabilities than this application requires.

Table 3.1Drive Cost Estimates ($)

	Qty. 1	Qty. 100
Planetary gear reducer	19,000	17,000
Plano-centric gear	10,000	8,000
Peerless-Winsmith	8,300	3,700
Chain drive w/gear motor	5,700	3,100
Ring gear/bearing	7,800	3,600

Backlash in the gear train must be minimized to prevent the dish from being moved by the wind and to minimize overshoot and oscillation when the dish position is updated. Backlash in conventional commercial gear reducers is generally too great for this application. Backlash was less of a problem for the chain drive and the ring gear/bearing unit. Both the chain drive and the final reduction spur gear can be adjusted at installation to minimize backlash. The significance of backlash in the primary gear reduction stages is reduced by the first power of the final drive reduction. Commercial tolerance on the ring gear/bearing combination was acceptable. Improved backlash could be obtained by special order with some additional custom honing at the factory. The Peerless-Winsmith unit has relatively low backlash. Actual experience has indicated even lower backlash than the factory specifies. Refer to Table 3.2 for a comparison of backlashes.

Table 3.2
Drive Backlash

	(mrad)
Planetary gear reducer	>4
Plano-centric gear	adjustable to 0
Peerless-Winsmith	1.4
Chain drive w/ gear motor	adjustable, < 1
Ring gear/bearing *	< 1.0

* The value shown for the ring gear/bearing backlash is for the final reduction stage only. The total effective backlash is the sum of this value and the primary reduction gear train backlash reduced by the first order of the final drive ratio.

Adequate torsional stiffness of the dish and drive system is important to avoid resonant excitation by the dynamics of the wind. A minimum resonant frequency of .5 to 2 hertz is generally used as a design goal. Higher stiffness drives contribute to increasing the structure's natural frequency. Table 3.3 summarizes the stiffnesses of various drives under

consideration. The ring gear/bearing drive is clearly the stiffest combination.

Table 3.3
Drive Torsional Stiffness

	(N-m/rad)	(in-lb/rad)
Plano-centric gear	2.0 E5	(1.8 E6)
Peerless-Winsmith	1.6 E7	(1.5 E8)
Chain drive w/ gear motor	9.9 E6	(9.0 E7)
Ring gear/bearing *	1.5 E9	(1.4 E10)

* The ring gear/bearing stiffness factor shown here is for the final gear reduction stage only. However, the effective stiffness of the primary reducer is increased by the square of the final reduction ratio. Therefore, the combined stiffness of the entire drive is not sensitive to the primary reducer's stiffness.

While the large-diameter ring gear/bearing drive looked promising for performance, cost, and simplicity of design, the enlarged Peerless-Winsmith unit was ultimately selected. It was decided that to detail design a different drive within this project was not cost-effective considering that an acceptable design could be readily obtained from a manufacturer with specific experience in this field.

3.2.2 Elevation Drive

Prior experience at SKI and throughout the solar concentrator industry has demonstrated that jackscrew or ball-screw drives are effective for dish elevation axis. Where only slightly more than 90 degrees of motion are required, a single linear actuator is adequate. No other type of actuator was considered. Such units are available from many commercial sources.

There are a few limitations of jackscrews that must be accommodated in any design. A jackscrew is most effective in tension applications. Where very high push forces are required, the screw of the jack acts as a column and can be subject to buckling. If the screw is kept in tension, the same cross-section of screw can carry a much higher load. A second limitation of jackscrews is efficiency. Plain ACME-type screws have a low efficiency. They require more power and generally do not last as long. Recirculating ball screws are much more efficient. The increased efficiency also means that, when the drive motor is de-energized, the load on the screw can back drive the motor permitting the load to move. Some means to prevent this must be devised. Jackscrews are known to increase in efficiency with age and may also require a means to prevent back drive. A motor brake may be added, although this raises questions of maintenance and reliability. For this application, the loads are large enough and required dish position update speeds low enough that a gear motor is required to drive the actuator. A low-efficiency gear reducer (i.e. as a worm gear) was selected as the primary gear reduction. These drives cannot be back driven and will serve as a passive jackscrew brake.

The selection of a cantilevered support configuration permitted the design to keep the jackscrew in tension in almost all combinations of wind and orientation. The jackscrew undergoes compressive loading only when the dish is facing the zenith and the loads are lowest.

Backlash can be an issue in jackscrews, as it is in gear drives. This is particularly true where a jackscrew is driving a balanced load. For the current design, backlash will only be apparent at one point of the elevation motion where the jack load goes from tension to compression. Because of the large pivot arm, the pointing error created by this backlash will be small.

3.3 Drive Detail Design

3.3.1 Azimuth drive

The selected drive utilizes the plano-centric azimuth gear drive developed by Peerless-Winsmith. The azimuth drive housing and rotating output stage is constructed from custom castings. It has a vertical input shaft on the bottom, and the entire top of the unit rotates to provide output. The large-diameter output stage permits use of a large-diameter support bearing for reacting against high overturning moments. A custom fabricated elevation stage bolts to the output platform. This drive and elevation stage combination is similar to the one developed as a low-cost heliostat drive by Peerless-Winsmith for Sandia National Laboratories (4).

The azimuth drive has a cast flange about its base that bolts directly to a matching flange on the top of the pylon. The drive motor is face mounted to the input stage on the bottom of the drive inside the pylon. The pylon design has an access panel to permit inspection and servicing of the motor. The azimuth drive has a 33,000:1 reduction ratio. Peak power input required is 1.7 hp at 1750 rpm, so a 2 hp motor is specified.

3.3.2 Elevation drive

The elevation drive geometry was selected to minimize the peak jackscrew load, and therefore, cost. The total motion from zenith position to stow position requires 115 degrees of travel. To minimize jackscrew load, the angle between the lever arm and the actuator is kept as close to 90 degrees as possible. Since the greatest elevation load occurs with the jack fully extended, the angle can be optimized for this position, so long as the jackscrew is never in line with the lever arm pivot at the opposite end of stroke.

The important variables for optimizing the elevation mechanism geometry are described in Figure 3.8. Table 3.4 shows the selected values resulting from multiple variations of these

dimensions. This geometry results in a peak driving load of 28 tons (32 tons peak static) in the jackscrew.

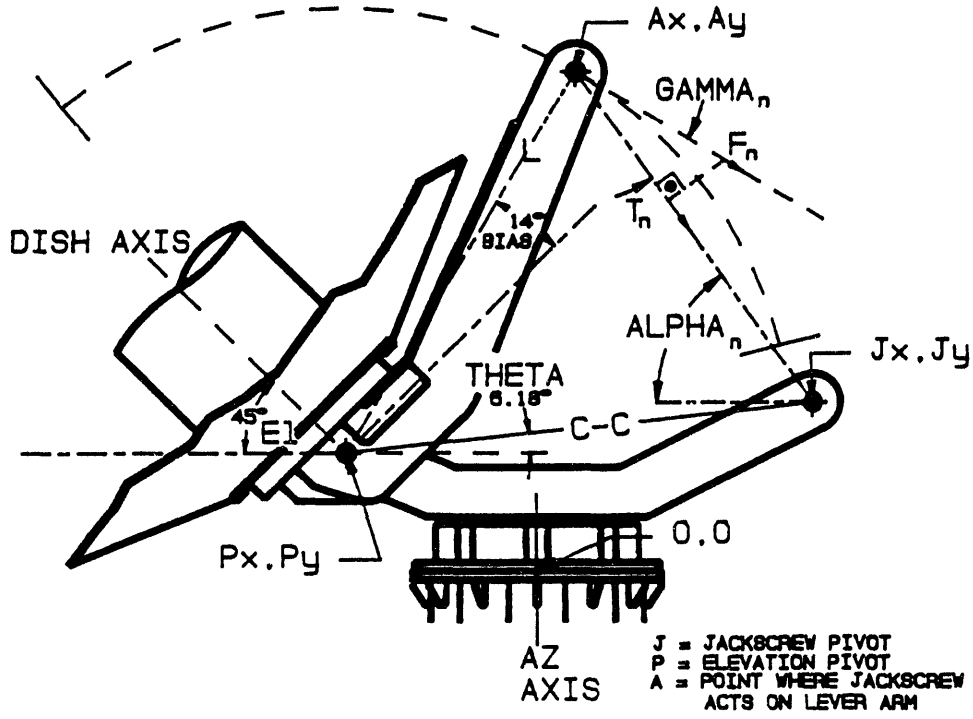

Figure 3.8 Elevation Jackscrew Drive Geometry.

Table 3.4
Selected Elevation Drive Geometry

	(m)	(inches)
C:C	1.65	65
P:x	0.71	28
P:y	0.25	10
J:x	0.93	36.6
J:y	0.43	17
L	1.57	62
Bias	14	14 degrees
Max. screw extension	2.83	111.5
Min. screw extension	0	0
Bearing separation, c-c	0.41	16

Figure 3.9 shows that the largest part of these loads is the weight of the dish. A 30-ton jackscrew is specified with a cap on the free end to unload the ball nut assembly in fully extended (stow) position.

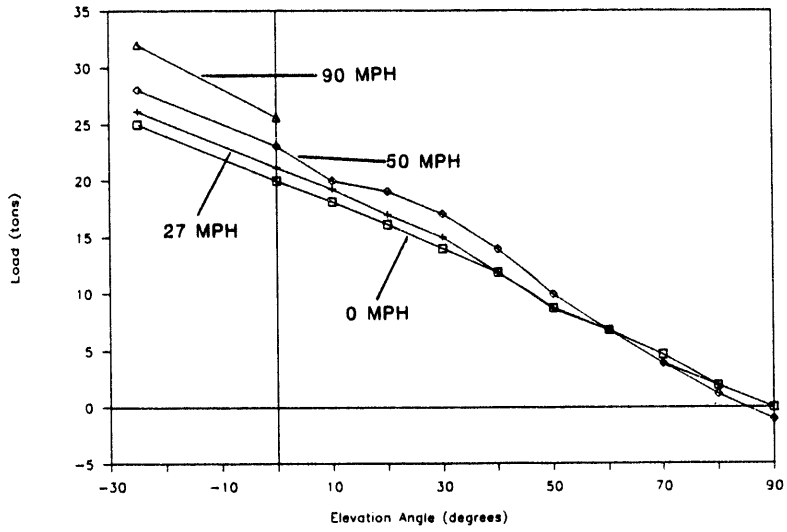

Figure 3.9 Elevation Jackscrew Load, Variation with Wind Speed and Elevation Angle.

The other important loads in the elevation assembly are the pivot bearing loads. The bearings must carry the side loads and azimuth moment of the optical element in addition to resisting the balanced loads from the optical element weight, wind loads, and elevation actuator reactions. Gravity loads account for over 80 percent of all commonly encountered dynamic loads. However, the peak survival load is almost twice the peak operating load. The graph in Figure 3.10 shows the bearing load in the more highly loaded bearing (except for the 0 mph wind case where both bearings are equally loaded). One-inch bore spherical mono-ball, self-aligning bearings are used to keep costs low and permit simple assembly and replacement. Their mounting detail is discussed more completely in Section 7 of this report.

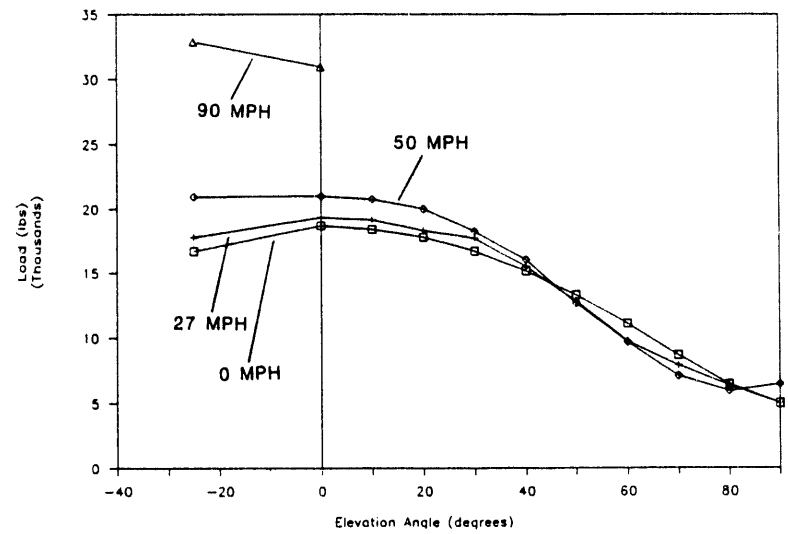

Figure 3.10 Elevation Pivot Bearing Loads, Variation with Wind Speed and Elevation Angle.

Identical bearings are used for the pivot of the jackscrew mounting. This mount is a fabricated channel with a trunnion at either end supported by the pivot bearings.

The elevation assembly is based on a flat plate that bolts to the rotating azimuth platform. Two main side rails, which serve to stiffen the plate, are extended on both ends to provide pivots for the screwjack mounting and the elevation axis bearings. Additional stiffeners reinforce this assembly at right angles to the side rails.

3.4 Structural Support Sizing

The main support for the dish and drive is a single hollow steel pylon. This approach has been used successfully for dishes and heliostats. Manufacturing studies have shown it to be cost-effective (10, 11). The selected drive is designed to mount to a horizontal flange. The single-pylon support easily accommodates this arrangement.

Several variations of the pylon construction are possible. The pylon body can be tapered from bottom to top to reduce material usage and improve stow angle. Secondly, the pylon can be cast in place into the concrete pier foundation. This approach has been used with heliostat supports to decrease installed costs by eliminating the ground level flange connection and using the extended pylon body to replace the reinforcing bar cage traditionally set into the concrete pier. The current work compared costs for a flange mounted and a cast in place pylon. Contractor quotations for the installed piers by the two different methods were compared. The flanged pylon with a bar-reinforced pier was selected as the less costly approach.

The pylon sizing was driven by two issues. The pylon height was selected to support the dish at stow such that a height of 0.46 m (18") was maintained between the lowest point of the optical element ring and the ground. This clearance was selected to avoid low vegetation and moderate snow accumulation. The pylon cross-section was selected to assure that, under peak wind loads, the stresses in the pylon did not exceed AISC allowables. Initial sizing was done at SKI. The detail design of the pylon and its foundation were then subcontracted to a firm experienced in detailing and installing large antenna structures and their foundations (12).

Foundation design is by nature very site specific. The current design was performed for soil conditions existing at Sandia's NSTTF.

3.4.1 Design results

The loads on the pylon are tabulated previously in Table 2.3. The pylon was sized to limit bending stress to the AISC allowable in the worst case wind load orientation; 90 mph wind speed, 0 degrees elevation, 0 degrees azimuth. A nominal 1.11 m (44") diameter tube with a

6.3 mm (1/4") wall thickness will withstand the bending load. Direct shear, local buckling, and tube torsional stress were checked and found acceptable. Table 3.5 shows the stress ratios for several stress types and components. "Stress ratio" is defined as the actual stress divided by the allowable stress.

Table 3.5
Stress Ratios for Various Stress Types

Preliminary Analysis

Stress Type	Stress Ratio
Bending	0.92
Direct shear	0.07
Local buckling	0.80
Tube gross torsion	0.18
Combined axial compression and bending	0.79

Detailed Analysis

Base flange stress	0.60
Base flange gussets	0.85
Hand access holes	0.55

Bending, shear, and gross torsional stresses were determined with classical analytical approaches. The local buckling was evaluated by several empirical methods (13). The result from the most conservative approach is reported. The method used to evaluate the combined bending and compressive stress is presented in the AISC code (14). Detailed analysis and consideration of local stresses at flange gussets, flange-to-pylon interfaces, and pylon access ports were performed by WG Associates.

The primary pylon sizing was stress driven, although the pylon does deflect significantly as shown in Table 3.6. The deflection is primarily a result of gravity loads which can be compensated in the tracking control algorithm. Actual peak wind-induced deflections are 0.3 mrad at the worst wind azimuth orientation and worst elevation position. This magnitude of deflection is tolerable under any case, but is even less significant considering that this combination of worst case orientations occurs very rarely.

Table 3.6
Pylon Stresses and Deflections for 0 Degree Azimuth Wind
0 Degree Elevation Angle

Wind speed	km/hr	0	43	145
(mph)	0	27	90	
Peak combined bending	MPa	35.8	22.7	111
and torsional stress	(psi)	5200	3300	16,100
	mm	5.9	4.4	- 10.4
Lateral pylon top deflection	(inches)	0.231	0.174	- 0.410
Total angular deflection	(mrad)	1.8	1.5	- 1.8

The wind forces act counter to the gravity loads in creating deflections and stresses in the 0 degree azimuth orientation. With a rear wind, the dynamic forces sum to the gravity loads. The wind load data used for the design indicates that the 180 degree drag coefficient is significantly lower than the 0 degree drag coefficient (44% of the front coefficient). Peak loads and deflections, therefore, occur with a front wind condition.

The design loads for the foundation are listed in Section 2. Initially, the foundation design was performed for a simple cast-in-place pier. A monolithic apron at ground level was included in the design for convenience of the installers and service operations. Initially, no credit was taken in the design for the load bearing characteristics of this apron. Review of the foundation pier performance required that the apron's contribution to torsional resistance be checked because the pier alone was marginal in resisting worst case torsional loads. The apron contributes significant resistance to torsional movement. The apron will also resist moment loads (resulting from lateral forces at the pylon top) at the pier pylon interface. This reduces bending stresses in the pier and lateral soil pressure at the upper end of the pier.

The soil design limits for the design of the pier foundation are obtained from on-site soil tests at the NSTTF (15). Although the report deals with 5 specific locations, it is believed that the soil characteristics are sufficiently similar throughout the area to justify use of the report findings for this design. The allowable soil factors used in the design are noted in Table 3.7.

Table 3.7
Allowable Soil Reactions

Bearing pressure	96 kPa	(2000 psf)
Net lateral pressure	55 kPa/m	(350 psf/ft. depth)
Friction coefficient	0.4	

The minimum pier diameter was defined by the smallest bolt-circle diameter for the pylon base size. A 1.2 m (4') bolt circle was selected with a re-bar cage specified, external to these anchor bolts. Three inches radial clearance from the re-bar to the pier O.D. resulted in a 1.5 m (5') pier diameter. Availability of a soil auger of this size was confirmed for the Albuquerque area.

The depth of the pier was driven primarily by bending, which results from the overturning moment. The reinforcing steel is designed so that when the pylon is loaded in bending the steel yields before the concrete fails.

The pier design was checked for soil reaction to torsion and compression loads and found to be adequate. By inspection, uplift is of no concern.

The anchor bolts are 32 mm (1-1/4") in diameter, resulting in an apparent overstress of 9%. However, the bolts were sized in consideration of the highly conservative nature of the analysis wherein;

> no credit was taken for the bolt pre-tension effect, and the load-bearing effects of the grout were not applied.

The pier foundation design provides appropriate factors of safety as shown in Table 3.8. The factor of safety is defined as the allowable divided by the actual stress. A 3-m (10-foot) diameter apron has been integrated into the pier design at grade level.

Table 3.8
Concrete Foundation Design Factors of Safety

Bending	1.38
Shear	2.33
Bearing	1.58
Torsion	1.31

3.5 Support Detail Design

3.5.1 Pylon

The pylon will be fabricated similar to many electric power poles (see Figure 3.11). The pylon is a tapered tube of all welded construction. The tube will be formed by a press brake operation. To reduce labor in working such large pieces, the sections are faceted with 12 sides to approximate a circular cross-section. Flanges are located at both ends of the pylon. The top flange mates with the base of the azimuth drive casting. There is an intermediate leveling plate to permit simple accurate field leveling of the drive and to reduce leveling tolerances (and costs) for the pylon installer. Top and bottom flanges are gusseted to the pylon body. At the bottom flange, there is an additional reinforcing ring inside the pylon body where the gussets bear on the pylon wall. This reduces local stresses at that point. Table 3.8 shows the important geometry of the pylon and selected component sizes.

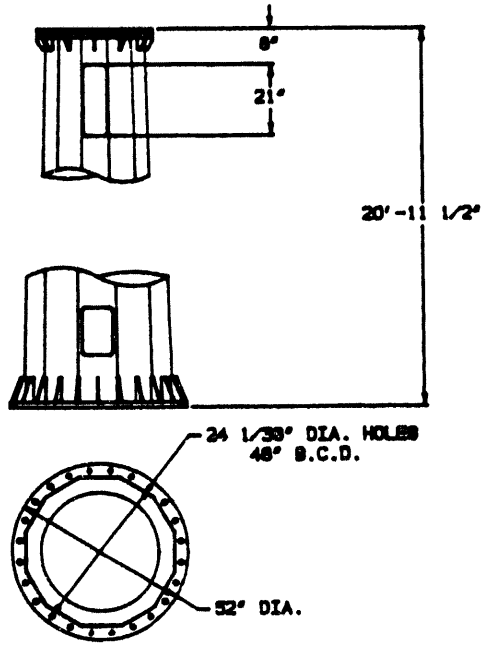

Figure 3.11 Selected Pylon Design Detail.

The pylon has two hand-holes for access to the inside. These are required for periodic inspection for corrosion and to service the azimuth drive motor. The upper-hand hole is used to service the motor. A special fixture should be fabricated to support the motor during removal and installation to protect it and the service personnel. The lower hand-hole is used primarily for inspection and to retrieve any dropped tools or parts. The hand-hole design includes edge reinforcement to maintain a load path where the pylon material has been removed. The cover plates are not designed as load carrying members. The design of the hand-hole cross-section may be varied if the fabricator has a different standard configuration. Such a configuration would require structural analysis prior to use.

Table 3.9
Pylon Design Summary

Top flange height	6.4 m	(20'-11 1/2")
Pylon base across flats	1.1 m	(44")
Pylon top across flats	0.74 m	(29")
Number of sides	12	
Wall thickness	6.3 mm	(1/4")
Material	A36 steel plate	
Top flange I.D.	0.70 m	(27.50")
Top flange thickness	22 mm	(7/8" stock)
Bolt circle diameter (primary)	0.81 m	(32")
Number of bolt holes	12	
Bolt hole diameter	21 mm	(13/16")
Base flange O.D.	1.32 m	(52")
Base flange thickness	38 mm	(1 1/2")
Bolt circle diameter	1.2 m	(48")
Number of bolt holes	24	
Bolt hole diameter	35 mm	(1 3/8")
Base outside gusset height	181 mm	(7 1/4")
Outside gusset thickness	13 mm	(1/2")
Top inside gusset height	102 mm	(4")
Top gusset thickness	6.3 mm	(1/4")
Total Mass	1187 kg	(2611 lbs)

3.5.2 Foundation

The foundation design is a straight-sided, poured-in-place, cylindrical pier 1.52 m (5 feet) in diameter (see Figure 3.12). At grade level, there is an integral 3.0 m (10-foot) diameter apron, .03m (1 foot) thick. There is a continuous, cast-in gusset transition from the pier to the apron, .03 m (1 foot) high with a 1.8 m (6 foot) diameter. The pier's reinforcing steel cage uses 24 #9 bars vertically on a 1.32 m (4'-4") circle. Number 4 bars serve as circumferential ties for the verticals. A single layer combining #6 and #8 bars is used to reinforce the apron in a radial pattern with circumferential ties. A circle of 24, 32 mm (1-1/4") anchor bolts are cast in place. The pier is 6.4 m (21 feet) deep.

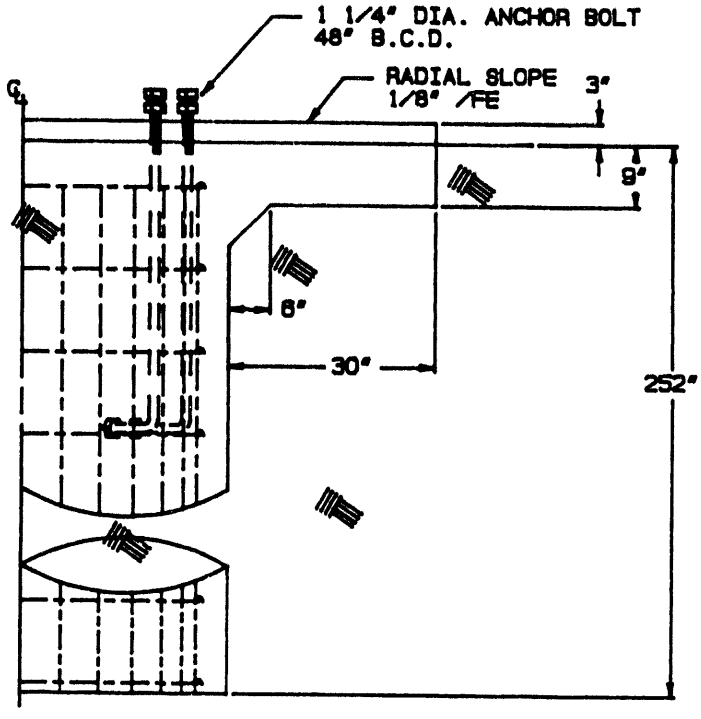

Figure 3.12 Selected Foundation Design Detail.

A total of 13.4 cubic meters (17.7 yards) of concrete is required. A mix with a 28-day compressive strength of 27.6 MPa (4000 psi) is specified. A total of 1236 kg (2720 pounds) of reinforcing steel is required.

It is important to emphasize that this foundation design is site specific and must be thoroughly reconsidered based on reliable soil test data for any other dish site.

4.0 Controls

Controls for a complete collector involve three separate primary functions:

a. Collector tracking,
b. Concentrator focus, and
c. Power conversion operation.

The PCA has numerous variables to be monitored and controlled (power output, available insolation, motor speed, temperature of receiver, engine, generator, heat rejection system, etc.). Collector tracking and focusing are relatively simple and easily isolated control tasks, respectively. This design has considered the tracking and focusing requirements but has not addressed the PCA control. The tracking and focus controls require single real-time inputs to initiate the required operating mode. These controls also have single-continuous status outputs, to indicate normal or alarm conditions. Since the required Input/Output (I/O) signals for these controls to operate are minimal, they have been designed as semi-independent units to be slaved to a central dish/PCA controller. Integration of these controls with the PCA controller will be performed at a later time when the PCA control scheme is better defined and a more specific target market is identified.

4.1 Tracking Controller

The dish must accurately and continuously track the sun during operation to maximize the amount of energy directed into the receiver aperture. Ideally, the tracking control will not only accurately follow the sun but also compensate for inaccuracies in the control and drive components, and structural deflections resulting from gravity or wind loads. The tracking control must be operational at any anticipated geographical location.

There are two basic approaches possible for dish tracking controls. These are closed loop and open loop.

4.1.1 Closed-Loop

In a closed-loop tracking controller, an error signal is generated by comparison of signals from optical or thermal sensors. These sensors either react to the direct incident solar flux or to reflected energy striking the receiver. The error signal is interpreted by the controller, which initiates some movement of the drive mechanism to minimize that error.

An optical tracker typically measures sun misalignment from the sensor axis in a single plane. In one configuration, a pair of photocells is separated by a fin. Unless the fin is

An optical tracker typically measures sun misalignment from the sensor axis in a single plane. In one configuration, a pair of photocells is separated by a fin. Unless the fin is pointed directly at the sun, it will cast a shadow on one cell. The unbalanced output from the two cells creates an error signal. Two such sensor pairs are required to track the sun in both elevation and azimuth (or in hour angle and declination angle). The controller logic must manipulate the drive to minimize both signals.

One problem with these sensors is that it is possible for them to track the bright edge of a cloud when the sun is partially obscured. Also if the collector is turned away from the sun (so that both photocells are shaded), the tracker must have some other means to determine in which direction to move. These sensors are also sensitive to dirt accumulations that may reduce the output from the photocells unevenly.

Spilled energy sensors may be used to track a collector, after it has first been directed at the sun by some other means. The sensors are arrayed about the lip of the receiver entrance facing towards the reflector. When the collector is off track, the concentrated image will illuminate sensors on one lip more than the others. The logic will drive the collector to balance the output from all the sensors.

The high temperatures and fluxes that exist at the receiver plane are problematic for sensor survival and calibration stability. Also, convective heat losses from the receiver may create misleading sensor imbalances that change with position, wind speed, and wind direction.

A conceptual design for a feedback sensor is to use a video camera with software based on the Beam Characterization System (BCS) developed at SNL for measuring concentrator performance. The camera would be located along the dish axis well out of the concentrated flux zone. It seems the system could directly optimize power into the receiver. Considerable development would be required to implement this approach. The details of the controller would probably be specific to the receiver used. Mention of the concept is made here to be considered for possible future development.

4.1.2 Open-Loop

An open-loop controller calculates the sun azimuth and elevation angle based on current date and local time and a stored value for the collector's latitude. The controller compares the calculated angles to the actual direction in which the collector is pointing and initiates drive movement if there is disagreement. The dish position is determined by encoders on the drive mechanism, which supply a signal to the tracking controller.

Open-loop controllers are dependent upon dish axis position encoders and internal software to maintain accurate positioning. An accurate reference clock is also required, usually located internal to the controller. The controller software must also accurately anticipate a

number of "real-world" variables. These may include direction and degree of tilt of drive mechanism as installed, and deflection of the structure as function of elevation angle.

4.1.3 Closed vs. Open Comparison

At first investigation, the closed-loop approach would seem to offer several advantages over open-loop tracking. However, making it reliable and serviceable is a challenge. One advantage of the closed-loop approach is its potential to optimize dish performance by compensation for real-world variables. A synthetic tracker can only compensate for variables that the designer has anticipated and modeled correctly, which could create tracking errors in practice.

Field experience at several sights, with equipment by various manufacturers, has shown optical tracking sensors to have significant reliability problems. Even the best sensors are sensitive to accumulated dirt. Closed-loop systems also have been troubled under partially cloudy conditions, with occasional tracking of bright clouds instead of the sun. Obtaining sufficiently accurate resolution may be a problem with a very high performance dish such as the stretched-membrane dish. Some dishes have experienced problems with sensors mounted at locations that deflected differently than the bore site of the concentrator.

Dish structures that are too limber have been problematic for open-loop trackers also. What open-loop trackers have done is to eliminate the reliability problems associated with active sensors. The position encoders that they use are generally reliable, industrial components. Another significant advantage of the open-loop tracking approach is the controlled manner in which the sun is acquired and off-tracked. When the dish first comes on-sun, an area of concentrated flux traverses across the lip of the receiver from its outermost edge to the center. This happens again when the dish is taken off-sun. This highly concentrated flux must not dwell on the PCA support structure. Even the insulated lip of the receiver cannot withstand this flux for a sustained period of time. The open-loop tracker can be programmed to minimize the time the flux is on the receiver lip. It can also be programmed to keep the flux off the PCA supports regardless of the dish elevation or azimuth angles.

What a strictly open-loop controller cannot do is recognize if some accidental offset in its control algorithm exists, which places the concentrated flux outside the receiver aperture. Deflections in the structure or foundation could also occur which the controller would not know to compensate for. If an encoder signal was interrupted momentarily or the controller memory was corrupted, this event could occur. While the bias may not be great enough to endanger the structure, the performance of the receiver would be affected.

4.1.4 Ideal System

The preceding considerations suggests that a hybrid might be the best tracking system for the following reasons:

a. The dish would not get "lost" in partially sunny conditions.
b. Sensor failure will not cripple operation.
c. The dish will come on- and off-sun in a safe manner.
d. Fine-tuning will be accomplished once on-sun.
e. Small changes in foundation, tilt, structure, or clock will automatically be accommodated.

After consideration of prior system experiences and the availability of demonstrated controllers and sensors, a conceptual system was defined. Ideally, SKI would use an open-loop tracker with full-time flux spillage sensors at the receiver lip. Two pairs of diametrically opposed thermocouples would be imbedded in the ceramic insulation around the receiver lip. Thermocouples were selected for their good reliability and stability at relatively high temperatures. The horizontally opposed sensors would be used to fine tune the azimuth angle. The vertically opposed sensors would be interpreted for fine tuning the elevation. Some adjustable bias will be built intc this comparison to compensate for possible increased convective heat losses on the upper side of the receiver aperture. A PID algorithm will be used to compensate for fluctuations resulting from structural oscillations, wind gusts, etc.

A thermocouple-feedback approach has been tried before on some LaJet concentrators. The limited information available to us suggests that all of the problems with this system were not overcome. The arguments in favor of investigating it further are as follows:

1. Variable heat loss for the upper and lower thermocouples will be anticipated and compensated.
2. Effects of thermal-time constants will be addressable through use of PID comparison algorithms.
3. The stretched-membrane dish will have a more uniform concentrated image, thus having more uniform spillage.
4. The primary tracking will be accomplished by open- loop control.

In addition to the optimization of on-sun performance, the flux-spillage sensors will provide a secondary disaster avoidance routine. Concentrated flux on the receiver lip for an excessive period of time would trigger a go-to-stow signal based on the presumption that the open-loop tracking has developed an inappropriate bias of some sort.

4.1.5 Selected Tracking Control

After consideration of the level of effort to develop such a control and a review of the currently existing controls, SNL and SKI concluded that it would not be prudent to design an entirely new control at this time. Open-loop controls exist that will satisfy most of the requirements of our dish.

The selected controller, dubbed SolarTrak by its developer, was developed at SNL (6) under the photovoltaic program. It has an open-loop configuration. It is programmable for a variety of drive configurations. It has compensation for drive tilt and gravity-induced deflections as a function of elevation angle. It also permits automatic optimization of the control algorithm based on measurement of the collector's power output. Licensing of the design is available from SNL. Manufactured controllers are also available from a corporate licensee, Solar Technologies, Ltd. (STI), Inglis, Florida.

The reported accuracy of the calculated sun position by the SolarTrak is 0.01 degrees (0.17 milliradian). There are over 100 operating parameters that can be set in the SolarTrak to specify the exact "personality" required for the characteristics of the dish that it is controlling. A detachable Data Panel is used to program these settings. The panel can be left attached for monitoring purposes or removed for use on other controllers. If left attached, it can be password protected to prevent unauthorized reprogramming. The SolarTrak can be operated as an autonomous unit or can provide addressable communications for master/slave applications.

If additional programming changes to the basic algorithms are required, this is possible at the factory. One such required change for tracking a thermal dish instead of the original PV-panel application is a specific path to follow for sun acquisition and off-tracking to protect the PCA support structure from concentrated flux.

The SolarTrak can be operated in an automatic or manual mode. In the automatic mode, the controller continually recalculates the sun position and compares it to the actual orientation of the drive. When a difference exceeding a programmed limit exists, the drive position is updated.

The manual mode of operation can be enabled by a toggle switch on the controller's circuit board, by resetting an address in the controller memory through the data panel, or through the external communication bus. When the SolarTrak is in manual mode, a joystick on the circuit board can be used to move the drive mechanism as required.

SKI's control design also includes a provision for manually controlling the drive that is entirely separate from the SolarTrak controller. Should the controller malfunction, this permits manual movement of the dish to a safe orientation. This redundancy may only be used on early dish units until all the critical control component's reliability is established.

Additional hardware has been specified by SKI to support the SolarTrak. This hardware includes the motor power supplies, manual switches, mechanical limit switches, and related mounting hardware.

4.1.6 Controller Interface Hardware

Figure 4.1 illustrates the auxiliary hardware integration with the SolarTrak controller. Ten 0-5 VDC inputs provide information to the controller on axis position, axis direction, reference position, and end of travel limits for each axis.

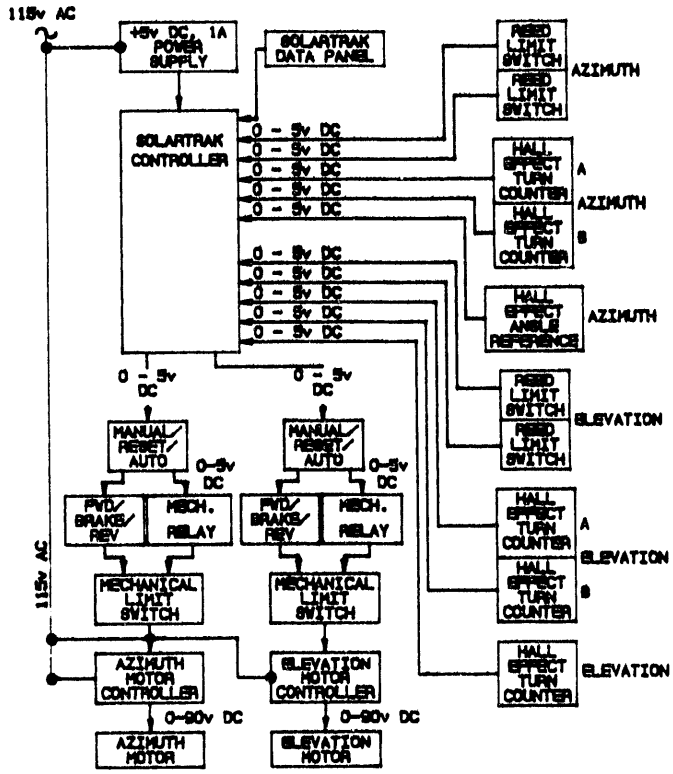

Figure 4.1 Solartrak Controller System Block Diagram

The shaft position, number of turns, and direction of rotation are monitored by one pair of Hall-effect sensors on each drive axis motor shaft. Actuating vanes on the motor shafts produce a quadrature signal in the switch outputs. One period of the quadrature signal represents one motor rotation. Therefore, the resolution of the drive axis positioning is equivalent to one quarter of a motor revolution. The gear-reduction ratio in the drive defines what actual angular positioning resolution is achieved. The azimuth drive uses a 33,000:1 reduction; one quarter of a motor revolution equates to 0.05 milliradians resolution at the concentrator. The elevation drive uses a gear reducer driving a jackscrew that, in turn, rotates a lever arm. Collector elevation angle is not a linear function of motor rotation. The SolarTrak controller compensates for this by using stored values that describe the geometry of the lever arm and the reduction ratio of the gearmotor and jack screw.

The SolarTrak also has stored values representing the angular limits of travel for each drive axis. These values serve as "soft" limit switches to avoid driving the collector too far in any direction.

To supplement the calculated drive position and drive limits, magnetically activated reed switches positioned at the end of travel for each drive stage as a safety precaution. If the controller should misinterpret the quadrature signal, the signal should be interrupted, or the controller suffers memory problems, the controller might not anticipate when the drive reaches the physical end of travel limits. These reed switches will override the controller and stop the drive movement to avoid physical damage to the dish.

One additional reed switch is placed at a precisely determined angular position on each drive stage. These two switches serve as references for the controller to verify that it is correctly calculating the drive azimuth and elevation angles. Each time the switch is activated, the drive position determined by the software will be compared to the stored reference switch location. If a discrepancy exists, the calculated value is reset.

Two sets of 5 VDC outputs provide motor drive signals, one pair for each drive axis. These outputs indicate which axis is to move and in which direction. The low power outputs control relays that control the motor power supplies. The power supplies control the acceleration and deceleration rates of the motors to minimize loads on drive train components. This also minimizes overshoot of the drive when it is making small adjustments in position. The power supplies also limit the maximum torque of the motor and motor speed to protect the components. The power supplies are pulse width modulated, regenerative controls. They are the most efficient type of industrial DC motor controller. They provide very smooth operation at low motor speeds. They also offer a high turndown ratio of up to 50:1 to permit smooth, controlled low speed movement for increased positioning accuracy.

The acceleration, deceleration, minimum speed, maximum speed, and peak motor current limits are set at the motor controllers, not by the SolarTrak.

The motors are 90 VDC, permanent magnet, totally enclosed, non-ventilated (TENV) units. These are common industrial motors with a long track record for reliability and accurate motion control. Since the motors will generally be running at a small fraction of the rated speed, integral fan cooled motors would not be effective. The non-ventilated types will provide longer life due to their design for passive heat dissipation.

4.1.7 Additional Control Hardware

SKI has taken a conservative approach to control design in order to assure that the dish does not become stranded in an unstowed position due to a control failure. The expense of these redundant controls can be easily justified to protect prototypical equipment and early market production equipment. Field experience will dictate which redundancies can be confidently eliminated to reduce the cost of future units.

In the auto position, the SolarTrak outputs are directly coupled to the relays controlling the motor power supplies. In the manual mode, these connections are interrupted. Manual switches may be activated to operate the motor power supplies. In this mode, the SolarTrak unit has no affect on the drive operation.

Because the SolarTrak unit is no longer monitoring the limit switches nor capable of interrupting the control signal to the motor power supplies, additional limit switches are mounted just beyond the reed limit switches to protect the drive during manual operation. These switches remain active in the automatic mode so that if the SolarTrak unit or the reed switches and their connections should fail, the drive remains protected. When the outer limit switches are tripped, the input signal to the respective motor power supply is interrupted. There is no way for a logic failure to permit driving past these limits. The outer limit switches also produce an alarm signal to the master controller. The control must be manually reset to drive the motors off of these outer limit switches.

4.1.8 Operation

There are three modes of operation selectable from the control panel: fully automatic operation, manual control via. the SolarTrak joystick, and manual control with panel switches bypassing the SolarTrak.

When on fully automatic, the SolarTrak controller has a default condition of active tracking. Depending on the time of day, the controller will either be in the night- stow position or will be on-sun. A wind switch input will cause the controller to go to the pre-programmed high-wind stow position, which may be different than the night time stow. A separate stow input will cause the controller to go to stow if the master controller detects insufficient insolation or a malfunction in the PCA.

Each time the controller changes from night stow to track or vice versa, it can be set to check the memory position registers against the physical position reference switches.

When power is first applied to the Solartrak or when a control signal instructs it to do so, the controller goes through a self-checking routine. The controller directs the drive through its

full range of travel until the angle reference switches are encountered. The current drive position is then reset, and the controller carries out its next instruction.

The controller also has a built-in routine to optimize the synthetic tracking algorithm based on feedback from an active sensor. Since the controller was originally designed for PV applications, a transducer signalling the true collector power output would have been used for this purpose. The optimization routine requires a full day of operation. The controller periodically moves the drive slightly ahead and behind the calculated azimuth and elevation positions to determine where the peak power output is achieved. The control algorithm is modified to apply these biases after the optimization routine is completed. For a solar thermal collector, using the collector output would probably not be appropriate for optimization. The Solartrak would not account for likely lags between drive repositioning and measured changes in the output resulting from thermal inertia in the receiver and engine. Instead, a direct normal pyrheliometer or other insolation measuring device could be used to supply a signal for optimization. Careful alignment of the device with the collector would be required. This routine is not required very frequently, possibly only once a year. The sensor unit could be dismounted between optimizations for use on other dishes.

4.2 Focus Controller

The focus of the dish is controlled by maintaining a constant pressure differential across the front membrane. Although the stainless steel membrane is pre-formed to a parabolic shape, the pressure differential across it does have a modest effect on the shape of the membrane. The nominal design pressure differential is 1000 Pa (4.2 inches water column or 0.15 psi). During dish start-up, the specific optimum differential is determined for the receiver position. The vacuum controller is set for the desired value. A vacuum in the optical-element plenum is created with a variable speed, multi-stage centrifugal blower. The controller monitors the plenum vacuum via a low-pressure diaphragm transducer and varies the blower speed as required.

The first 7-m optical element prototype had an adjustable speed blower set to run at a fixed speed. There was no active feedback to control the vacuum differential if conditions changed. This system was acceptable because, unlike the stretched-membrane heliostats, the dish is insensitive to wind speed and orientation. The stabilization vacuum was selected to assure this insensitivity (see Section 6.2). However, if the leakage rate of air into the optical-element plenum changes for any reason, the blower will not maintain the desired pressure differential. The pressure differential of a centrifugal blower operating at a fixed speed can be very sensitive to the flow rate. It is also sensitive to air density (which is affected by temperature, barometric pressure and humidity). Therefore, the current design uses a closed- loop feedback to maintain a constant vacuum differential rather than a constant blower speed.

The vacuum is sensed by a transducer with a large spring loaded diaphragm. A standard industrial process controller monitors the transducer signal and varies the blower speed through a PID algorithm. The transducer outputs a 4-20 mA signal. The controller outputs out a 0-10 VDC signal. The PID (proportional + integral + derivative) controller can be tuned to minimize fluctuations, due to system dynamics, and maintain close control of the stabilization pressure.

The controller has separate alarm outputs to signal excessive deviation from set point and high limit. The controller can also communicate bi-directionally over EIA-485 digital communications link, to reprogram or monitor internal settings.

Two vacuum blowers are used to provide redundancy for increased reliability. Normally, both blowers will be operating, following the same speed control signal. The blowers are plumbed in parallel with a check valve at each blower outlet. This mounting arrangement permits one blower to be shut down and replaced while the other is still operated. If one blower fails, the other blower will automatically increase speed to compensate for the reduced flow.

Vacuum blowers are standard industrial items with a motor, speed controller, and multistage centrifugal vacuum blower integrated in a single unit. The motor is an electronically-commutated brushless DC motor. DC motors offer simple speed regulation over a wide range of speeds. However, conventional DC motors use brushes to commutate the motor current to the armature, which have total operating life spans measured in hundreds, or at best, thousands of hours. The brushless design retains the speed control features with no brushes to wear. This unit also has built-in motor speed control circuitry that follows a 0-9 VDC control signal. Finally, the blower is a multistage, close tolerance unit that is necessary for the vacuum level required in this dish. Using a simple single-stage blower would require a much larger, heavier, and noisier blower and would result in a greater parasitic power usage. A vacuum pump is not cost-effective because of the relatively high volume and small differntial pressure required for the optical element.

The blowers operate on 110 VAC, single-phase power. Nominal blower power consumption is anticipated to be the same or less than the 7-m prototype, about 125 watts.

An activated, diaphragm high-vacuum limit switch will cut off power to the blower motors if the vacuum is too great. This protects the membranes and optical- element structure. The same switch sends an alarm signal to the master controller that will shut down the collector and notify the operator of a problem. This switch is a self-resetting device so that as the vacuum drops due to normal leakage, power will be restored to the blower motors although the alarm condition will remain set. The switch will cycle in this manner and will serve as a crude vacuum control until the problem is resolved. This prevents the vacuum from being entirely shut-off and leaving the unstabilized membrane susceptible to wind induced damage.

Most of the vacuum control components are mounted in a weather tight enclosure on the side of the azimuth stage of the drive. The vacuum hoses connecting the blowers to the optical element must only accommodate the elevation movement, which is much more limited than the azimuth rotation. Only four pairs of wire must run from the rotating azimuth stage to the pylon. These are: one pair for blower power; an alarm signal pair; a transducer output signal pair; and a PID controller speed control signal pair. The PID controller is mounted in the control enclosure on the pylon base to permit easier access for monitoring and adjustment.

4.3 Concentrator Testing and Calibration

A Beam Characterization System (BCS) developed by SNL was mentioned earlier during the discussion of methods for monitoring concentrator performance. This system (16) was developed for testing heliostats and was successfully modified to test dish concentrators also. It uses a video camera, digitizing software, and a flux target with integral flux reference gauge. For dish testing purposes, a water-cooled target is placed at the concentrator focal point. The BCS system measures the flux intensity pattern on the target while the dish is operating. For the first stretched- membrane optical element, two parameters were varied while measurements were made - the distance from the target to the membrane, and the level of stabilization vacuum. Comparison of the flux contours permitted selection of the optimum receiver position and stabilization vacuum.

The BCS is a very powerful and cost-effective tool for testing concentrators that could be used advantageously for production concentrators. Testing each dish as part of the start-up procedure would permit accommodation of changes in manufacturing variables. These could include general accumulated assembly tolerances and metal membrane shape variations due to initial pre-forming stress states and material property variations. The BCS results would define the optimum receiver placement and vacuum setting.

Periodic testing of operating dishes would also be valuable, at least until considerable operating experience has been gained. Actual operation of a stretched-membrane dish could result in changes in the optical performance.

5.0 PCA Support

The PCA support is the structure that supports the receiver, engine, and generator assembly at the focal point of the dish. The structure must prevent deflections from the weight of the PCA and from wind loads. Excessive deflections would cause the concentrated flux to spill out of the receiver aperture. This would reduce operating efficiency and could damage the structure near the receiver aperture.

5.1 PCA Support Configuration and Summary

The configuration selected is a nominally equilateral tripod (see Figure 5.1). The bases of the tripod legs attach to the optical-element ring. The top of the tripod legs attach to a support frame to which the engine assembly is bolted.

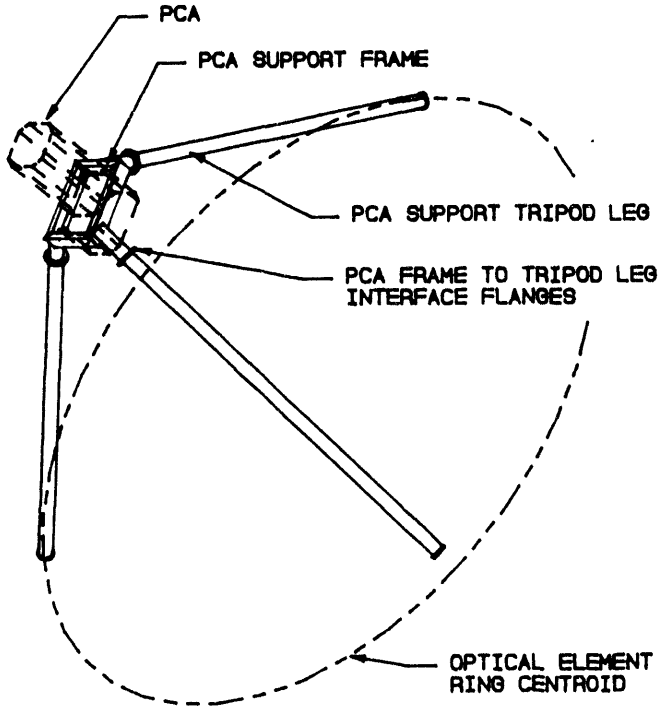

Figure 5.1 Final PCA Support Configuration.

The gravity and wind loads on the PCA and PCA support are transmitted through the tripod legs into the optical-element ring. To avoid high local stresses and deflections of the ring, the PCA attachment geometry was designed such that the loads act through the centroid of

the ring cross section. The actual attachment interface is a spherical bearing to minimize the imposition of moments on the optical element ring.

The PCA interface to the PCA support was designed to minimize bending loads in the tripod legs. The maximum loads on the lower two legs are compressive. Therefore, the legs must be designed as columns. Superimposed bending loads were minimized to assure stability. This was in part achieved by aligning the axes of the legs to pass through the center of gravity of the PCA.

The final PCA support design has three tubular steel legs. They attach to brackets at the optical-element ring by means of pins through spherical rod ends. The brackets attach to the outside of the optical-element ring and reach radially inward over the front surface of the membrane to pin to the ends of the tripod legs.

At the PCA, the legs bolt to circular flanges on three tubular stubs welded to the PCA support frame. The frame is rectangular steel tubing. The PCA mounts to four points on this frame. The frame has high stiffness to avoid imparting any twisting loads to the PCA internal structure.

5.2 Structural Analysis and Sizing

The system to be analyzed includes the PCA mounting frame, the three support legs, and the mounting brackets. Initially, it was not known that the tripod would be nearly equilateral or that the paired legs would be on the lower side of the dish. Use of a single lower strut and two upper legs was also investigated.

5.2.1 Design Loads

The position of the PCA is dependent on the receiver type. The PCA support was designed for the average position of the centers of gravity of a PCA with a pool boiler and one with a heat pipe. Both PCAs' design weight were estimated by the engine developer as 635 kg (1400 pounds) at the start of this contract.

The gravity loads in the PCA support members are a function of both the PCA support geometry and the dish elevation angle.

When considering the wind loads, the magnitudes were defined by classical aerodynamic drag formulae. Wind loads on the PCA were considered as a point applied load acting at the PCA center of gravity. Wind loads on the PCA tripod legs were analyzed as distributed loads.

For PCA Wind Drag

Force (drag)	= Cd * Area * P (velocity pressure of the wind)
Cd	= 1.6
Area	= 79.08" * 29.4" = 2325 sq.in.
P	= Wind speed ^ 2 * 0.00256/144 (psi) (wind speed in mph)

The deflections were analyzed over a range of elevation angle and a wind speed of 43 km/hr (27 mph). Stresses were analyzed for various elevation angles with a wind of 80 km/hr (50 mph) and 0 elevation for a wind of 145 km/hr (90 mph). The cases with the worst wind load conditions were selected by inspection and are listed in Table 5.1.

Table 5.1
Worst Wind Cases for PCA Analysis

Survival Conditions

Wind Speed km/hr (mph)	El (degrees)	AZ (degrees)
145 (90)	-25	90
80 (50)	45	90
80 (50)	90	0
80 (50)	90	180

Operating Conditions

Wind Speed km/hr (mph)	El (degrees)	AZ (degrees)
43(27)	0	90
43(27)	45	90
43(27)	90	90
43(27)	90	0
43(27)	90	180
0	0	NA
0	45	NA
0	90	NA

5.2.2 PCA Support Geometry

The coordinate system used in the PCA support analysis is described in Figure 5.2. The designers were predisposed towards a tripod design patterned after that used on the 7-m prototype. Some consideration was given to a guyed bipod design. For a bipod, loads on the optical-element ring from the two struts and the opposed braces would create a folding moment on the optical-element ring. Analysis of this approach required considerable

model changes and was not pursued due largely to budget and schedule constraints. Initial investigation did not show any reasons for a net increase in total structure efficiency with a bipod.

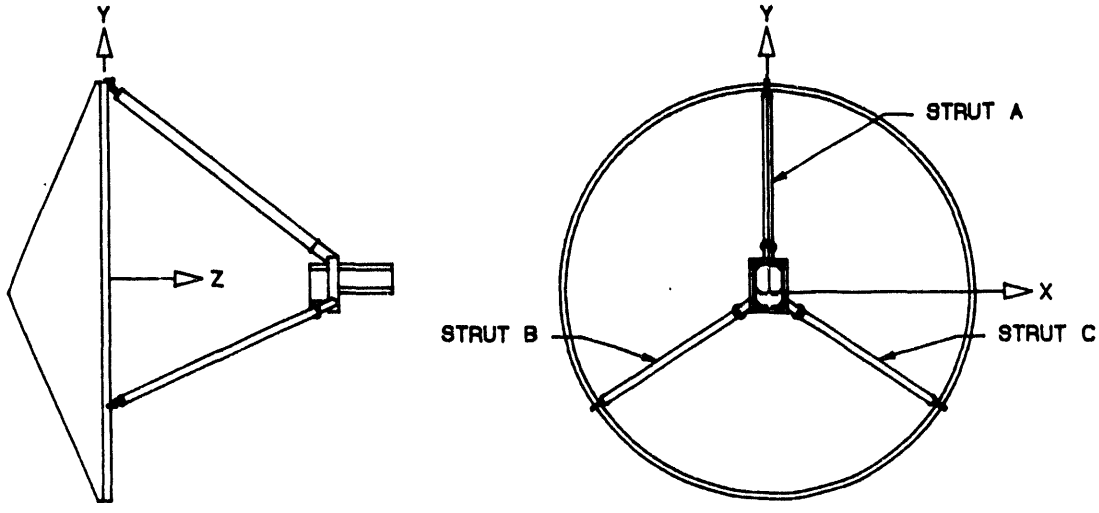

Figure 5.2 PCA Coordinate System For Analysis.

For the tripod approach, most of the geometry is determined once the design constraints are defined. These are:

Axis of tripod legs to pass through ring, cross-section centroid.
Axis of tripod legs to pass through average PCA center of gravity.
PCA frame to clear either type of PCA (pool boiler or heat pipe).
PCA to be supported at existing mounting plane.
Center of receiver aperture to lie on dish axis.
Center of receiver aperture to be 206.3" from ring plane.

The only geometric variable investigated was the angle separating the two paired tripod legs. The 7-m prototype design angle of 120 degrees was established as a baseline. Other angles from 22 to 120 degrees were investigated. Also analyzed was the effect of positioning the two paired legs at the top of the dish.

The effect of increasing the angle is to increase the effectiveness of the paired legs in resisting side wind loads. A side wind load on the PCA creates a couple of effects; different loads in the paired legs are caused which sum to a net reaction equal and opposite to that couple. This effect is shown in Figures 5.3, 5.4 & 5.5. In the first Figure, there is no side load from the wind so both paired legs have the same load. In figures 5.4 and 5.5, the 43 km/hr (27 mph) side wind causes opposite reactions in the paired legs. The wider spread angle results in lower loads because of the greater moment from the dish vertical center line at which the reactions occur. The top leg load does not depend on the spread of the paired legs.

Note: In these figures the elevation angle scale extends up to 90 and back down to -25 degrees. The curve from 90 to -25 degrees represents a PCA support tripod with the two paired legs at the top of the dish.

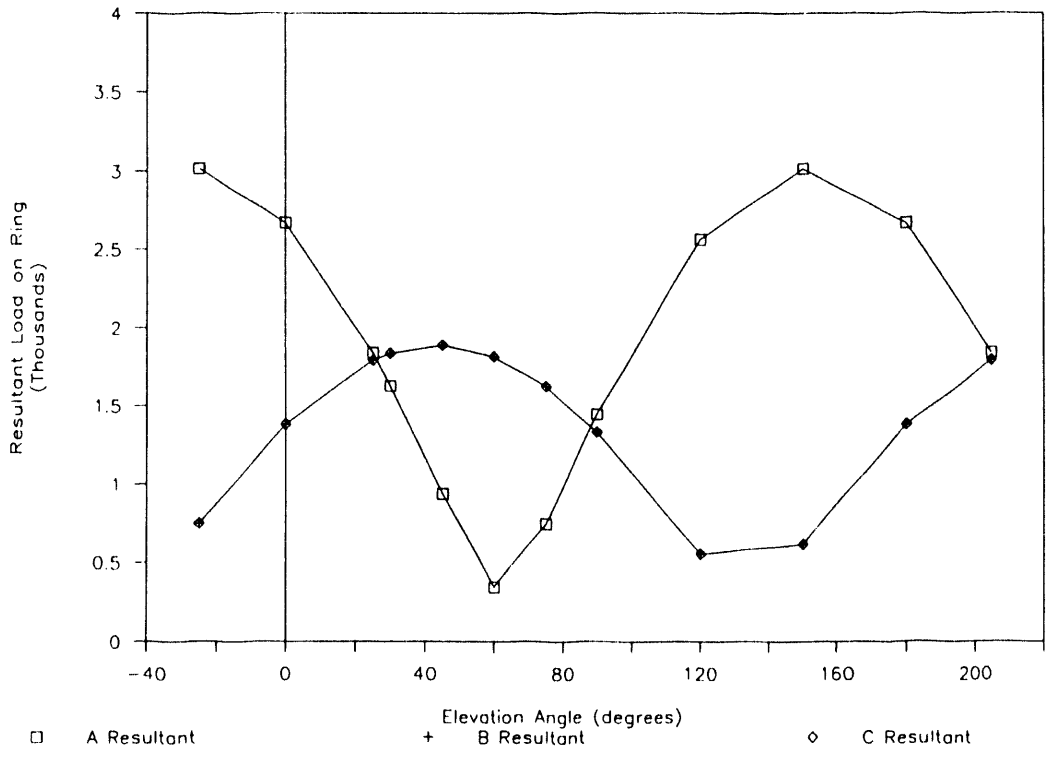

Figure 5.3 PCA Support Strut Load on Optical-Element Ring, 112 degree Spread, 0 km/hr Wind.

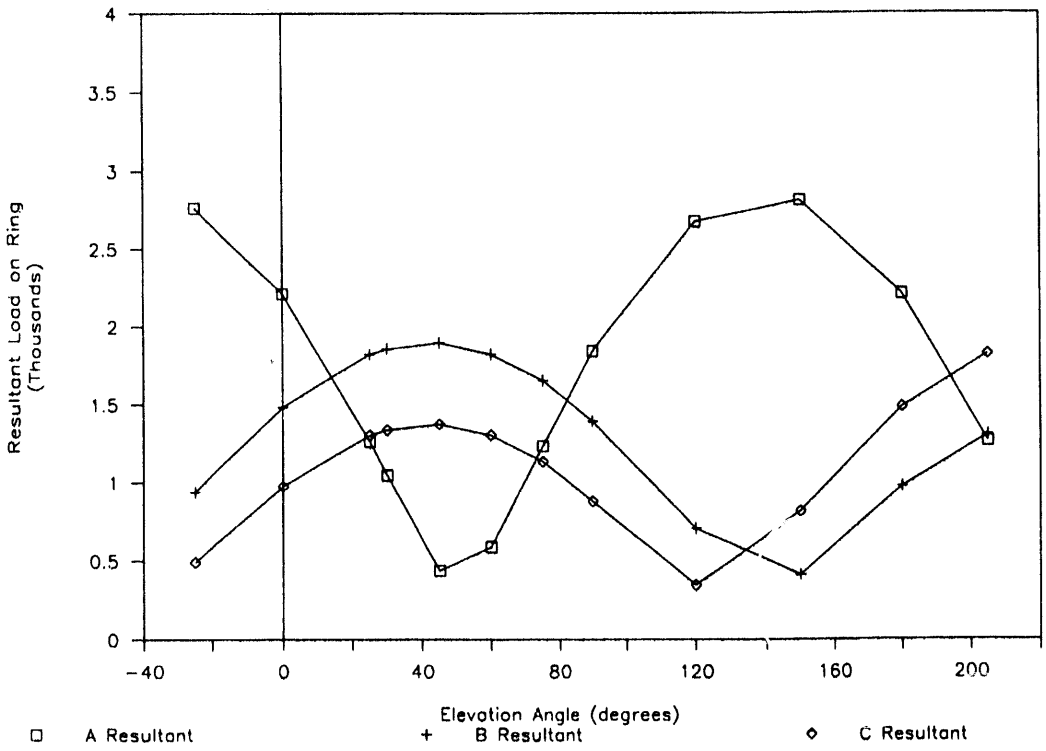

Figure 5.4 PCA Support Strut Load on Optical-Element Ring, 44 degree Spread, 43 km/hr (27 mph) Wind.

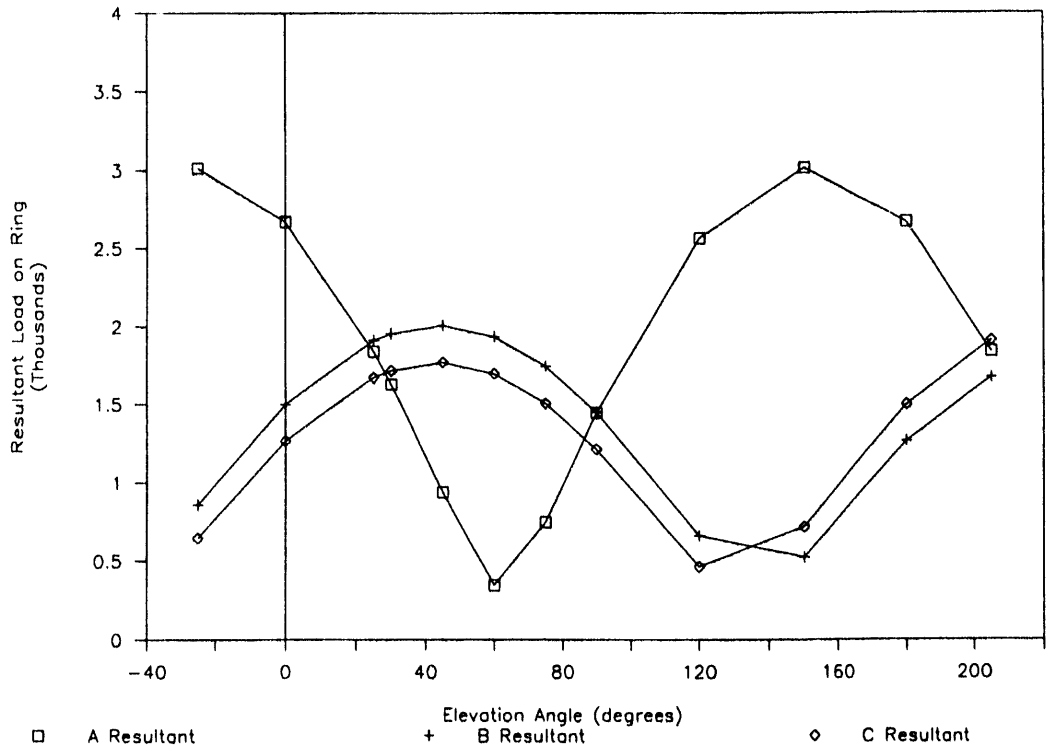

Figure 5.5 PCA Support Strut Load on Optical-Element Ring, 112 degree Spread, 43 km/hr (27 mph) Wind.

Limiting the PCA support leg reactions on the ring is significant because lower concentrated loads mean reduced stress and deflections in the optical-element ring. Figures 5.6 and 5.7 show that under worst case operating conditions, the paired legs' load on the ring can exceed the top leg load for narrow spacings. The wider spacing selected keeps the paired leg loads on the ring less than the peak load from the single leg. This avoids increasing the ring size to withstand the paired ring loads beyond the base size necessary for the single leg load.

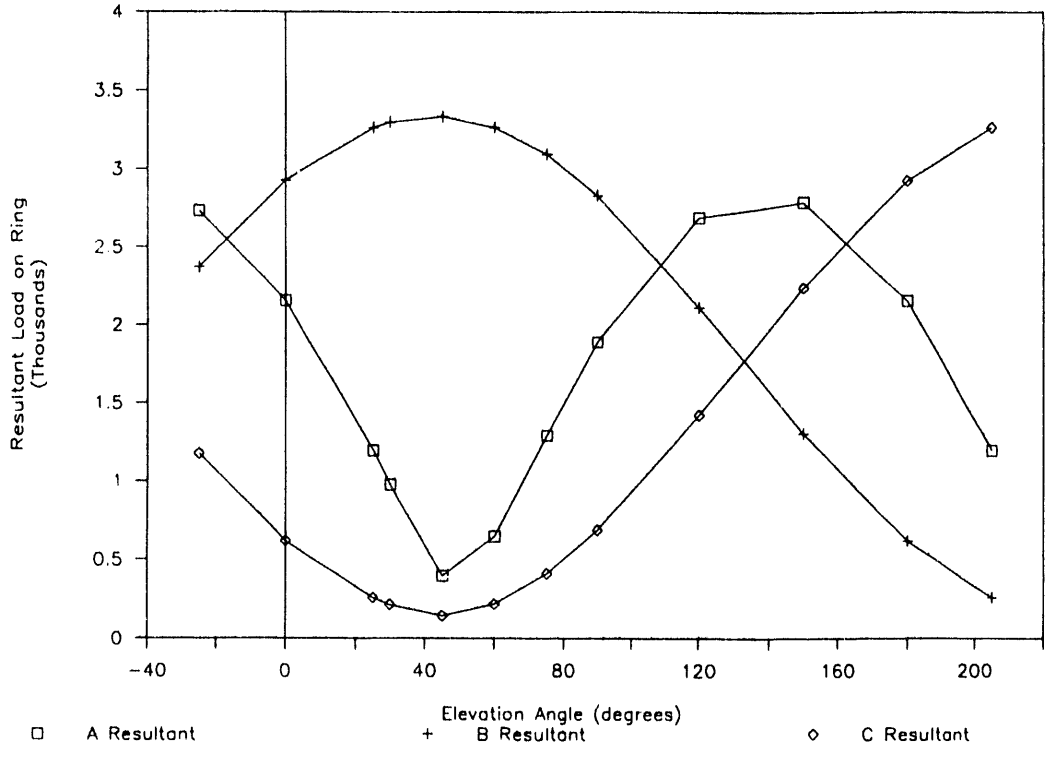

Figure 5.6 PCA Support Strut Load on Optical-Element Ring, 22 degree Spread, 80 km/hr (50 mph) Wind.

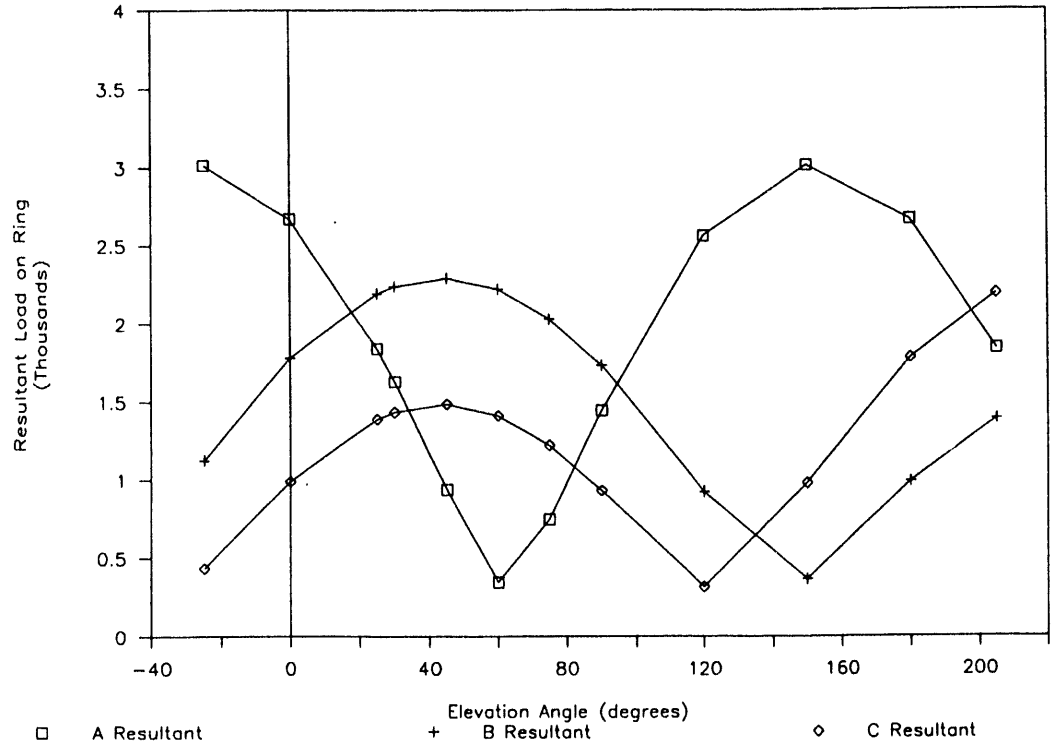

Figure 5.7 PCA Support Strut Load on Optical-Element Ring, 112 degree Spread, 80 km/hr (50 mph) Wind.

5.2.3 Structural Analysis

After the loads were determined, structural sizing was estimated based on AISC limitations. Detail analysis by finite element (FE) code was performed by a structural engineering firm who also performed the design detailing (17).

The driving factor in initial tripod leg design was satisfaction of the AISC allowable column compressive stress. A 0.23 m (9") O.D. x 3.2 mm (0.125") wall tube satisfied the code with an acceptable amount of shading of the reflective membrane. This was used as the starting point for the FE analysis.

The goal of the analysis was prediction of the specific response (deflection and stresses) of the support structure to gravity and wind loads. Stresses were limited to those allowable under the AISC code (see Table 5.2). Note that safety factors are very high. This results from the design being driven by receiver deflections in the X-Y plane.

Table 5.2
Allowable and Actual Stresses
During Survival Conditions (145 km/hr, 90 mph)

		ACTUAL		ALLOWABLE	
		(MPa)	(psi)	(MPa)	(psi)
Main strut.	bending stress	16.0	(2319)	159	(23100)
	compressive	1.8	(256)	25.8	(3748)
PCA mounting frame					
	bending stress	17.7	(2566)	190	(27600)
	compressive	0.8	(115)	181	(26220)
	shear, torsional	10.9	(1581)	127	(18400)

The important deflection is that of the receiver aperture. Therefore, the FE model was created with a phantom element that resulted in one node being located at the aperture center. Deflections and translations at this node were analyzed to ensure they were less than the limits shown in Table 5.3. The loaded model is shown in Figure 5.8 with exaggerated deflections superimposed on the undeflected model geometry.

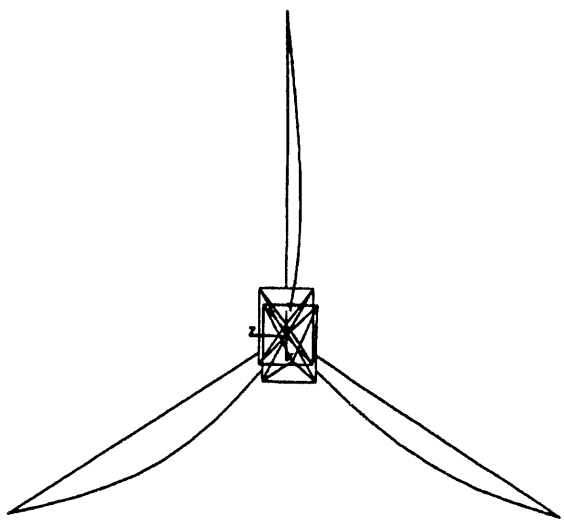

Figure 5.8 Pictoral Representation of PCA Support FE Analysis Results. (Exaggerated deflection.)

Table 5.3
Allowable and Actual Deflections and Rotations
Selected Node at Dish Focal Point at
Operational Conditions (43 km/hr, 27 mph)

	GOAL		ACTUAL	
Deflection in Z	+/- 13 mm	(0.5")	0.2 mm	(0.009")
Deflection in X-Y plane $(x^2 + y^2)^{0.5}$	= < 3.2 mm	(0.125")	3 mm	(0.121")
Rotation about X	+/- 15 mrad		2.2 mrad	
Rotation about Y	+/- 15 mrad		0.2 mrad	
Rotation about Z	no limit		NA	

The PCA support frame member's size was determined by the fabrication requirements rather than by optimum size to limit deflections. The frame member's height was increased from the calculated optimum size to interface efficiently with the tripod legs. The large diameter of the legs and the oblique angle at which they attach require a large area for attachment. The frame's overall dimensions were selected to permit the entire PCA to fit within the interior dimensions of the frame. This will permit some adjustment of the PCA's exact distance from the dish vertex if necessary. Spacers or standoffs from the four PCA mounting gussets may be used for this purpose.

5.3 Detail PCA Support Design

All steel construction was used. Plates and structural shapes are A36 steel; round and rectangular tubing are A53B and A500B, respectively. The PCA structure was designed to eliminate field welding. Field assembly of the four components requires only hand tools.

Each support leg is terminated at the ring end with a spherical bearing rod end (see Figure 5.9). The rod ends have male, left-hand threaded shanks that thread into an intermediate threaded bushing. The external threads on this bushing thread into a welded adapter on the end of the support strut. This combination provides a turnbuckle action to permit adjustment of the length to compensate for fabrication tolerances.

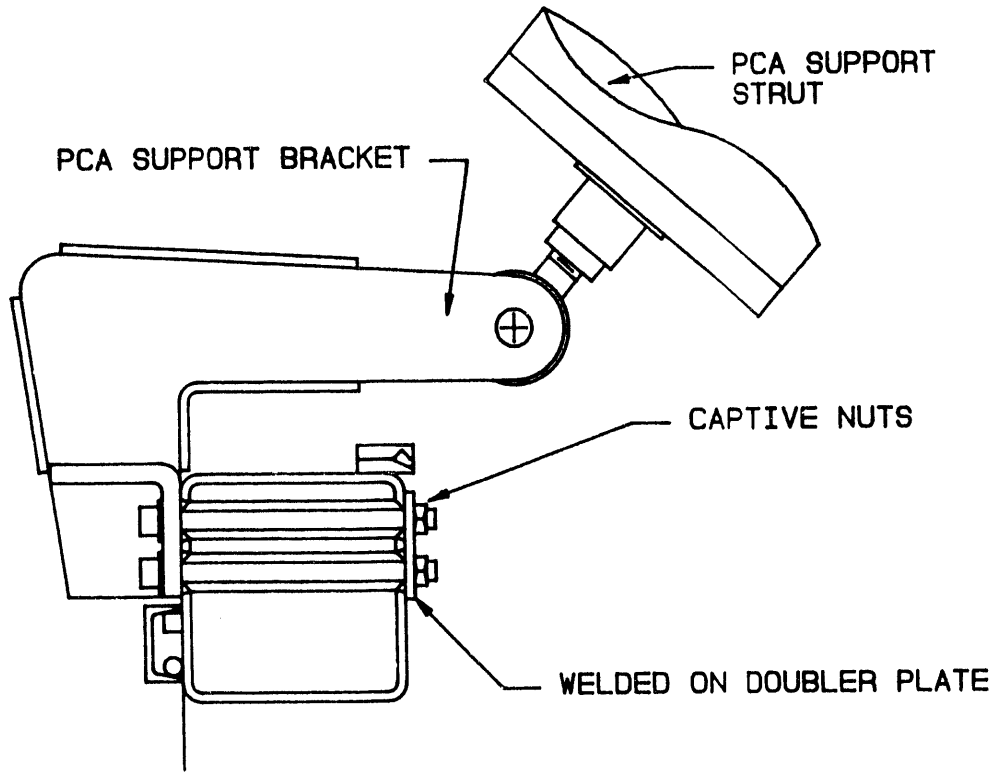

Figure 5.9 Detail of PCA Support Strut to Optical-Element Interface.

The final geometry of the PCA tripod has the two paired legs 112.5 degrees apart. This places each mounting bracket equidistant between adjacent spokes for easy access during fabrication and assembly. Each bracket is a simple weldment. The weldments bolt onto the ring during final assembly. A removable bracket is required to permit easy layout of the membranes during final assembly. The bracket bolts insert into tubes welded into the optical-element ring to distribute the PCA loads. A welded nut plate on the inside of the ring permits bolt tightening without requiring wrench access to the nuts.

At the PCA end, the support legs attach to flanged stubs on the PCA support frame. The flanges use four bolts for leg attachment. The stubs are cut at the flangeless end to mate with the PCA support frame rectangular tubing for welding.

Tolerances on individual pieces may be standard fabrication values. Final assembly and welding of the stub flanges to the support frame should be jigged to maintain correct PCA support leg rod end position. The chordal separation, the radial position, and the "Z" distance from the rod ends to the support frame all require control during final shop assembly. Tolerances of +/- 3.2 mm (1/8") on assembled dimensions are acceptable. This should not be difficult with proper fixturing.

After the prototypes are confirmed, a large jig should be fabricated and machined to permit stub tube welding without assembly of the entire PCA support. If only a few assemblies are being built, the fixture will not be cost-effective.

Surface finish of the PCA tripod is hot-dip galvanizing. The PCA support frame will require drain holes for the dipping operation. These holes will be tapped and plugged prior to field installation.

6.0 Optical Element Analysis

The basic configuration of the optical element remains the same as it was in the 7-m prototype dish. That is, the optical element looks much like a bicycle wheel. A ring is attached to a central hub with two sets of spokes. The optical element, like a bicycle wheel, makes efficient use of structural material and is lightweight and stiff.

The full-scale optical element was analyzed and sized to withstand survival loads without yielding or buckling and to be adequately stiff during operation to ensure good optical performance.

This section covers the analysis and sizing of the optical element and its components. This includes the selection of 10.4 m as the concentrator diameter, selection of the number of spokes, ring size and shape, hub size and more. Stress, deflection, stability, and natural frequency of the concentrator are all discussed.

6.1 Selection of Dish Aperture Area

This concentrator was designed to mate with a 25 kW electric Stirling cycle heat engine that is currently under development by others. The concentrator was originally designed for a "nominal" 25 kW system and was 11.7 m in diameter. It was later reduced to a 25 kW "peak" because of uncertainty in the capacity of the receivers being developed for the heat engine systems. After review with SNL personnel, it was agreed that the dish would be sized such that the maximum net thermal power into the receiver would not exceed 60 kW.

The analytical solution presented by Jaffe (18) was incorporated into a spreadsheet code entitled EFF (see Appendix D). This tool was used for sensitivity checks and trade-off decisions. For the cases of interest, it compared well with the SNL code used for confirmation.

Final confirmation was done using CIRCE (19) for the concentrator optics analysis and a receiver loss model developed by Mancini (20). The following list summarizes the important variables used for this analysis:

Incident Flux	1050 W/sq m	Assumed
Slope Error	2.5 mrad	7-m tests
Specularity	1.5 mrad	Measurement
Tracking Error	0 mrad	Assumed
Reflectivity	82%	Measured
Blocking & Shading	10%	Design
f/D	0.6	Design
Receiver Temp.	750 C	Assumed
Ambient Temp.	21 C	Assumed

The following list summarizes the characteristics of the selected configuration:

Concentrator Diameter	10.4 m
Receiver Aperture Radius	0.13 m
Receiver Gross Thermal Input	65.6 kW
Receiver Net Thermal Input	60.4 kW

A concentrator diameter of 10.4 m (85 sq meters) met the requirements of the 25 kWe system.

6.2 Selection of Stabilization Pressure

A stabilization pressure of 0.15 psi was selected to prevent the metal membrane from being lifted in a high wind. A high wind from the rear reduces the magnitude of the net pressure on the membrane. The selected stabilization pressure is equivalent to the dynamic pressure of a 145 km/hr (90 mph) wind and is adequate to prevent a lifting pressure on the membrane up to this wind speed.

Basing the stabilization pressure on wind speed departs from the method used previously on the 7-m optical element. That unit was designed to stow facing the zenith, and wind loads were much lower. The design criteria for it was the pressure required to pull the plastic membrane into intimate contact with the metal membrane.

The stabilization pressure selected for the 10.4-m dish is adequate for use with a polyester membrane 0.09 mm (3.5 mils) thick or any membrane with equivalent stiffness. Ref (21) describes the method for such calculations.

6.3 Rear Structure Analysis

An alternative means of closing the rear of the plenum was investigated. Early development of the dish called for the rear spokes and membrane to serve the purpose. The membrane was used to transfer the pressure load to the spokes. The spokes carried the lateral load as tension to the ring. This induced compressive stresses in the ring requiring additional ring material.

SKI investigated a geodesic dome structure to reduce the magnitude of ring loads. A geodesic dome is a set of compression/tension members connected in a triangular pattern. Each member is straight and short relative to the dish diameter. The structure is naturally contoured in a spherical shape. A membrane would be draped over this structure. The plenum pressure loads would be carried by compression in the dome members to the ring. The net loads on the ring from the dome would be radially outward and upward and would almost directly cancel the radial inward and downward load induced by the front membrane. If the loads ideally cancelled, the ring stresses could be reduced by approximately 50%. This would correspond to approximately 727 kg (1600 lbs) saving in ring and spoke weight.

The potential advantage of this is offset by the disadvantages of high dome weight and complexity. SKI obtained estimates from geodesic dome manufacturers for applicable domes. The estimated weight for a steel dome of 10.4-m diameter was 1140 kg (2500 lbs). Even allowing for some conservatism in the dome design, there is a net weight penalty for using a dome. The dome would also add to the total number of parts and to the complexity of the dish. This approach was not pursued further.

6.4 Initial Sizing

Numerous design variables were evaluated during the initial sizing of the optical-element components. Each of these variables (including such things as the number of spokes, initial spoke tension, and membrane attachment points) were evaluated in terms of their impact on the overall optical-element design. The goal was an optical element that is lightweight and manufacturable at a low cost.

This initial sizing was done with mathematical structural models in spreadsheet format developed for this purpose. These models were limited in that they were pseudo axisymmetric representations of the optical element. They did not include point loads from the PCA supports or the non-uniform portion of wind loads, but did include the point loads of the spokes. Detailed and asymmetric analyses were performed as the final step for the selected design.

An assumption was made that the optical element is a stress driven rather than a deflection driven design. While the pseudo axisymmetric model was adequate in predicting approximate stress levels, it did not provide information on major ring/membrane deflections. Deflections were analyzed after all components were sized.

This section of the report describes the initial sizing of the optical element. It first describes the models used for the pseudo axisymmetric analysis and then describes the analysis itself.

6.4.1 Models and Approach

The sag of the rear spokes and their corresponding loads were determined with a modified version of an analytical solution developed by NREL (22). It is assumed that the pressure acting on the rear membrane is carried to the spokes, rather than directly from the membrane to the ring and hub. This results in a triangular load distribution along the spoke. The solution was originally coded in Task 2 of this project and was shown to predict deflections within 3% of both finite element models and measurements of the 7-m diameter prototype (21). The code (now called SPOKESAG) has been expanded to include calculations of the resulting gap between the front and rear membranes as a function of membrane/ring/spoke initial geometry, spoke properties,and pressure load. (Refer to Appendix D for more complete information on the codes.)

The method of determining the initial ring stress is based on super position of stresses from the various sources using classical solutions from Roark (13). The analytical model developed for this is called RINGSZ. This model calculates ring stresses based on variables such as the number of spokes, ring size, front-membrane attachment point, rear-spoke attachment point, departure angle of the spokes, wind speed/direction, and stabilization pressure.

Loads enter the ring through the rear spokes and the front membrane. The front spokes also induce a load in the ring, but only as a reaction to the other two loads. The resulting ring loading can be envisioned as a set of loads acting through the ring centroid. See Figures 6.1 and 6.2 for actual and modeled load geometry. The membrane causes a distributed radial and out-of-plane (out of the plane defined by the ring) load as well as a distributed moment acting to turn the ring inside out. The spoke loads combine to act as point loads both radially and out-of-plane, as well as point moments.

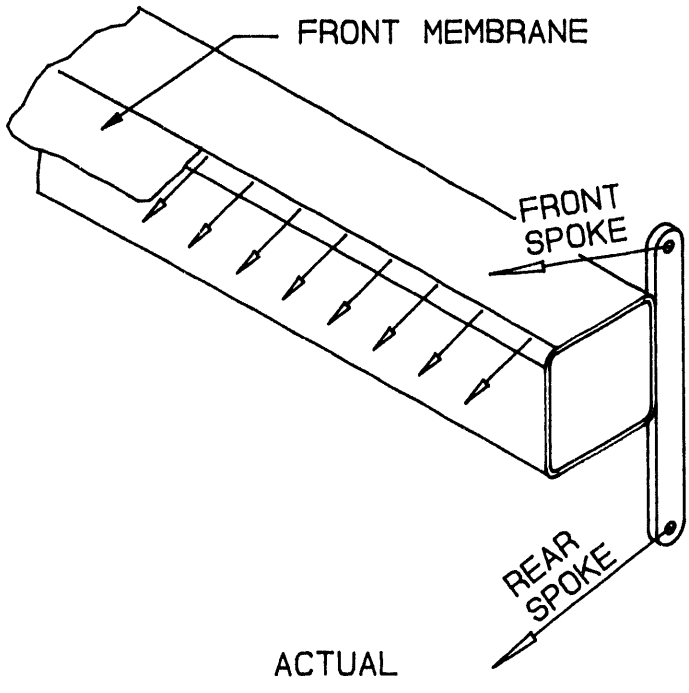

Figure 6.1 Actual Ring Load Geometry

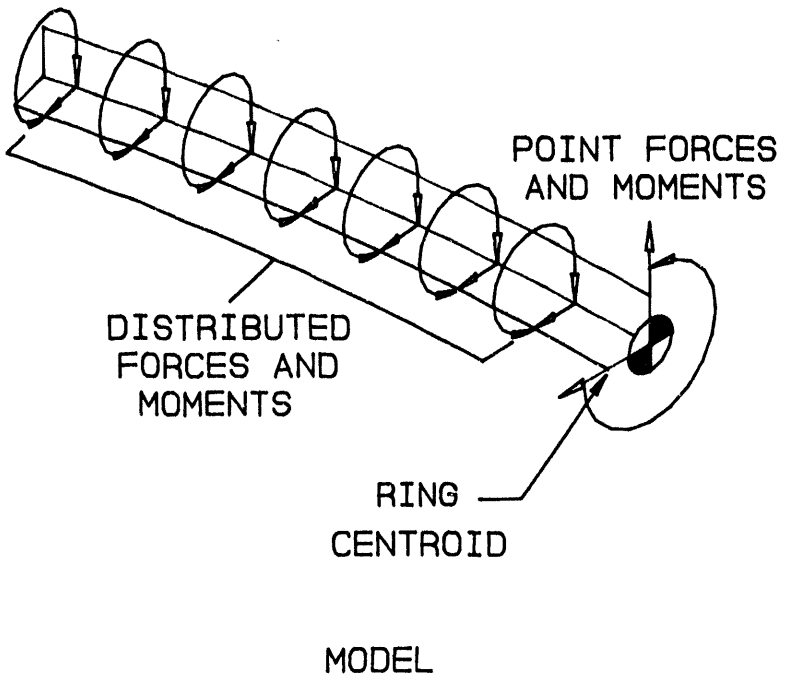

Figure 6.2 Ring Loads as Modeled.

Loads from the PCA support and the non-uniform component of the wind are not modeled. The magnitude of the front membrane load at the ring is assumed to be that which provides static equilibrium of the membrane while acting in the plane of local membrane. That is, the membrane is assumed to carry no significant loads other than tension. Another assumption is that the wind loads occur as a gust and that the control system does not respond quickly enough to compensate. In this way, the wind pressure is assumed to act on the front membrane for a front wind and on the rear membrane for a rear wind.

The loads are carried by the ring in four ways. First and most significantly, the radial loads are carried as direct compression in the ring. Second, all moment loads are resisted by "bending across the cross-section," which is a stress pattern identical to out-of-plane bending of a beam. If the top of the ring is rolled in, the top fibers of the ring experience compression and the bottom fibers experience tension of the same magnitude. No stress is induced at the neutral axis. Third, point radial loads induce in-plane bending of the ring section. Of less significance, the out-of-plane, distributed load creates out-of-plane bending loads. The resulting radial displacement of the ring from these combined loads is also calculated. This displacement is of much smaller magnitude then that caused by the PCA loads.

RINGSZ incorporated the rear-spoke load calculation routine from SPOKESAG, thus allowing direct input of stabilization pressure, wind speed/direction, and spoke properties. (See Appendix D for more details of RINGSZ.)

6.4.2 Analysis

Each significant design variable was evaluated in terms of its impact on ring stress (and weight). Limits were placed on each variable for practical reasons. For instance, an ideal low-stress ring would have all spokes and membranes acting through its centroid. This creates unworkable interference problems. Thus, the attachment points are separated from the centroid. Selection of the specific locations for these points were some of the most important design variables.

Figure 6.3 shows shows stresses are developed in the ring under various wind conditions based on the RINGSZ model. The case shown is a 0.15 x 0.15 m (6 x 6-inch) ring with all other variables as established for the final design. The stresses are representative of those that would occur at mid span between spokes at the top inside corner. The peak stress is the negative arithmetic sum of the absolute values of the stress components. This value represents the highest compressive stress in the ring without regard to whether it occurs at the top inside corner of the bottom inside corner.

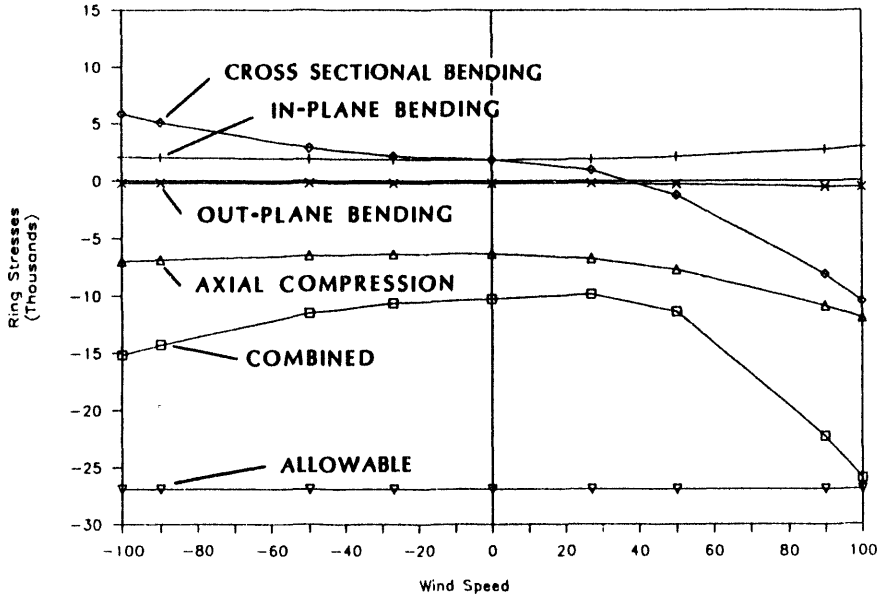

Figure 6.3 Ring Stress Components as a Function of Wind Speed.

As shown in Figure 6.3, the out-of-plane bending stresses are low. These stresses are caused by the out-of-plane distributed load of the front membrane being carried as bending to the adjacent supports (spokes). The in-plane bending stress is also relatively small and is caused by the radial point load at the spoke attachments. The axial compressive stress is the uniform stress in the ring caused by the sum of all radial loads acting on it. This is a significant stress and represents 60% of the peak stress with zero wind. The axial compression increases as the front wind speed increases because of the increase in the radial components of the front

membrane load and the front spokes. The tension in the front spokes increases as a reaction to the front wind. The compressive load is relatively insensitive to rear wind for several reasons. First, the drag coefficient and corresponding pressure load is less for a rear wind. Second, some of the loads are carried directly from the membrane to the rear hub without passing through the ring. Third, the front spokes react to the wind load by decreasing their load, thus reducing the radial load on the ring. The cross-sectional bending stress is another important component to the peak stress. With no wind, there is a slight net moment on the ring causing an outward rotation of the top ring surface. As the front wind speed is increased, the load from the front membrane rolls the top of the ring inward. With a rear wind, the combination of the rear spoke loads increasing in tension and the front spoke loads decreasing in tension causes the ring top to roll further outward. A line has been included to show the maximum allowable ring stress. Note that the maximum design wind speed is 145 km/hr (90 mph).

The rectangular ring section is an appropriate member for carrying the variety of loads. The high-cross-sectional bending load requires a high out-of-plane moment of inertia. The in-plane bending load is high enough to require a significant in-plane moment of inertia. Axial compression is dependent only on cross-sectional area, but shape of the member. A circular not the cross-section would be structurally more efficient, but would present competing interface/attachment problems.

The location of the attachment of the front membrane to the ring was defined entirely by hardware limitations. No simple low-cost concept was developed for attaching the membrane to the ring that would put the loads close to the centroid. Several ideas were considered, but were rejected because of complexity and cost. The concept used for the 7-m prototype worked well and is relatively simple. This concept was selected for the 10.4-m dish as well. It places the attachment point 3.2 mm (0.125 inches) up from the top of the ring surface and 6.3 mm (0.25 inches) inside the inner face of the ring.

The ring wall thickness was set at the minimum value that would not distort excessively during the rolling process. The tube bender who successfully rolled the ring for the 7-m prototype suggested 6.3 mm (0.25 inches) as the minimum for the 10.4-m dish. This value is dependent on the bend radius and the height and width of the tube. It is assumed that the steel is formed while it is hot. Web buckling was confirmed not to be an issue for the ring based on analytical techniques by Timoshenko (23).

The length of the hub affects the departure angle of the spokes at the ring and also the ring loads. A longer hub would allow wind loads to be carried with less resulting radial load on the ring. It would also allow more clearance between the front and rear membranes. A competing effect of a longer hub is that it would block more reflected sunlight from entering the receiver. It would also increase the gravity moments on the dish drive. Both issues are significant. These issues were considered in selecting the hub length for the 7-m prototype (although hub bending loads were not as high). Directly scaling the 7-m hub length for the 10.4-m dish put the end of the hub just into the region of concentrated flux. Further extension did not seem reasonable.

The benefits to the drive and pedestal of a shorter hub were not weighed because of the sequencing of design tasks. For these reasons, the hub was scaled directly from the 7-m prototype.

The number of spokes was selected after qualitatively weighing the relative disadvantages and advantages. The disadvantages related to having a large number of spokes are increased blocking and shading of the sunlight. Some incident rays are shaded by the front spokes prior to reaching the reflector. Some reflected and moderately concentrated rays are blocked prior to reaching the receiver. The total impact represents approximately 10% of the available energy even with flat spokes. The weight and cost of the spokes also increases with number. In theory, the total load carried by all spokes is constant. Therefore, the sum of the cross-sectional area of the spokes can remain constant. Thus the weight of all the spokes would be independent of the number. The weight and cost of the spoke brackets and termination hardware increases with spoke quantity, however.

Ring stress is reduced by increasing the number of spokes. With an infinite number of spokes, there would be no point loads on the ring, eliminating in-plane and out-of-plane bending loads. These loads represent approximately 15% of the maximum ring stress with 32 sets of spokes (based on the pseudo axisymmetric ring modeling.)

Sag of the rear membrane betwe rear spokes is reduced with a larger number of spokes. Avoiding contact between the f rear membranes was a limiting design constraint for the 7-m prototype and was initi ght to be a constraint for the 10.4-m unit. The model used to predict the sag for the 10.4-m dish serves only as an approximation. Therefore, there was benefit of confidence in keeping the span on the 10.4-m dish close to that on the 7-m prototype, which had a known and acceptable sag. The span between spokes was 0.91 m (36 inches) on the 7-m prototype. This was judged to be excessive in terms of blocking/shading and cost/complexity and 32 sets of spokes were selected, corresponding to a 1.02 m (40 inches) span.

The means of predicting sag of the rear membrane between the spokes was simply a scaling relation using the measured sag on the 7-m prototype as a data point. Membrane properties and the magnitude of initial slack were assumed to be the same for the 10.4-m dish as for the 7-m. The relationships between sag, span, and pressure were assumed to be the same as for axisymmetric membranes having initial tension under uniform pressure. Murphy has shown that the sag for such a case is a function of the pressure to the one third power and the span to the four thirds power (24). The two cases are not entirely similar. The rear membrane is supported by spokes on two sides and the ring on the third. The resulting membrane shape is compound but far from axisymmetric. The initial slack in the rear membrane is unavoidable and makes the difference between the cases more significant.

The front spoke is attached to the ring at its top surface and 25-mm (one inch) in from the outer edge. Analysis showed that moving the spoke attachment farther in would reduce the

membrane clamping hardware. Figure 6.4 shows the ring stress components if the attachment were .15-m (6 inches) radially inward from the outer edge. Note the marked reduction in cross-sectional bending stress with a front wind as compared to that of Figure 6.3 presented earlier.

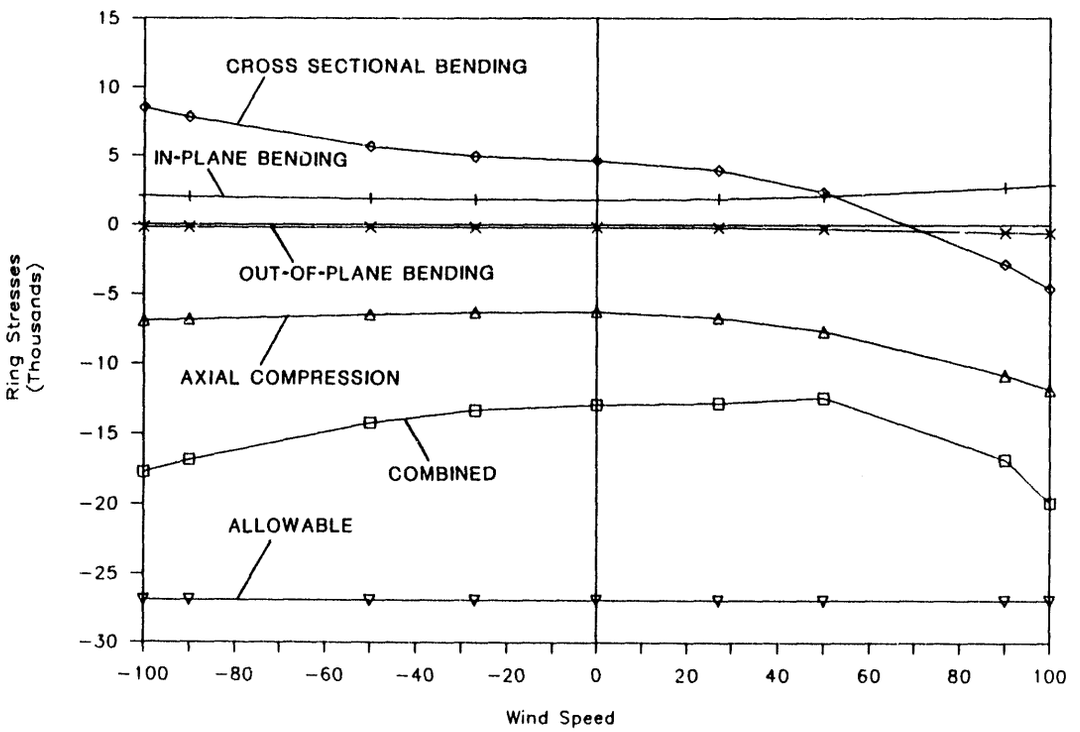

Figure 6.4 Ring Stress if Front Spokes were Located Farther Inward.

The location of the attachment of the rear spoke to the ring was selected to be 0.29 m (11.5 inches) down from the top surface of the ring and 19 mm (0.75 inches) radially inward from the outer ring edge. The 19 mm (0.75 inches) was selected to provide compatibility with the appropriate spoke bracketing concept used on the 7-m prototype. Initially, the distance from the top surface was kept at a minimum to reduce the size of the moment arm through which the rear spokes induce moments into the ring. As the ring design evolved, this distance was increased so that the rear spokes could be used to counter moment loads from the front spokes and membrane.

The properties of the rear spoke affect the sag of the spoke and the loads it induces into the ring. A very soft spoke will sag more than a stiff one, thus allowing more efficient alignment of the resulting load vector and imposed load. (This same effect can be seen by the high stresses created in a hammock that is tightly strung between two trees rather than loosely strung.) The modulus of elasticity and the initial tension both contribute to its stiffness. The modulus of elasticity is an effective modulus based on a combination of the spoke and a spring-gap element. The variation of the effective modulus has a significant effect on the ring stress under rear wind and no wind conditions, but has little effect for front wind cases. Figure 6.5

demonstrates this. The ring stress (shown here as a ratio of the peak ring stress to that of the allowable ring stress) are plotted against effective spoke modulus. Note that the lowest stress can be obtained from soft spokes, but no significant benefit is gained by reducing the modulus much past the point where the top two curves cross. The insensitivity shown in the front wind conditions is caused by two stresses canceling one another. As the spoke modulus is decreased, the reduced rear spoke load decreases the axial ring compression, but allows the ring to roll farther inward (on the top side). Thus, the cross-sectional bending stress increases. The selected modulus is 1034 MPa (1.5E6 psi) (with a 130 sq. mm (0.2 square inch) cross-sectional area).

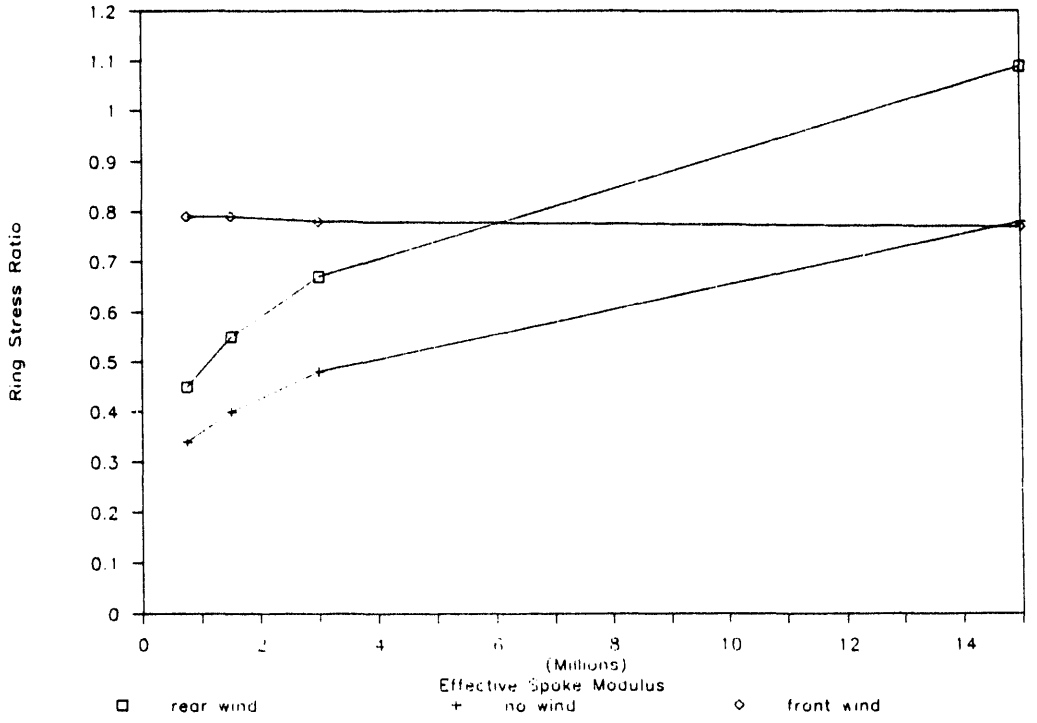

Figure 6.5 Ring Stress as a Function of Effective Rear Spoke Stiffness

Similar effects are seen when the initial tension is varied. The peak ring stress is insensitive to small variations in initial tension. The minimum initial tension is defined by that required to prevent the front membranes from going slack in high rear wind conditions. The selected tension of 6600 N (1500 pounds) avoids this.

No contact will occur between the front and rear membranes. Figure 6.6 shows the clearance between the front (parabolic) membrane and a rear spoke. This is a scale drawing of an entire rear spoke under load showing

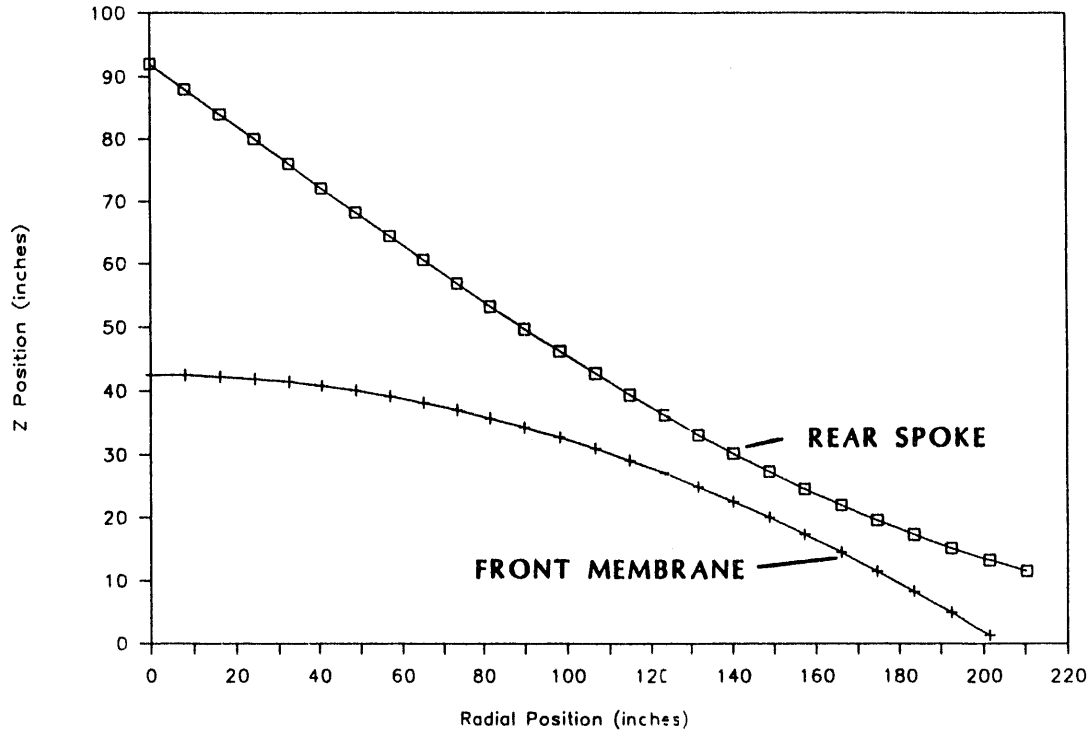

Figure 6.6 Rear Spoke-to-Front Membrane Clearance

its relative position to the front membrane (shown facing down). This data was developed with the SPOKESAG model described earlier. The maximum spoke sag is 200 mm (8.0 inches) and the minimum distance between spoke and membrane is 180 mm (7.2 inches). The rear membrane sags approximately 66 mm (2.6 inches) between spokes. The closest the two membranes come together is 117 mm (4.6 inches). Under a worst case rear wind gust, the gap would reduce to 52 mm (1.9 inches). The gap between membranes was not a design constraint for the 10.4-m dish.

6.5 Final Sizing

The optical element size and geometry established earlier was evaluated in more detail as part of the final sizing. This analysis used detailed asymmetric models of the optical element to predict ring stress, deflection, and gross buckling. The impact of ring deflections on optical performance was evaluated by the National Renewable Energy Laboratory (NREL) using codes developed for membrane and dish analysis. As a result of these analyses, the ring height was increased from 152 mm to 203 mm (6 to 8 inches) to reduce the magnitude of optical distortions caused by the PCA support loads.

A finite-element model was used for these evaluations. The model is complex and does not allow cost-effective parametric evaluations, optimization, or numerous iterations. SKI relied on the initial sizing effort (using simpler models) for such work. This final evaluation was

intended primarily as a means to include PCA point loads and to evaluate the dish in terms of buckling and deflection while confirming the earlier stress predictions.

This section of the report describes the models used for the analysis, and the results of the final sizing effort.

6.5.1 Models and Approach

The finite-element model was built under SKI's direction by a subcontractor using ANSYS software (25). The model included the hub, ring, front and rear spokes. The hub and ring were modeled as beam elements with the spokes as spars. The front membrane was represented as a set of loads acting at the departure point on the ring.

The rear spokes were modeled as artificially soft, but straight elements in order to provide the same longitudinal stiffness as a deflected spoke. The artificial stiffness was determined through analysis using the previously described spoke model (SPOKESAG). The rear-spoke spar element was capable of compression or tension and was initiated with no tension. The spar element was used only to account for changes in the spoke tension. Initial load of the rear spoke was applied directly to the ring as an external force.

The loads induced by the PCA supports are also represented as external forces. These loads included the effects of PCA weight, PCA support structure weight, and wind loads. (See Appendix D for a description of a model (PCAREACT) developed to calculate these loads as function of PCA support leg spacing.)

Gravity loads were included for the PCA, the PCA support, and the ring. The impact of gravity loads from the hub, spokes, and membranes on ring stress, deflection, and buckling was assumed to be small and was not modeled. The gravity load from these members is small relative to other loads.

The load on the front membrane was assumed to have a pill box distribution. See Figures 6.7 and 6.8 for typical out-of-plane and in-plane load profiles. These out-of-plane loads were calculated to provide the net normal force and moments corresponding to the wind loads for the case of interest. The average in-plane load was defined to be the orthogonal component giving the resulting load vector the same departure angle as the membrane. Slight variations were made within quadrants to make the sum of the in-plane forces equal those defined by the wind loads. (Refer to Appendix D for a description of a model (RNGLD) that translates wind loads to membrane loads in this fashion.)

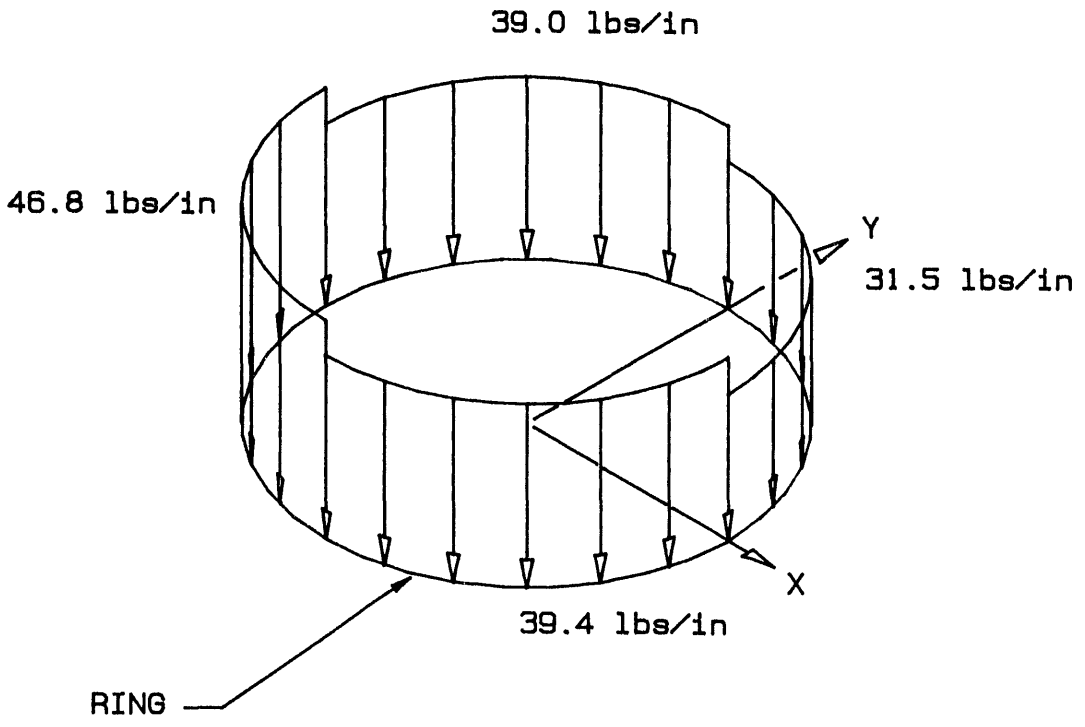

Figure 6.7 Typical Out-of-Plane Ring Loads as Modeled.

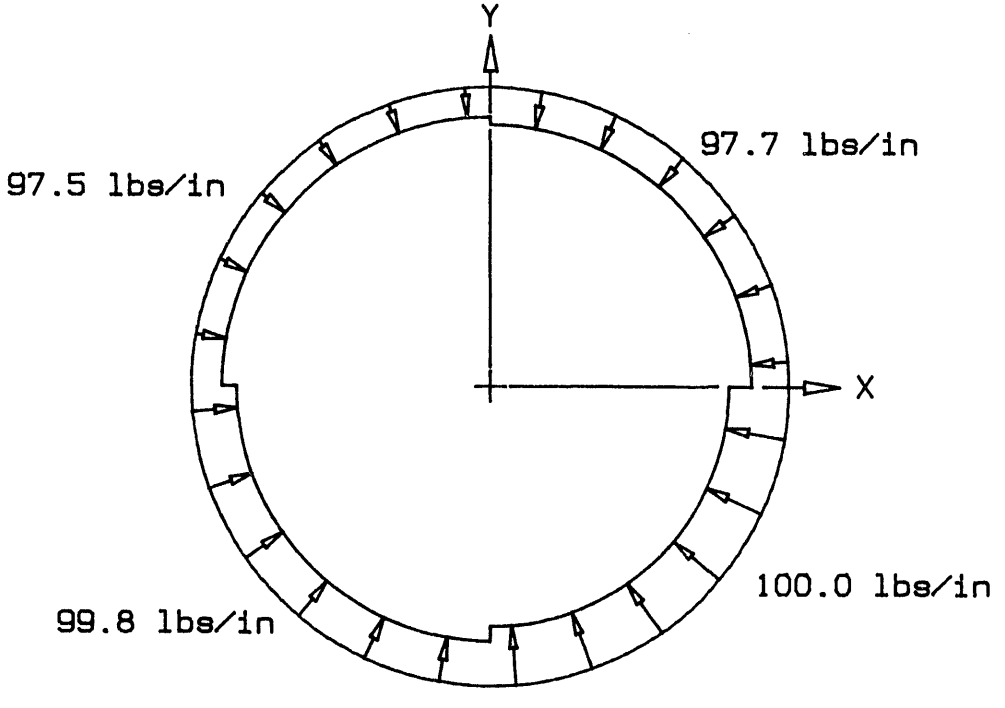

Figure 6.8 Typical In-Plane Ring Loads as Modeled.

Five cases were selected for evaluation. Three represented survival situations and two were selected for evaluation of operational deflections. Table 6.1 summarizes the cases.

Table 6.1 Summary of Evaluated Cases

Case #	Wind Speed km/hr (mph)	EL (degrees)	AZ (degrees)
S3	145 (90)	-25	45
S4	145 (90)	-25	90
S5	145 (90)	-25	180
D2	43 (27)	30	0
D7	0 (0)	0	na

Case S3 was selected because it has the highest azimuth moment and a normal force that is almost as high as that of a head-on wind. (Moments here are acting about axes in the plane of the ring.) Case S4 was selected because it has the highest side load. Case S5 was selected because it has the highest normal load from the rear. Case D2 represents an intermediate orientation that was selected for evaluation of deflections in high operational winds. It is a case that has a combination of nearly the worst normal and elevation moment load. Case D7 was selected to represent the worst gravity loads under zero wind conditions.

Two significant assumptions were made in applying the LTV wind load data. First, load data for a zero elevation were assumed to be representative of loads on a dish with a negative 25 degree elevation. No wind load data was available for negative elevation angles. This assumption gave slightly conservative normal loads. Second, the moment loads about the elevation axis as function of elevation angle were used to represent those about the azimuth angle as a function of azimuth angle. This is valid since the wind tunnel data were taken in a tunnel without a boundary layer.

The finite-element model predicts deflection and rotation of the ring centroid in a global (stationary) coordinate system. This data was converted to usable terms in a two step process. First, the displacement and rotation of the departure point were calculated based on the motion of the ring centroid and the relative location of the two. Second, the displacement of the departure point was calculated relative to the displacement of the receiver. This removes the tracking impact of rigid body ring rotation from the distortion effect. The ring tilts under gravity and wind loads. This tilt causes a tacking error that, if compensated for in the drive controller, will have no impact on dish performance. A code entitled XXSSC was developed for doing these conversions. (See Appendix D for more details on this code.)

The impact of ring departure point deflection on the optical shape and performance of the membrane was evaluated by NREL using two codes. First, DISH was used to determine the resulting membrane shape. Second, OPTDSH was used to determine the resulting impact on

dish performance. Refer to "Membrane Dish Analysis: A Summary of Structural and Optical Analysis Capabilities" for a complete description of these codes (26).

6.5.2 Analysis

Both an eigenvalue analysis and a non-linear iterative analysis were used to identify the buckling limit of the optical element. The eigenvalue analysis is non-iterative and reaches a single solution. The non-linear analysis is performed by sequentially increasing the loads on the model and determining if the analysis converges on a unique solution. If it does not converge, it is assumed that the structure has buckled. The non-linear analysis is believed to be more accurate because it takes into account load amplifications and varying stiffnesses as the geometry distorts. It also allows evaluation of the stresses at the design condition for confirmation with other models.

Case S3 was selected for analysis because SKI suspected that the highest stresses would occur in that case. Comparison of the finite element predicted stresses with those predicted by RINGSZ show good correlation. All stress components agreed within 10%, some were within 6%. The loads in the front spokes were within 3%.

This analysis was used to predict buckling of the entire optical element (often referred to as gross buckling). Local buckling of the ring wall or buckling of the hub are analyzed with other techniques and presented separately.

The eigenvalue analysis predicted buckling failure at 2.5 times the applied loads, but the mode of failure had no physical basis. The mode of failure was torsion or wind up of the ring about the hub. This mode was not seen in the non-linear analysis and was judged to be spurious. The next lowest buckling mode predicted by eigenvalue analysis was a two-lobe potato chip distortion of the ring with a load factor of 2.8. Non-linear analysis showed a similar two-lobe distortion with a load factor between 2.6 and 2.7 (solution converges at 2.6 and diverges at 2.7). The distorted shape is shown in Figure 6.9. The figure shows the undistorted ring centroid as a dashed line, and the distorted ring as a solid line. The X and Y axes are in the plane of the ring, and Z is coincident with the dish axis.

Several runs were done to evaluate means of increasing the stability of the optical element. Increasing the ring cross-section from 152 x 152 mm to 203 x 203 mm (6x6 to 8x8 inches) increased the load factor to 3.9 (39% increase) with a ring weight increase of 33%. Increasing the tube thickness only, from 0.25 to 0.37 inches, increased the load factor only to 3.1 (10% increase) with a ring weight increase of 50%. Adding a second set of stiff rear spokes (same stiffness as front spokes) increased the load factor to a value somewhere between 7 (150% increase) an 9 (221% increase). This technique could have the lowest weight penalty associated with it if stiffening is required.

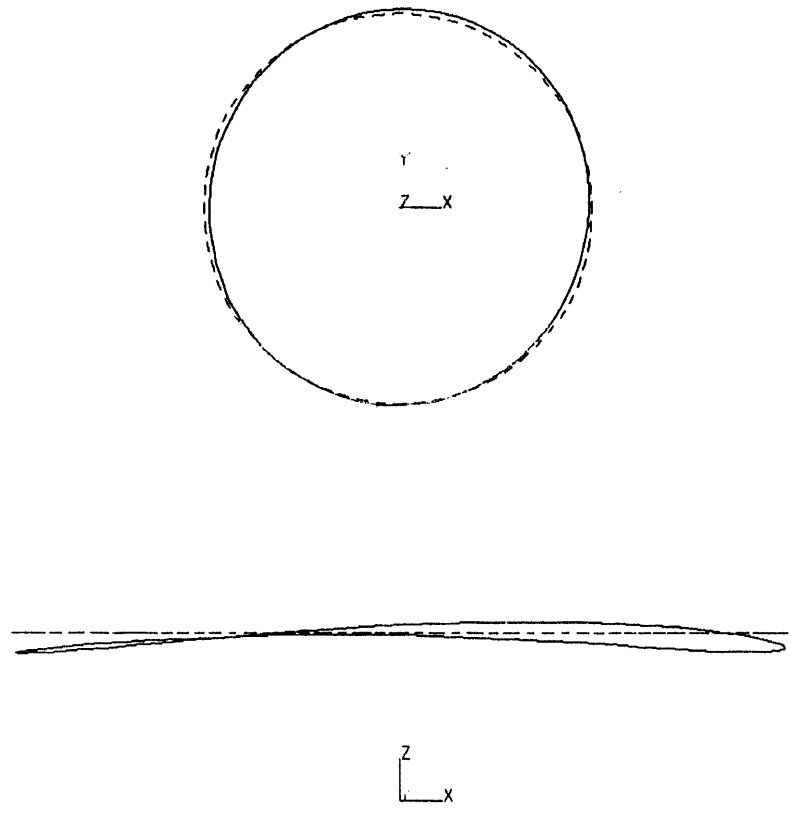

Figure 6.9 Buckled Shape of Ring

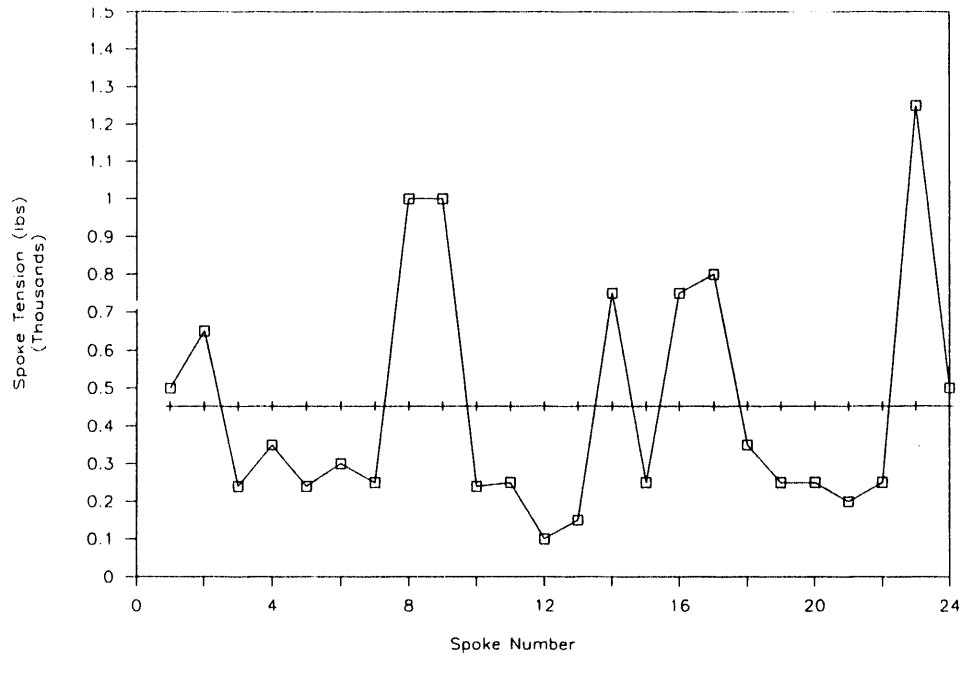

Figure 6.10 Measured Spoke Tension on 7-M Diameter Prototype

Acceptable load factors on buckling vary from application to application. Some airframe designers use values only slightly greater than one, particularly if the material does not yield and the structure can snap back to its original shape after the load is removed. Experienced investigators consider it appropriate to define the factor of safety in the same manner as would be used for factors of safety on stress. Since the dish structure is designed per AISC code, this would suggest a lower limit of about 1.6 for load factor.

Two runs were performed to test the sensitivity of the structure to imperfections. First, gravity and PCA support loads were removed. The load factor remained at 2.8 showing little sensitivity to imperfections. Second, the ring was distorted toward the buckled shape with an amplitude of 5.0 mm (0.2 inches) peak-to-peak. The front-spoke tensions were varied up to 50% of their initial values. This was also done with a two-lobe pattern to exaggerate buckling. The rear-spoke loads were varied by up to 17% in the two-lobe pattern. The 17% value represents the change in spoke load from a spoke that is installed with 50% difference in initial tension. The ring deflection and the spoke loads represent realistic values for manufacturing tolerances.

Figure 6.10 shows the variation in front-spoke tension on the 7-m prototype, as measured by torque values on the tightening nuts. Note that 50% variation is realistic. The conservative part of the analysis is that all variations combine in the worst way. The results, however, show no decrease in load factor thus demonstrating an inherent insensitivity to imperfections. The optical element was judged to be acceptable in terms of gross buckling.

Analysis of the stress in the ring and front spokes showed acceptable levels. Figure 6.11 shows stresses in the ring for case S4 as a function of circumferential location. A circumferential location of zero degrees refers to the right-hand side of the ring as viewed from the front while the dish is facing the horizon. Ninety degrees is the top

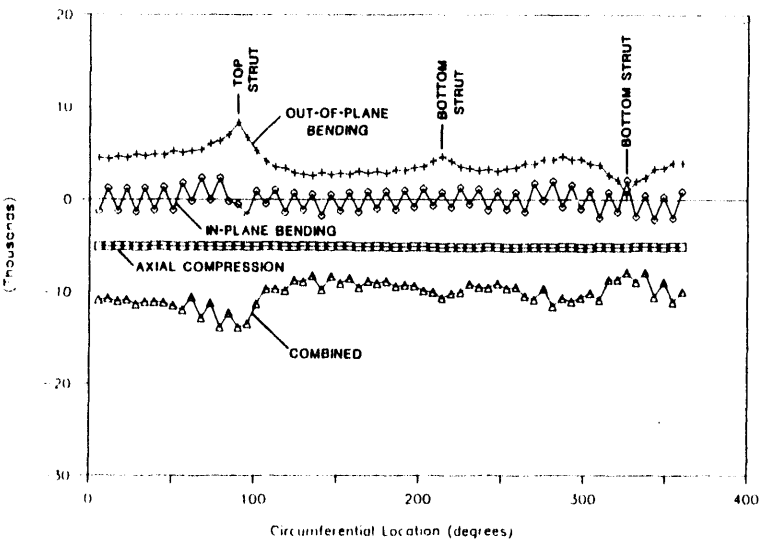

Figure 6.11 Ring Stresses as a Function of Location (Case S4).

most ring location. Axial ring compression is relatively constant as can be expected. Out-of-plane bending stresses cycle between positive and negative values due to the spoke loading. The out-of-plane bending, as used here, includes cross-sectional bending. This stress averages 27.2 MPa (3950 psi), but is significantly affected by the PCA struts. Note, that the lower two struts act in opposite directions because of the large side load acting on the PCA. This increases the compression in the leeward strut and decreases the compression in the windward strut. The lower line represents the worst combination of these stresses.

The highest loading occurs in case S3. A peak ring stress of 162 MPa (23,490 psi) is expected at the lower right strut. The maximum allowable stress is 186 MPa (27,000 psi). Figure 6.12 shows the stress pattern for this case. It can be noted that the PCA loads have a large impact on the peak stress. Peak stress for case S5 is only 117 MPa (17,000 psi). Peak stresses for the operational cases ranged from 73 MPa (10,600 psi) 81 MPa (11,700 psi).

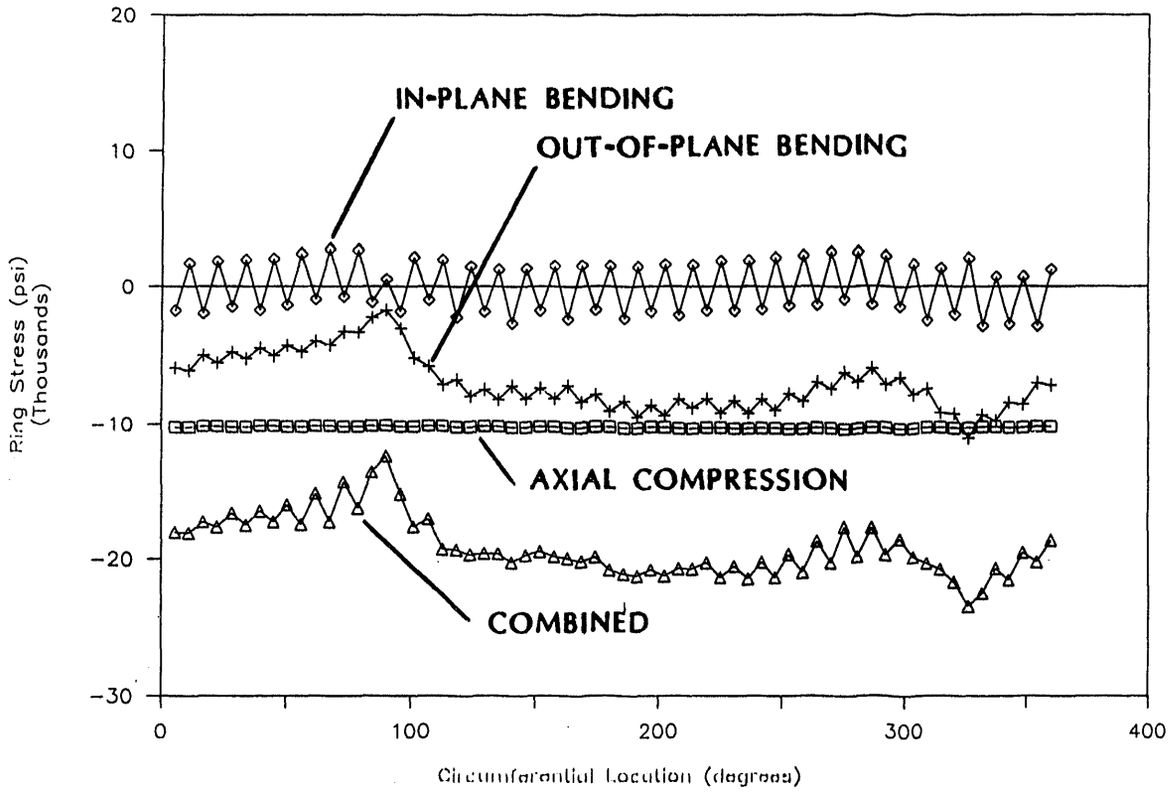

Figure 6.12 Ring Stresses as a Function of Location (Case S3).

Peak front-spoke load was 29,000 N (6,600 lbs) and occurred in case S3. The allowable limit (based on yield) is 95,900 N (21,600 lbs). Peak Load for all other cases was less than 18,000 N (4,100 lbs).

Figure 6.13 shows the influence that the PCA supports have on spoke loads. This is an illustrative case with an elevation angle of 30 degrees and front wind of 43 km/hr (27 mph)

(case D2). The lower two struts push equally on the ring (as evident by the two peaks on the right-hand side of the graph), and the top strut pulls on the ring, thereby, reducing spoke loads at that location.

Figure 6.13 shows the influence that the PCA supports have on spoke loads. This is an illustrative case with an elevation angle of 30 degrees and a front wind of 43 km/hr (27 mph) (case D2). The lower two struts push equally on the ring (as evident by the two peaks on the right-hand side of the reducing spoke loads at that location.

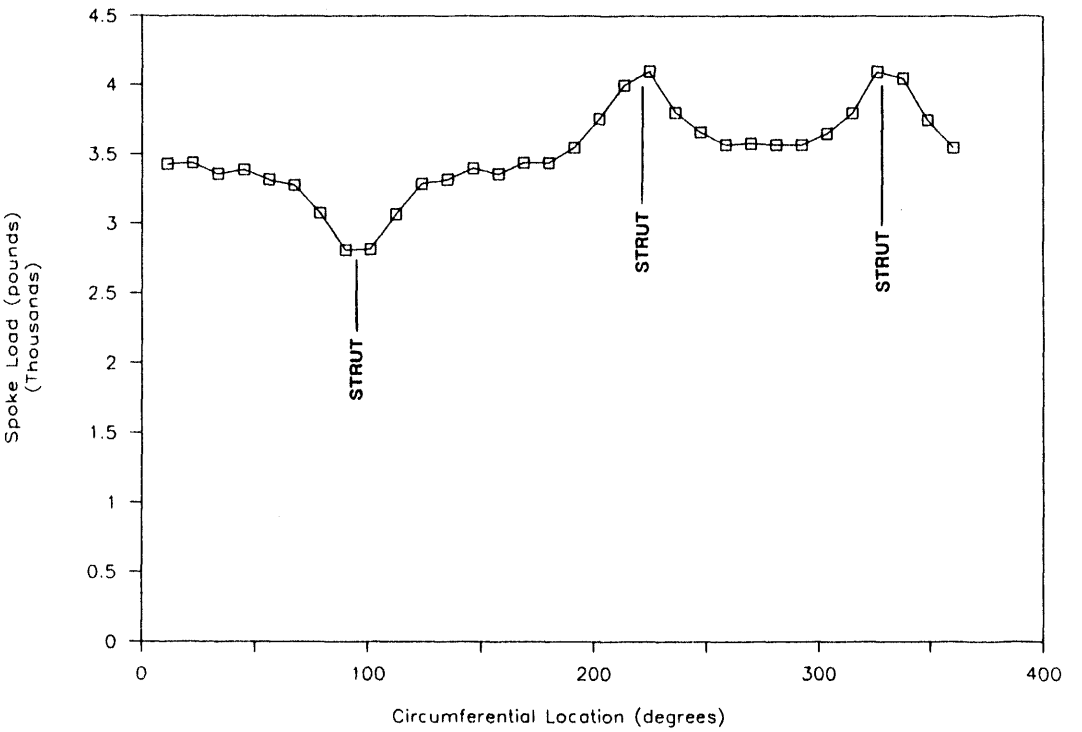

Figure 6.13 Influence of PCA Struts on Spoke Loads.

Movement of the optical element is divided into two categories. Those deflections that are a result of gross, overall tilt of the ring are considered tracking error because the PCA (being attached to the ring) will move with these motions. Deflections of the ring about this tilted position incudes slope error in the optical surface and is, therefore, categorized as such.

The weight of the optical element, PCA, and PCA support induce the most significant tracking errors in the optical element. The operational cases analyzed with FEA show that gravity will cause the optical element to tilt 2.8 mrad. If unchecked, this would be equivalent to 2.8 mrad of tracking error. However, gravity is predictable and can be compensated for in the tracking control algorithms.

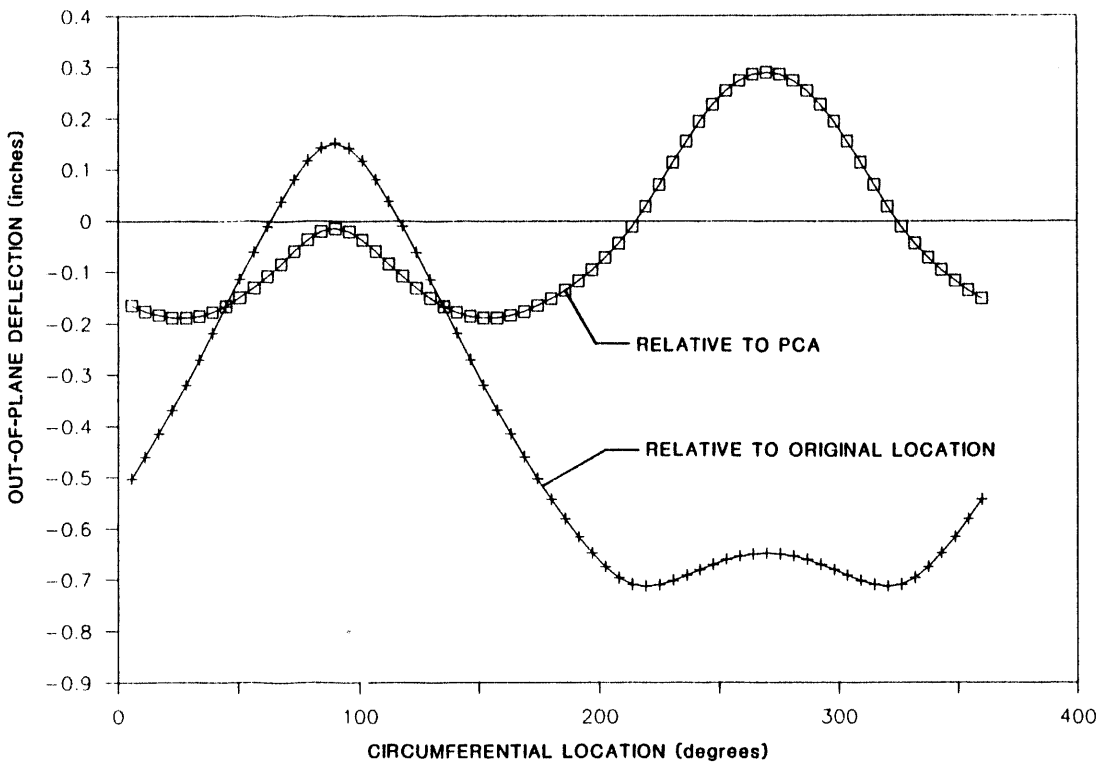

Figure 6.14 Ring Deflection as Function of Location (Case D7).

Analysis of FEA results show that tracking error caused by the wind will be small. Case S3 is a survival case having the maximum wind induced azimuth moment. The resulting azimuth rotation is 1.2 mrad. Peak wind induced operational moments (azimuth or elevation) are significantly less. The anticipated maximum operational tracking error is less than 0.4 mrad.

Analysis of distortions that cause slope error was more complicated. Figure 6.14 shows the out-of-plane deflection of the departure point of the membrane from the ring for case D7 (zero wind, facing the horizon). The lower line indicates the deflection relative to the original state (prior to application of gravity, stabilization pressure and initial spoke tension). The relatively low values, near 270 degrees, and the high values, near 90 degrees, indicate a significant tilt about the horizontal axis (2.7 mrad). The line is not a true sinusoid, which indicates that there are distortions in addition to tilt.

The top line shows the ring distortion only. It is a plot of the departure point deflection relative to the plane passing through the three PCA support attachment points. Thus, all tracking issues are removed. The top strut (at 90 degrees) pulls the ring toward the front of the dish. The lower two struts are in compression and tend to push the ring to the back. The peak-to-peak deflection of the departure point is approximately 13 mm (0.5 inches).

The impact this distortion has on dish performance was analyzed by Tim Wendelin at NREL using the DISH and OPTDSH codes (27). Effective radial and out-of-plane deflections were taken from Case D7. Circumferential rotations of the departure point were assumed to be zero. Details of the analysis are presented in Appendix E. There was good agreement between this model and CIRCE for the undeflected case. Concentrator efficiency was within 1.5 percentage points of one another. The drop in performance due to ring deflection was approximately 5.3 percentage points.

The FEA was initiated before the PCA supports were designed. Estimates for the PCA support weight were low and, therefore, the FEA was done with loads that were artificially about 25% low. To assess the impact of the additional load, a linear relation was assumed to exist between PCA support loads and reduction in thermal efficiency. This is a conservative assumption because some structural stiffness is created by the spokes. Using the linear assumption, the effective penalty from ring distortion is approximately 6.9 percentage points in optical efficiency.

Up to this point, the design of the optical element was assumed to be limited by stress. The resulting deflections and their impacts on performance was judged to be excessive. The design then shifted from being stress limited to being deflection limited. Several options were reviewed to reduce ring deflection.

One option was to add structural members that carry the PCA loads from the ring to the hub. These could be tension/compression struts or bending elements. Neither variation would allow the ring translation that occurs with changes in stabilization pressure. They have the potential to induce stress concentrations in the ring by carrying distributed loads through discreet points. Additionally, the tension/compression struts would compound the in-plane loads caused by the PCA supports. These options were not pursued to the analysis phase.

Possible reductions in the PCA support weight were considered. If 0.30 m (12-inch) diameter mechanical tubing replaced the 0.20 m (8-inch) pipe, the PCA support weight would decrease 29%. However, the larger diameter tube increases blocking at the same time that it decreases ring deflection. The net effect was a small decrease in performance.

Increases in spoke stiffness have only minor effects on ring deflection. An FEA case was run with front spokes having twice the nominal cross-sectional area. This had an insignificant effect on effective ring deflections.

Increases in ring stiffness showed promising results to reduce deflections. A 15% reduction in the ring deflection was shown by increasing the ring wall thickness from 6.3 mm (0.25 inches) to 9.5 mm (0.375 inches). This is 83% of what would be expected with a linear relation between ring stiffness (out-of-plane moment of inertia) and deflection. This difference is most probably due to the stiffness contribution of the spokes. The 83% value was used to evaluate other means of increasing ring stiffness without incurring high weight penalties. The most advanta-

geous approach was to use a 152 x 203 x 6-mm (6 x 8 x 0.25-inch) tube (baseline was a 152 x 152 x 6-mm or 6 x 6 x 0.25-inch). The out-of-plane moment of inertia is twice that of the baseline with only a 17% increase (169 kg or 371 lbs) in ring weight. This would most probably reduce the thermal efficiency drop from approximately 6.9, to 4.2 percentage points.

A FEA run has not been done for an optical element with the final PCA support weight and a 152 x 203 x 6-mm (6 x 8 x 0.25-inch) ring. Rather, a smaller (6 x 6 x 0.25-inch) ring was used. Confidence has been established for use of the larger ring by evaluating the changes between cases modeled with FEA. The larger ring has improved load carrying properties. The PCA loads still pass through its centroid. The distance from the ring centroid and the membrane loads change; but, as analyzed, have lower stresses using the RINGSZ model. The increased weight of the ring may increase the spoke loads, but their load was previously just 30% of yield and the weight only increased by 17%. The PCA support load increased approximately 25%. This, by itself, would increase ring stress, but is countered by a 100% increase of out-of-plane moment of inertia. The PCA loads primarily affect the out-of-plane stress. The worst case analyzed had an out-of-plane stress of approximately 55.1 MPa (8,000 psi). A 25% increase in this stress component would almost be completely offset by the 17% reduction in axial stress (70.7 MPa or 10,250 psi).

The larger (152 x 203 x 6-mm) tube was selected for the prototype. This ring will give acceptable performance without being so over designed that feedback to the design process is compromised.

6.6 Hub Design

The optical-element hub is a tubular member located at the center of the optical-element ring oriented with its axis concurrent with the dish axis. The hub serves two primary functions. It serves as a terminus for all the spokes. It also serves as the interface to the elevation drive.

All loads on the hub result from the reactions at the spoke attachments. The front spokes terminate at the extreme outer end of the hub. The rear spokes terminate just forward of the rear end of the hub. The tension loads in the spokes are transferred to the hub, which exists in a state of axial compression to balance these loads. The radial component of the spoke tension is balanced by local circumferential tension and by bending stresses in the hub. The entire weight of the optical-element ring and the PCA system plus the dynamic wind loads is carried as spoke tension to the hub. The spokes are always in tension.

The geometry of the hub, specifically its length and the position of its forward end relative to the ring plane, were scaled from the successful 7-m prototype geometry. Selection of the hub diameter resulted from a compromise among three considerations:

minimizing reflected flux blocking,
maximizing hub stiffness, and
simplifying of fabrication.

Some of the reflected flux may be blocked by the hub's outer end. The amount of flux blocked is a function of the hub length and diameter. The length was set by the 7-m prototype geometry so only the diameter remained a variable. A 0.61 m (24-inch) diameter was selected to prevent total flux shadowing and blocking from exceeding 10%. An area in the center of the reflective surface is shadowed by the PCA assembly and its support. This reduces the effect of the hub in blocking reflected flux. The additional reflective area blocked by the hub that is not shadowed by the PCA is only 0.1 sq.m. or 1 percent of the total reflective area blocked.

All wind-induced loads were increased by a factor of two to compensate for uncertainties in the wind load predictions (see Section 2).

6.6.1 Model Description

The hub was modeled as a cantilever beam. The net reaction from the front spokes was applied to the free end of the beam. The net reaction from the rear spokes was assumed to go directly to ground. The actual attachment point of the rear spokes to the hub was immediately adjacent to the hub rear attachment to the drive, making this a reasonable simplification of the model. Reactions for each moment and force were calculated separately (see Appendix D). Deflections were calculated with classical analytical techniques described by Roark (13). Slenderness rations, allowable stresses, and combined stress rations were calculated per AISC methods (14).

When a nominal hub design was selected, a finite-element model was built in Engineering Software Company's Integrated Structural Analysis package. This two-dimensional model permitted us to check the calculated stresses and deflections. No axial compression loads could be added to the bending loads for this model. To simulate the effect of the axial load on bending, a moment was applied to the free end of the beam. Figure 6.15 shows a schematic of the hub with imposed loads. It also tabulates hub section properties. This moment was equal to the compressive force from the spoke tension times the lateral deflection at the beam free end.

Inspection of the predicted stresses and stress ratios lead to local reinforcement of the hub to reduce stress at the rear end without adding material to the entire hub. This change was made to the models also.

6.6.2 Analysis results and selected member sizes

The selected hub is 0.61 m (24 inches) in diameter and 6.4 mm (1/4 inch) wall thickness. Without any additional reinforcing, this results in a 159 MPa (23,000 psi) peak survival

combined stress using the doubled wind loads. This exceeds the AISC allowable stress limit. The dominant bending load in the hub results from gravity loads, so reinforcing is only required in one plane. Plane rectangular stiffener blades were added to limit the stress at the root of the hub. Peak stress was reduced, but a large step in the hub stress occurs at the end of the reinforcing blades. Figure 6.16 shows peak hub stress along its length. The hub stress with revised, tapered stiffeners shows that stress risers have been eliminated. Peak stress is reduced to 103 MPa (15,000 psi).

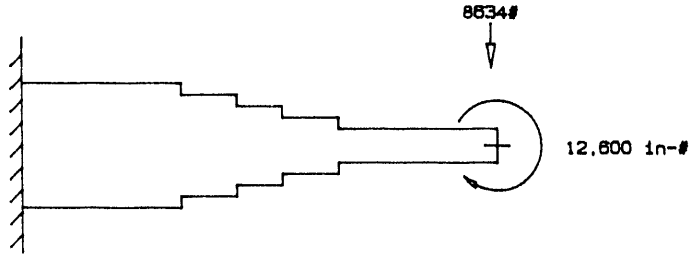

POSITION	MOMENT OF INERTIA	SECTION MODULUS
0	2097 in^4	200 in^2
27	2061	196
36	2013	190
48	1911	178
52	1875	172
60	1735	154
72	1613	142
178	1315	110

Figure 6.15 HUB Model with 43 km/hr (27 mph) Wind Loads Shown.

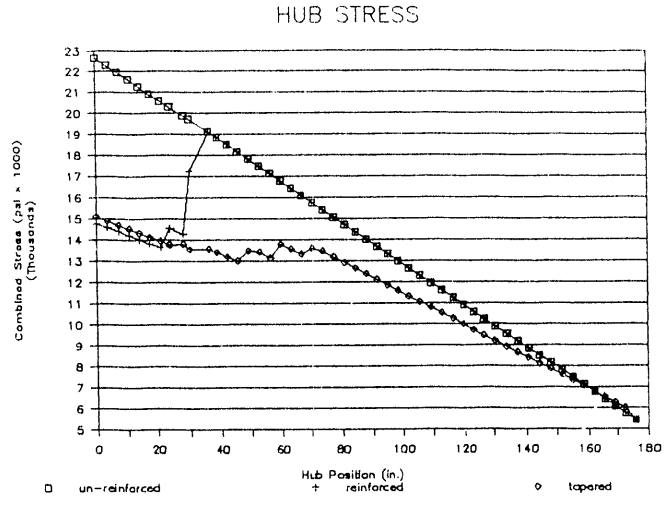

Figure 6.16 HUB Stress

Hub deflection with no wind is 6.8 mm (0.267 inches). With 43 km/hr (27 mph) wind at its worst orientation, deflection is 7.0 mm (0.277 inches). This is a negligible angular change. At survival conditions, this deflection is approximately 8.6 mm (0.34 inches).

The reinforcing blades were designed to be integral with the elevation pivot pin mounting. A pin in double shear was selected as a simple and reliable pivot geometry. This required two blades per side for the pin mounting and led to two blades per side being used for the reinforcing blades as well. The resulting stiffener design utilizes more material than is strictly necessary. The fabrication, however, is simplified by sing uniform thickness for each entire blade.

6.7 Natural Frequency Issues

Structures with low natural frequencies that have poor inherent damping could be excited at resonance by the wind. Such excitation produces internal loads that could be magnitudes higher than exist under normal operation and could result in structural failure. SKI has analyzed the natural frequency of the dish to ensure that it is sufficiently above the dominant exciting frequency of the wind. Most of this work was done for an 11.7-m diameter dish prior to the reduced tier in the dish size. Critical vibration modes were reevaluated for the current 10.4-m dish and were found to be acceptable.

Lumped parameter modeling was used to evaluate five different vibrational modes for the 11.7-m dish. The mode with the lowest natural frequency was a torsional vibration about the vertical axis with the dish facing the zenith. The pedestal, azimuth drive, hub, and front spokes were modeled as springs acting in series against the mass moment of inertia of the ring. The mass of the optical element minus the hub was assumed to be distributed along the ring centroid. The stiffness of the spokes was calculated based on their geometric resistance to elongation or compression when the ring rotates. The spring constants for the hub and pedestal were determined from classical mechanics. The spring constant of the drive was estimated from manufacturer's data. The single spring/mass model had a natural frequency of 1.4 Hz. The parameters were updated for the 10.4-m dish, and the analysis was repeated. The natural frequency was calculated to be 1.6 Hz.

A computer program (TORSFREQ) was written for this analysis and is described in Appendix D.

Four other modes of vibration were analyzed for the 11.7-m dish, but all produced higher natural frequencies than the mode described above. With the dish facing the horizon, the natural frequency in torsion about the axis of the pedestal was 1.7 Hz. The natural frequency in torsion about the elevation axis (facing the horizon) was 2.2 Hz. The natural frequency in translation in and out of the ring plane (facing horizon) was 3.5 Hz. The natural frequency in translation in the plane of the ring (facing the zenith) was 4.0 Hz. This analysis includes the effects of bend and twist of the pedestal, drive, hub, and ring relative to the hub. The spring

constant for ring translation or tilt relative to the hub was based on finite element analysis of the optical element under gravity loads.

The dominant excitation frequency of the wind is approximately one hertz. Other similar structures have been successfully demonstrated with natural frequencies in the range of 1.4 Hz. The 1.6 Hz value for the 10.4-m dish was judged to be acceptable.

The 10.4-m dish was not evaluated for the other four modes of vibration. It was assumed that the other modes would produce higher natural frequencies as occurred with the 11.7-m dish. In support of this assumption, the differences between the 11.7-m dish and 10.4-m dish were reviewed. The mass moment of inertia of the optical element was the same for both dishes. The bending stiffness of the hub was twice that of the 11.7-m dish, and the torsional stiffness was slightly greater. The bending and torsional stiffness of the pedestal decreased by only 20 percent. The translational and tilt stiffness of the ring relative to the hub was not evaluated.

6.8 Selection of Metal Membrane Thickness

The thickness of the metal membrane affects the final shape of the dish and is, therefore, an important variable in the forming process. Because the forming process is dependent on dish diameter, the thickness of the membrane must also change with diameter. A method of selecting the membrane thickness was formalized based on experience with 3.7-m and 7-m membrane forming.

We used 0.05 mm (2-mil) thick membranes at the 3.7 m scale and achieved accuracies of 2.3 mrad (2). We altered the forming variables slightly for our 7-m membranes and achieved accuracies of 2.5 mrad (3). The membrane thickness at 7-m was 0.18 mm (7 mil).

Free-body analysis of the membrane forming process defines the required membrane thickness based on the dish diameter, membrane strength, and applied. The applied forming load is a combination of air and water pressure. A software routine entitled MEMBTHK (Appendix D) was written to define thickness based on these variables. Applying the same forming variables as was used for the 3.7-m membranes predicts a 0.4 mm (16 mil) thickness for the 10.4-m dish. The same analysis using 7-m data predicts 0.2 mm (8 mil) membrane thickness. This bounds our results for this sized dish. Accurate 10.4-m membranes could likely be formed with membrane thickness between 0.2 and 0.4 mm (8 and 16 mil).

We looked to some subleties of the previous membrane forming for final thickness selection. Figure 6.17 shows the contour accuracy of the three 7-m membranes that have been formed (21). The presented data was taken along a single radial line. Each membrane is shown at an intermediate step in the forming process. Each membrane had the same thickness, but had slight variations in the forming variables. The point of interest is the area about two-thirds the dish radius from the center. This area seemed to be unaffected by the forming process. Its slope error was constant at about -4 mrad.

Figure 6.18 shows the accuracy of a 3.7-m diameter membrane (2). The data represents measurements taken over the entire dish surface. It has a broader band than the previous data. Notice that there is no point on this graph at two-thirds the radius where the slope error is not very close to zero.

Comparison of the data from the previous two graphs implies that the forming method should follow that of the 3.7-m membrane and, therefore, the membrane thickness should be 0.4 mm (16 mil). We tempered these results a bit because the forming method used at 3.7-m allowed no room for slight variations in the forming process that may be required with initial prototypes. We, therefore, selected 0.3 mm (12-mils) as the appropriate membrane thickness. This allows us to improve the accuracy of the membrane and provides flexibility of the process.

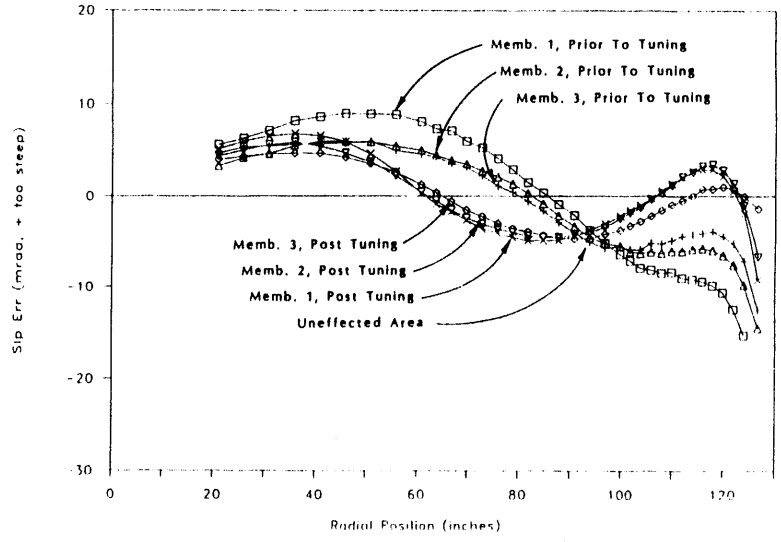

Figure 6.17 7-M Membrane Slope Error Showing Unaffected Area.

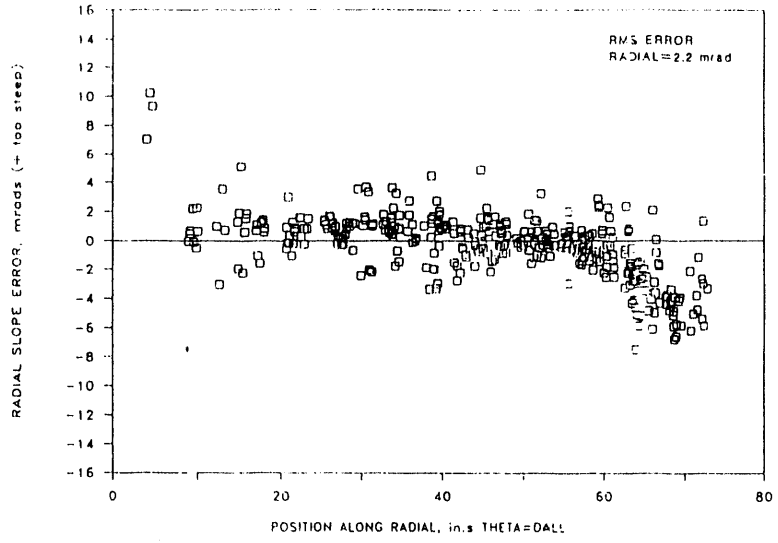

6.18 3.7-M Membrane Slope Error

7.0 Optical Element Detail Design

This section discusses specific details of the optical element. Joining methods, fabrication details, and geometry are described. The primary components discussed are the ring, membranes, spokes, and hub. The general approach to this detailed design is very similar to that used on the 7-m prototype. Several details have been improved based on experience gained with the prototype. To improve cost-effectiveness, many fasteners have been eliminated. This increases the reliance upon welded joints. Welding is often more cost-effective for production operations because fewer parts and fewer process steps are required. Also, less field and shop assembly labor is required for welding. Quality assurance procedures are critical for such a design, but these systems are reliably used throughout industry today for many products. Most welding will be done using GMAW processes for high quality welds with minimum weld time and minimum weld cleaning required before final surface finishing.

7.1 Ring and Membrane Attachments

The ring is a rectangular steel tube rolled to an outside radius of 5.36 m (211 inches). The cross-section is 152 mm (6 inches) wide, 203 mm (8 inches) high, and has a 1/4 inch wall thickness. The ring is fabricated from three sections and field welded to form a complete ring. The spoke, PCA support, and membrane attachment hardware are welded onto the ring segments at the factory. The joints between the ring segments are positioned to be clear of any other attachments. Figure 7.1 is a frontal view of the ring showing the location of spokes, splices, and PCA supports. The use of three segments for the ring was chosen to minimize field welding and permit component shipment by truck.

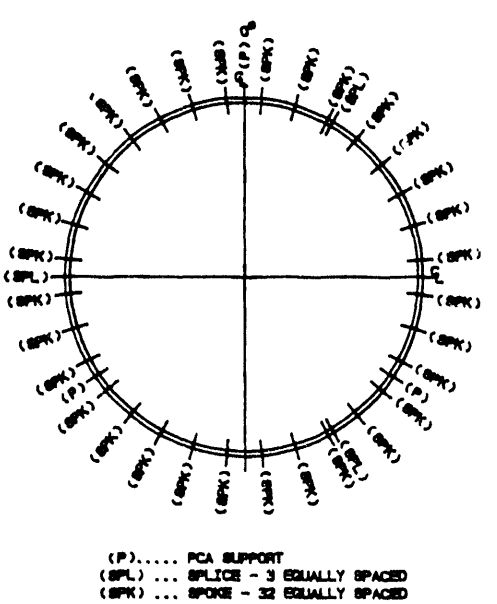

Figure 7.1 Layout of Optical-Element Ring Attachments and Splices.

7.1.1 Rear-Membrane Standoff Rail

The rear standoff rail around the outer circumference of the ring serves to space the rear membrane away from the ring (Figure 7.2). The rear membrane must not contact the front-metal membrane under any condition. The rear membrane drapes over the rear spokes and the standoff rail. The standoff rail is fitted closely to the rear spoke attachment brackets so that the membrane material is always well supported. Although the rear-membrane material is extremely tough, concentrated loads on the membrane material should be avoided to prevent chafing or local damage.

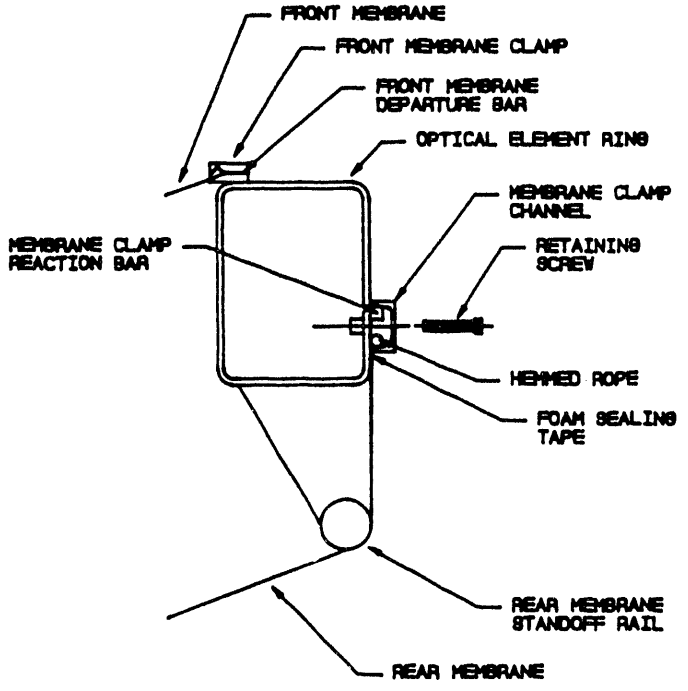

Figure 7.2 Details of Optical-Element Ring Cross-Section.

The standoff rail consists of light-wall steel tube segments, bent to match the radius of the ring. The rail mounting brackets are cut and formed from steel plate. The brackets are welded to the rolled-ring segments and the rail tubing is fitted and welded to the brackets.

7.1.2 Rear-Membrane Attachment Hardware

The rear membrane has a hem all the way around its perimeter with a 13 mm (1/2 inch) diameter rope sewn into it. This provides a means to grip the membrane against the ring. A channel-rolled leg fits against the outer radius of the ring and captures the membrane hem as shown in Figure 7.2. The other leg of the channel rests against a steel bar welded to the outside of the ring. This provides an anchor for the channel to resist the tension in the membrane. The retaining bolts holding the channel serve to keep it in contact with the membrane and ring; membrane tension is not reacted through the bolts. The radial pressure of the channel segments against the membrane also serve to seal the membrane to the ring. To assist this

sealing, a strip of closed-cell foam is placed between the membrane and the ring directly under the channel leg.

The ring material is too thin to be tapped to receive the membrane clamp retaining screws. Self-clinching rivet nuts are used in plain holes to allow machine screws to be used for this purpose. These fasteners allow use of screws and speed production by eliminating tapping.

7.1.3 Front-Membrane Attachment Hardware

The front-membrane mounting hardware is shown in cross-section in Figure 7.3. All the hardware is fabricated from common carbon steels. The front membrane is welded to the departure bar during final assembly in the field. The departure bar is machined to have an angle on its inside edge matching the angle of the parabolic membrane at its periphery. The membrane is trimmed in the factory immediately after forming such that its outer radius matches the radius at the outer edge of the departure bar beveled edge. This allows the membrane to be welded to the departure bar along the inclined surface of the departure bar. Electric resistance welding will be used.

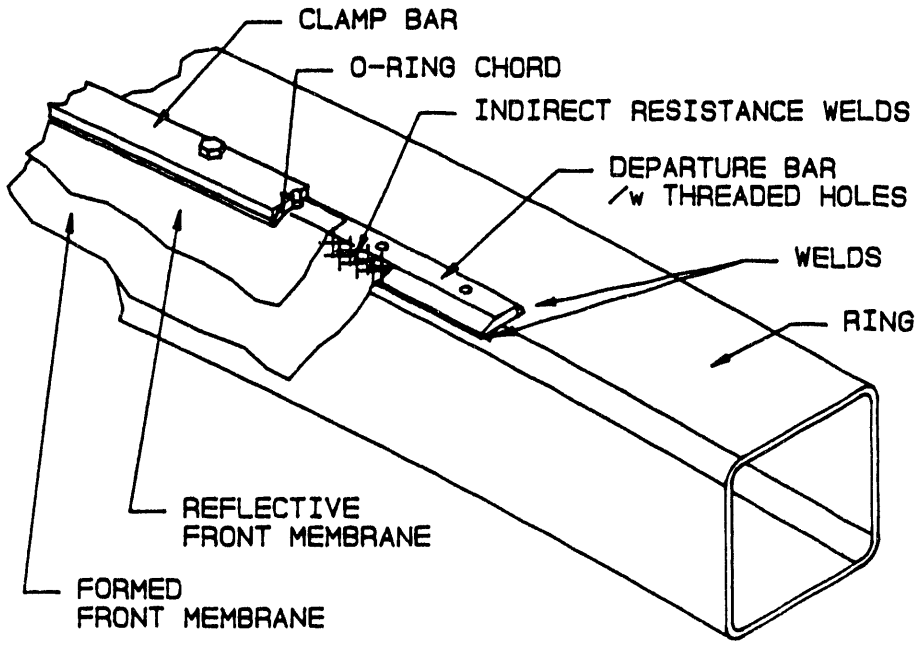

Figure 7.3 Front Membrane's Periphery Attachment Details.

7.1.4 Departure Bar

For the current design, the departure bar is welded to the ring segments during factory component fabrication. At this time, there is no bevel on the bar. The bevel is machined onto the bar after the ring has been assembled in the field. A portable-milling head supported by

the ring will be used for this. The machine will mill the required angle on the departure bar while also assuring concentricity and planarity of the departure bar.

Machining the bar in the field during final assembly may seem to be a significant complication to the assembly operation. However, this approach actually avoids many more potential problems than it creates. The departure bar must closely match the ring on which the membrane is formed for the installed membrane shape to be uncompromised. To assure this, either the field assembly operation must be very accurate or the departure bar must be adjustable. The prototype dish was completely pre-assembled in a shop. The departure bar was clamped in place, and the ring was match drilled to assure its radial placement. Planarity was adjusted by shim stacks placed on 230 mm (nine-inch) centers. The membrane was then formed using the ring as part of the tooling. The ring was then cut in two for shipping, fixtured very carefully in the field, and re-welded. The shims were readjusted to maintain planarity, but the radial position could not be adjusted. This approach is not practical for a manufacturing operation. The tooling must be permanent and the assembly operation must occur only once and in the field. The manufacturing procedures must assure that the departure bar matches the tooling within tolerance after final assembly.

Tooling is required to control the radius and planarity of the bar to the ring segments during attachment in the factory. The field assembly tooling must accurately control the ring radius and planarity during its final assembly and welding. The welding of large steel components such as this without inducing distortions from weld stresses is very problematic. Additionally, the departure bar is subject to damage from handling and clamping during shipping so it must be inspected and dressed in the field before assembly.

To install the departure bar in the field requires clamping and match drilling it for radial position and shimming it for planarity. This is very time consuming. For both of these approaches, an accurate rotating fixture is required in the field to measure the departure bar position.

The 10.4-m design employs a field-milling operation using a rotating fixture as a reference. The design eliminates the use of shims and also eliminates the match drilling. A custom milling, self-propelled machine (see Figure 7.4) will be supported by the ring. The machining forces will carried directly to the ring as the machine travels around the ring itself. It will have a sensor head that detects the relative position of the end of the rotating arm. The cutting head will be driven radially or vertically to maintain the departure bar bevel at the correct vertical and radial positions relative to the end of the rotating fixture arm.

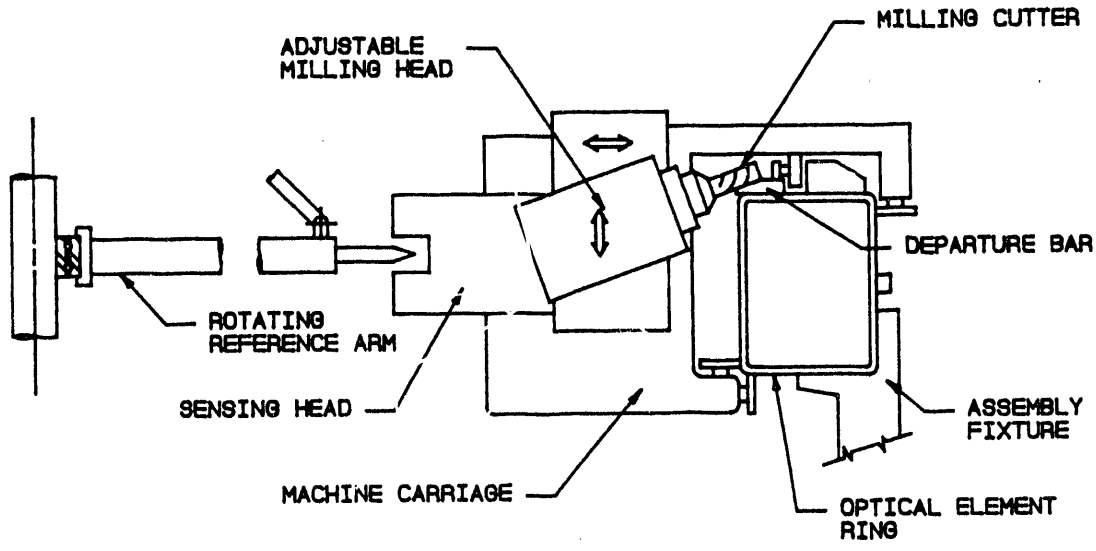

Figure 7.4 Conceptual Layout for Field Milling of Departure Bar.

7.1.5 Clamp Bar

The front-membrane clamp bar (see Figure 7.3) is made up of multiple segments, rolled to the correct radius. These segments are predrilled for the clamping screws. The clamping screws extend through the clamp bar and thread into holes in the departure bar. The clamp-bar segments also have machined grooves under their inside edge. This groove captures a length of neoprene O-ring cord. (The cord is sized so that it has an interference fit in the groove so that clamping pressure causes the cord to tightly clamp the front membranes to the departure bar.) The elastomeric cord creates an even pressure on the polymer-membrane material and avoids line contact with attendant high pressures that could cut the film.

7.2 Membranes

7.2.1 Front-Metal Membrane

The front membrane is Type-304, one-quarter hard stainless steel. It is fabricated from 0.3 mm (0.012") thick by 0.91 m (36") wide coil stock. The coil stock must be stretcher leveled by the rolling mill so the material lays as flat as possible on the layout table during fabrication. Some membrane problems for several stretched-membrane mirrors have been traced to non-flat stock material. Obtaining stretcher-leveled material meeting an exact specification is difficult. The few rolling mills capable of doing this recognize that leveling coil stock is increasingly difficult with increasing coil width and decreasing thickness. These firms either

charge a premium for leveled material or decline to quote to a rigid specification. This design requires the widest material possible to reduce the total number of seams.

The membrane is fabricated by resistance welding strips of coil stock edge to edge to form a sheet approximately the width of the dish. Each edge is overlapped approximately 13 mm (1/2"). The sheet is trimmed to a circular shape and fixtured to a tooling ring for forming. The perimeter of the tooling ring has the same diameter and angle as the departure bar of the dish. After forming, the membrane is trimmed to the outside diameter of the inclined angle on the departure bar and rolled onto a custom-contoured mandrel for storage and shipping. This operation is more fully described in Reference 2.

When the front membrane is attached to the optical-element ring, its outer edge is positioned and welded to the departure bar. Welding is accomplished quickly with a hand-held rolling resistance spot welder. The outer edge of the metal membrane is to be sealed to the departure bar using Tedlar weather resistant pressure sensitive tape. This prevents moisture from causing corrosion of the departure bar under the metal membrane. When the reflective membrane is in place, the clamp bar is installed as described previously. The pressure from the O-ring cord clamps both the metal membrane and the polymer membranes in place. The metal-membrane-to-departure-bar welds serve only as a backup fastener system.

The center of the formed membrane has a hole to accommodate the central hub. After membrane installation, the center of the membrane is tethered to the central hub. If stabilization vacuum is ever lost, this tether protects the formed metal membrane by preventing it from being drawn completely convex by wind or gravity forces.

The hole in the membrane is sized to allow free draining of rain into the hub itself. It also allows service access to the reflective-membrane-bellows seal. The edge of the central hole has front and rear reinforcing doubler rings to reduce local stresses from the membrane-seal attachment. The doubler rings have staggered outside diameters to better carry the loads through the steps in membrane thickness. The doubler rings are the same thickness as the body of the membrane.

The tether is achieved using a heavy plasticized polyester cloth collar (see Figure 7.5). The collar clamps to a ring on the hub several inches to the rear of the metal-membrane center opening. The forward end of the collar clamps to a second ring on the metal-membrane inside diameter. There is sufficient slack in the collar to accommodate shifts in the membrane's position relative to the hub, which occur during normal operation.

The spacer ring, which supports the fixed tether mounting ring, has multiple holes to allow vacuum to be drawn in the space between the reflective and the metal membranes. These holes serve as flow restricters to ensure that during initial vacuum stabilization of the dish, the metal membrane is pulled to its stabilized position and shape before the reflective membrane. This allows the reflective membrane to be gradually pulled into place without trapping air.

This restriction also assures that if the reflective membrane fails, the metal membrane will remain stabilized. The leakage rate through the restricter holes is less than the volume capacity of the vacuum blowers at the minimum stabilization vacuum.

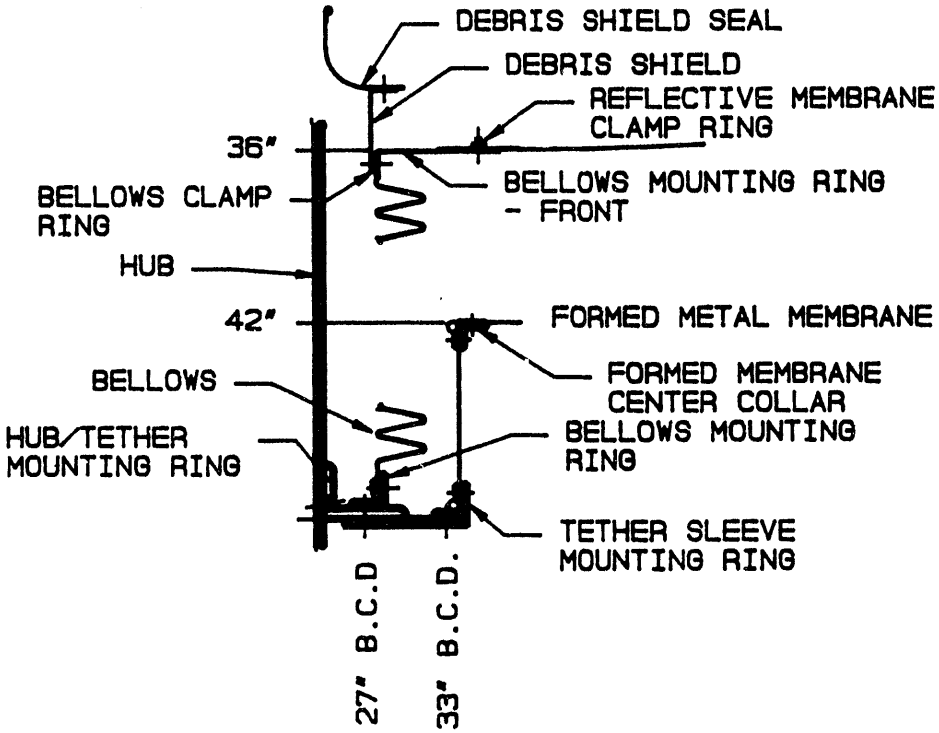

FIGURE 7.5 CENTRAL FRONT-MEMBRANE SEAL AND TETHER DETAILS.

A tube for a temporary air supply connects to the space between the bellows and the tether ring. This allows pressurized air to be blown between the membranes to promote separation when needed during replacement or servicing. If the stabilization vacuum is to be turned off during any dish servicing operation, the reflective polymer membrane will attempt to return to its original shallow cone shape. If it is stuck to the metal membrane, it will tend to pull the metal membrane upwards and inducing wrinkles and creases. Air can be blown between the membranes to gently separate them while holding the metal membrane in its correct operating shape.

7.2.2 Front-Reflective Membrane

Completely satisfactory materials for the front-reflective membrane are not commercially available today. There are several efforts to develop and/or demonstrate potential materials. Existing commercial reflective films have been successfully used for heliostats and high f/d dishes, although film life is still a major issue. Low f/d dishes require a ductile film that will support capable high strength seams. This is additional to the requirements shared with other solar reflectors, high reflectivity, and resistance to weathering. NREL is funding film development contracts that include consideration of metallized Teflon film. These offer the possibility of high reflectivity combined with ductility and weathering properties required.

The current stretched-membrane dish design has a reflective polymer film stretched over the formed metal membrane. The film is not adhered to the metal to augment its replacement. The membrane is actually two layers, the front is a transparent protective film and the second a highly reflective film. The reflective membrane is fabricated in a conic shape. The inside surface of the cone is reflective, and the depth is 85% of the depth of the formed metal membrane. When the dish's stabilization vacuum is activated, the vacuum stretches the reflective membrane and draws it down against the contour of the formed metal membrane.

High silvered films use acrylic or polyester as the substrate. Acrylic is not ductile enough to reliably stretch the required amount for a 0.6 f/d dish. Its notch-sensitive nature also makes it unsuitable for the reflective film. Seaming acrylic poses problems also. Solvent welding is possible, but if not well controlled, it can weaken the film or degrade the reflectivity near the seam.

Polyester is more ductile, but it suffers from degradation by exposure to ultraviolet light. This effect is minimized by metallizing the front side of the film and applying a protective transparent overcoat. The overcoat serves two purposes. It isolates the silver from the atmosphere to eliminate tarnishing. It contains ultraviolet inhibitors to prevent the transmission of ultraviolet light. This is important because the silver is effectively transparent to ultraviolet polyester does allow high strength seams using heat activated adhesives.

Tests of a two-layer reflective membranes such as described here are described in Appendix A. The reflective film being used is a commercial product available from 3M Company called SilverLux. It is normally used on reflectors for indoor lighting fixtures. An important question, which the testing should answer, is how well the protective overcoat performs after being stretched and exposed to extensive sunlight. The cover film is DuPont's Teflon FEP Type-C film. An important issue being addressed for this material is how its transparency is affected by extended exposure to weather and cleaning. Ideally, a single-layer film will become available.

Until such time that a more suitable film is available, the two-layer approach will be adequate. See Section 11 for a description of 7-m tests of this approach. The reflective polyester film may be 0.01 to 0.05 mm (0.5 to 2 mils) thick without adversely affecting the stabilization vacuum required. The strongest seams tested, to date, use a heat activated polyester-based adhesive reinforced with transverse fiber tape (see Figure 7.6). The film edges are butted together, and the adhesive is applied to the back of the film. The fibers in the tape bridge across the seam and sandwich the adhesive and the film. When the adhesive is activated under pressure and heat, it flows around the fibers and bonds to the film surface. A strip of Tedlar pressure-sensitive tape is applied to the front of the seam to eliminate pealing forces at the front interface and to seal the butt joint.

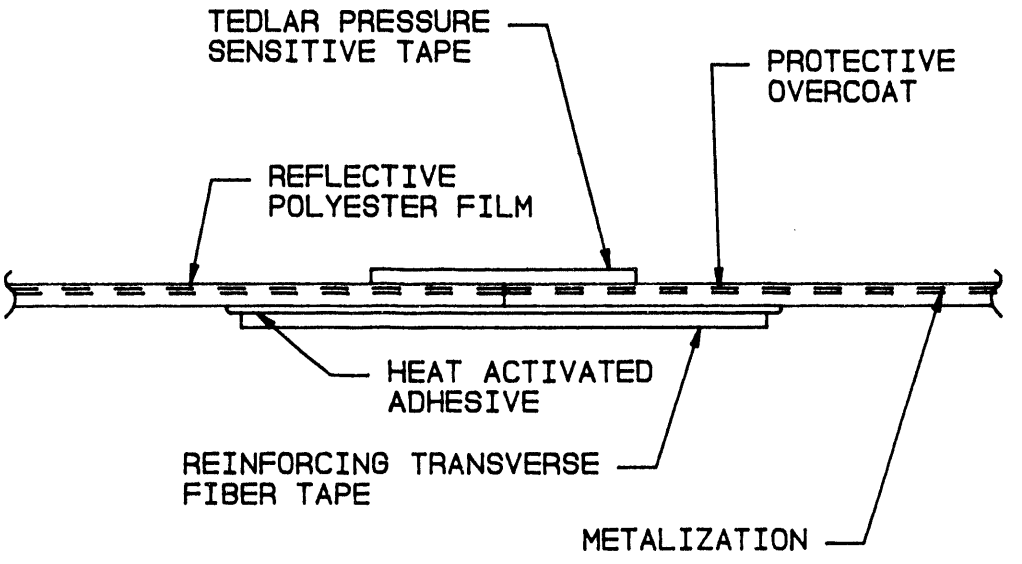

Figure 7.6 Cross-Section of Reflective- Membrane Material Seam.

The selected reflective film is 3M SilverLux. Solar reflectivity is 94%. It is constructed of 2 mil polyester film with a front metallized layer of silver covered with an acrylic solution coat. The acrylic includes ultraviolet absorbing agents.

The transparent protective film is 0.05 mm (2 mil) fluorocarbon film. Seaming is readily accomplished using impulse heat sealing. The film is ductile, so seam tension is not great (approximately 874 n/m or 5 lbs/inch) even starting with a flat membrane. Peak local strain in an initially flat membrane is 8% while maximum possible material elongation is 300%. Solar transmissivity is 96%.

Measurement of the solar-weighted hemispherical reflectance of the two layer membrane was 93% (28).

7.2.3 Rear Membrane

The rear membrane is draped over the outside (rear side) of the optical-element rear spokes. Its purpose is to enclose the volume between the formed front membrane and the rear spokes to create a vacuum plenum. When stabilization vacuum is applied, the rear-membrane material is drawn against the rear spokes. The rear membrane is constructed of a PVC coated polyester cloth. The heavy (1.2 kg/m^2 or 32 oz/sq.yd.) cloth is strong, abrasion and tear resistant, and easily fabricated. Seams in the membrane are overlapped, solvent glued, and sewn with multiple passes. Correctly executed seams are as strong as the fabric itself. The material is manufactured for use in air supported buildings and cargo tarpaulins.

The rear membrane is fabricated in the shape of a cone. The circumference is finished with a rope sewn into a continuous hem. This rope is captured against the outside of the optical-element ring by segments of channel as described in Section 7.1. The center of the membrane has a hole to accommodate the optical-element hub. This hole also has a rope sewn into a hem around its circumference.

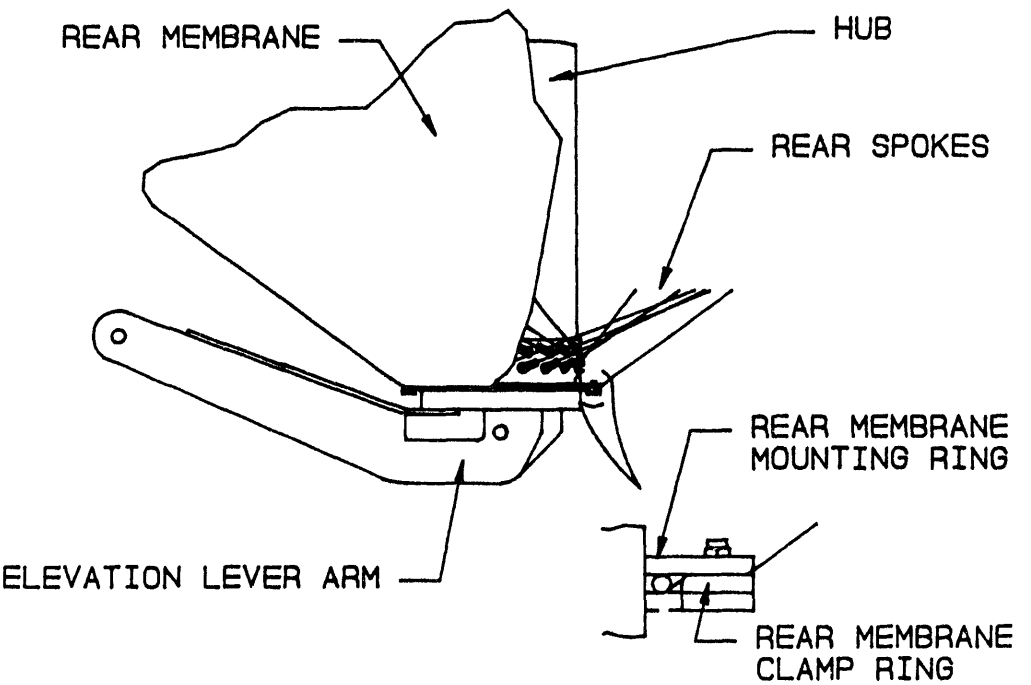

Figure 7.7 Rear-Membrane Center Attachment Details.

A flange is welded to the hub behind the rear-spoke attachment. The center of the rear membrane is supported by this flange as shown in Figure 7.7. A separate split-clamping flange captures the rear membrane against the sewn in flange. The split flange is through bolted to the mounting flange.

7.3 Membrane Seals

The front membrane must be sealed to the optical element to retain the stabilization vacuum. Seals exist at the membrane periphery and at the central hub. The seals must minimize leakage into the vacuum plenum because it will proportionately increase parasitic power usage by the vacuum system. The seals are designed to permit field replacement of the reflective membranes.

The periphery seal is accomplished by squeezing the membrane against the metal membrane where it is backed by the departure bar (see Figures 7.2 & 7.3). The squeezing force is applied by the O-ring cord as described in Section 7.1.

The central-seal assembly includes separate seals for the reflective and metal membrane (see Figure 7.5). The seal at the hub is flexible to permit the reflective membrane to move from its initial position at installation with no vacuum applied to the operating position against the formed-metal membrane. The seal assembly at the hub includes a secondary seal for the metal membrane only. There are three purposes for this seal:

1. If the reflective membrane should be damaged while it is being replaced, the metal membrane can still be stabilized.

2. When the reflective membrane is to be replaced, the space between it and the metal membrane can be pressurized to separate the reflective membrane from the metal one for easier removal.

3. The metal-membrane seal serves the additional function of providing a tether for the metal membrane. If all vacuum should be lost, tethering the center of the metal membrane to the hub should prevent large deflections of the metal membrane resulting from wind or gravity loads. This would prevent destruction of the membrane.

7.3.1 Reflective-Membrane Central Seal

The reflective-membrane seal a collapsible bellows. One end of the bellows seal attaches to an adapter on the hub and the other end to a ring on the reflective membrane. When the reflective membrane is installed, it has a conical shape. The nadir of the cone is 85 percent of the depth of the formed metal membrane. The bellows extends from a fixed ring on the hub to the central hole in the reflective membrane. As stabilization vacuum is applied, the air is evacuated between the reflective and metal membranes bringing them into contact. The central bellows collapses to permit this movement.

The central bellows is molded from a Hypalon coated fabric. This material is flexible at all ambient temperatures and resistant to the effects of weathering. The bellows should last almost as long as the entire structure. The original bellows is a single, continuous molded piece. It is installed on the hub before the front spokes are attached. When it requires replacement, the replacement bellows has a zippered seam to permit its installation around the hub. The bellows are retained by clamp strips on the inside circumference of the collars. The front end of the bellows attaches to a free spacer ring, which in turn fastens to the inner edge of the reflective membrane. The free-spacer ring is required to adapt the bellows to the large inside diameter of the reflective membrane. The large inside diameter is used to permit field replacement of the bellows and access to the formed metal membrane's central tether.

The central-seal bellows serves the additional function of directing rain and melted snow to a central drain. Since the dish is stowed facing upwards, accommodation must be made for drainage from the center of the membranes. The central bellows serves as a funnel to direct run off to holes through the wall of the central hub. The water can then drain out the open rear-end of the hub. The hub wall is reinforced with a band where the drain holes penetrate

it. The drain holes' total area is small in order to not weaken the hub. The reinforcing band is formed from steel angle. A separate free-ring is bolted to this angle to create a larger ring for the seal termination.

7.3.2 Metal-Membrane Central Seal

A second flexible seal extends from the fixed ring on the hub to the inside diameter of the formed-metal membrane. This seal is not a bellows because the metal membrane does not move. It is flexible because, during operation, the optical-element ring will shift relative to the hub causing the hole in the metal membrane to assume a position that is not concentric with the hub. This flexible seal is installed with slack, so that minor movement of the metal membrane is not resisted. Larger movement of the metal membrane is prevented by this seal. If stabilization vacuum is lost and the wind causes the membrane to become convex, this seal will prevent the center of the membrane from displacing in the axial direction.

The central metal-membrane seal is constructed of PVC coated polyester cloth, the same material as used for the rear membrane. It has very high tensile strength and tear resistance. It is secured in the same manner as the bellows with a slightly thicker clamp strip. The seal also has a hem with a sewn-in rope for extra pullout resistance. This is the same method of mounting as is used for the rear membrane.

7.3.4 Rain-Grating Ring

A stainless-steel ring is installed in the annular space inside of the spacer ring using the same fasteners as the bellow's clamp ring. This slotted part serves as a debris grating to prevent clogging of the drain holes through the hub. The grating ring is made as a split-ring to simplify installation. It can be readily removed to permit access to the bolts retaining the molded bellows and tether. A PVC-coated cloth collar closes the gap between the rain-grating ring and the hub. The outside diameter of this collar bolts to the grating ring. The inside diameter has a hem sealed about a rigid metal ring that loosely fits the hub. This will prevent debris from over flowing the grating into the hub drains and still allows the collar to move up and down the hub as the polymer membranes move.

7.4 Spokes And Spoke Attachments

The spokes serve to transmit all wind and gravity loads on the membranes, PCA, and ring to the hub. The front spokes, as described in Section 6, define the torsional and translational stiffness of the ring relative to the hub. These functions create a purely axial load in the spokes. The rear spokes also carry the combined stabilization vacuum and wind dynamic pressure load acting on the rear membrane. This results in both an axial load and a distributed load applied along the entire rear spoke length. The nature of the loads and the way the spokes respond to them define the type of spoke termination that is most suitable. The rear spokes incorporate

a spring element to reduce their effective stiffness when initial stabilization vacuum is first applied.

7.4.1 Front Spokes

The spokes are loaded only in tension. Original designs used round rod for these elements. Calculations of total shading of the dish aperture indicated that a narrower spoke would be advantageous to offset unavoidable shading by other components. Since the loads all are tension, the use of a non-circular cross section has no adverse structural effect. The method of terminating the spokes at the hub and ring must accommodate both small angular changes during operation and small assembly misalignments.

Calculations for the optical-element structural integrity defined the loads and the required stiffness for the front spokes. Additionally, minimum cross-section was desired to minimize shading. Alloy steel (type 4140, yield stress = 758 MPa or 110,000 psi) was selected as the spoke material to achieve a high stiffness per unit area and to maintain an adequate factor of safety on stress. The spokes operate with a factor of safety of 3.3 over yield in worst case loading. The cross-section is 21 mm x 6.4 mm (0.81" x 0.25").

Alloy steel bar is not readily available in the lengths required for the front spokes. Forged ends to the spoke sections was initially investigated. Welding the steel bars followed by post-weld heat treatment to the low state of temper required was determined to be a more cost-effective manufacturing procedure. The design evolved to include a welded splice in the body of each spoke and welded on ends for interface to the hub and ring (see Figure 7.8). Both end details are identical to improve manufacturability.

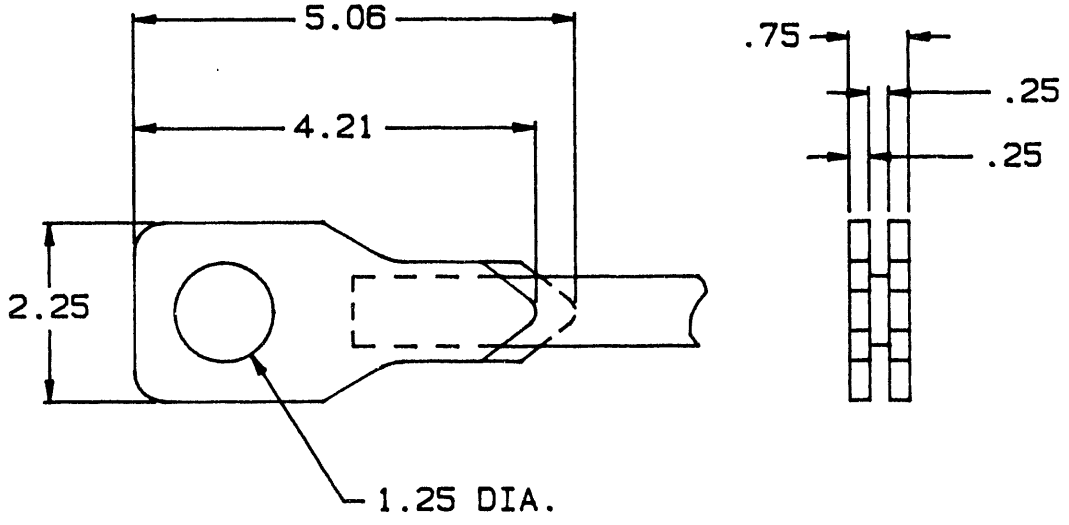

Figure 7.8 Front-Spoke End Detail.

The spoke pattern was slightly modified to simplify its attachment to the hub. The original pattern had the spokes attached to the hub 5.6 degrees away from a true tangent. This caused the attachment hardware to be asymmetrical and more difficult to machine and assemble. It also prevented small angular changes in the spoke without binding the pin or bending the spoke. The hub attachments were moved so the spoke was tangent to the hub. The pierced ears at the inner end of the spokes are pinned to the hub with a hollow headed sleeve (see Figure 7.9). This pre-stressed bolted joint is intended to transfer the spoke tension to the hub through friction. If for any reason the bolt pre-load is lost, it is sufficiently strong in plain shear to carry loads. The hub required local reinforcing to reduce bearing stresses in the hub wall caused by shear forces if the bolt pretension should be lost.

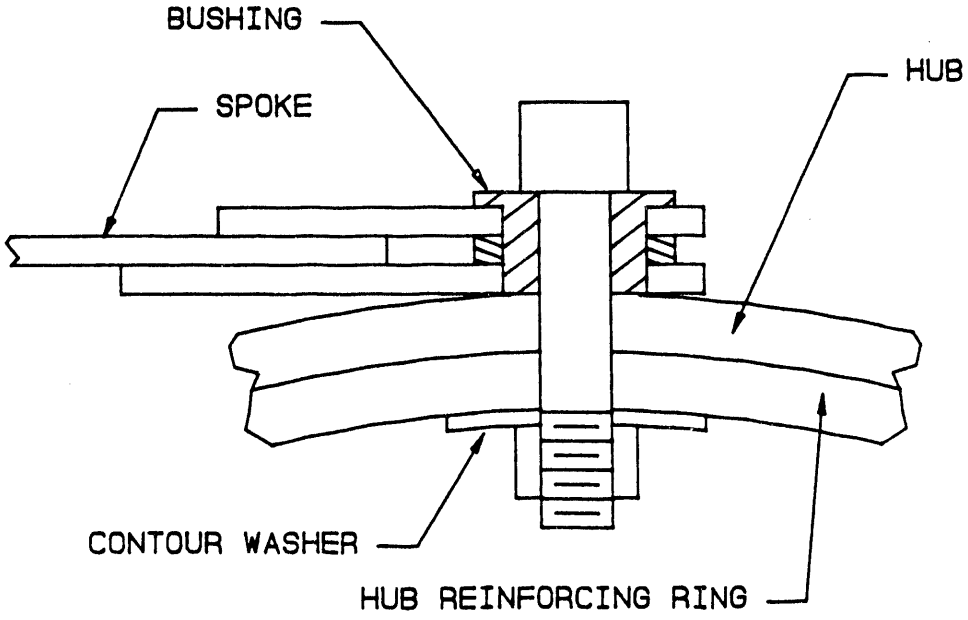

Figure 7.9 Front-Spoke-to-Hub-Attachment Detail.

The spoke splice is achieved by both welding the spoke sections directly and by use of two splice plates (see Figure 7.10). The splice plates provide extra weld area to increase the factor of safety on the weld.

The front-spoke attachment to the ring (see Figure 7.11) is designed to apply the spoke tension to the optimum point relative to the ring centroid as determined in the analysis described in Section 6.0. At the same time, the attachment hardware must allow access to the membrane clamp bar for reflective membrane installation or replacement. Radial misalignment of the spoke, inherent in the assembled spoke pattern, is allowed by independent adjustment of the two-pin retention screws. The use of a pinned connection through the spoke allows slight changes in spoke out-of-plane angle that occur during operation. Each nut is supported on a spherical washer set to prevent binding.

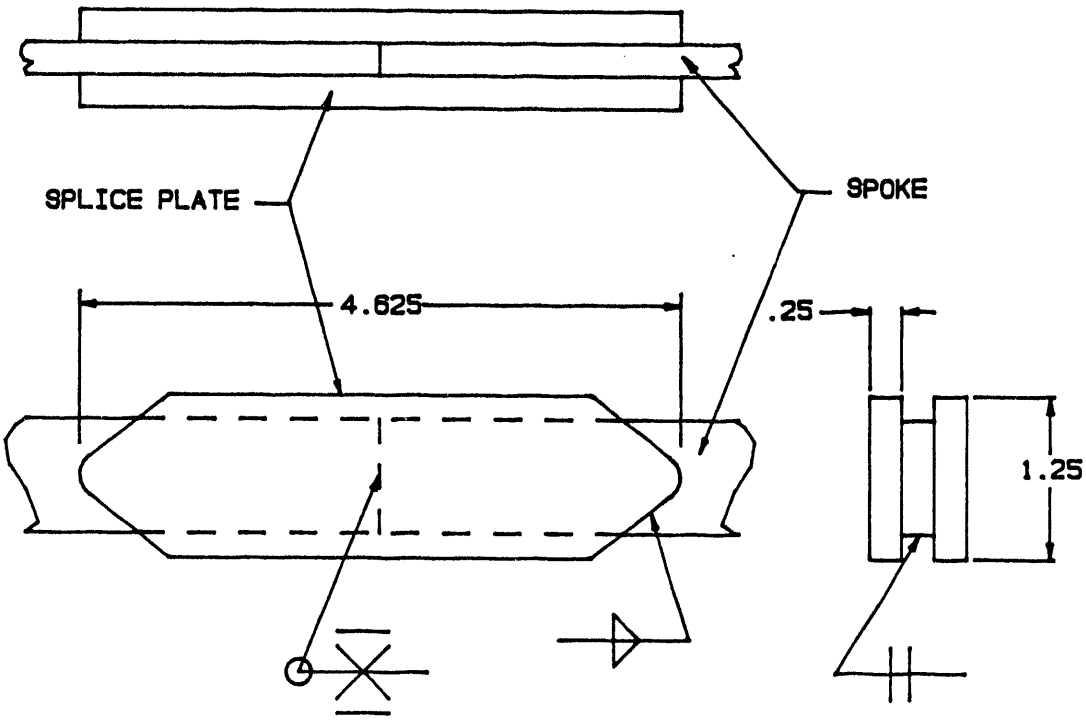

Figure 7.10 Front-Spoke Splice Detail.

The front-spoke brackets are welded to the ring and aligned with a true radius. The spokes are installed in right- and left-hand fashion such that the spokes, however, do not run truly perpendicular to the ring. The two-pin retention bolts are used to compensate for this difference. The spoke brackets are simple weldments with common commercial tolerances. The welds to the ring are loaded primarily in shear.

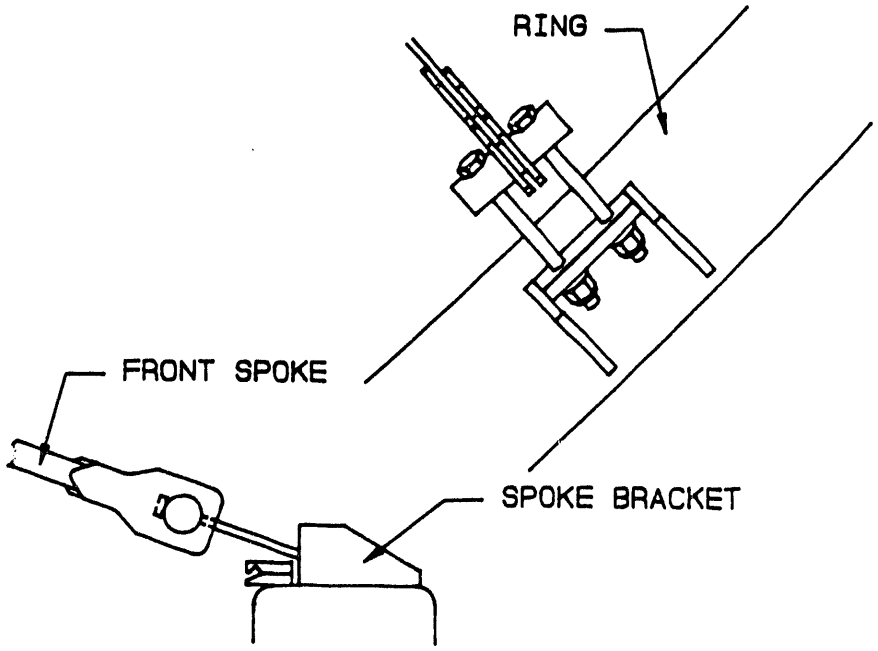

Figure 7.11 Front-Spoke-to-Optical-Element Ring Attachment.

7.4.2 Rear Spokes

The rear spokes are round for easier processing because shading is not an issue. The rear spokes carry a distributed transverse load from the rear membrane that is draped over them. They are required to "sag" under this load to support the rear membrane and to limit peak tension in the spokes. This precludes use of identical spokes to those on the front of the optical element.

The rear spokes are 4140 alloy steel to provide an acceptable factor of safety. The diameter is 13 mm (0.50 inches). Peak loads in the rear spokes are somewhat lower than in the front spokes so the factor of safety is even better. Notching and area reductions of the spoke are avoided by using rolled threads for the terminations.

The rear spoke attachment points to the ring were determined to be several inches from the rear face of the ring in order to keep the front and rear membranes separated (see Figure 7.12). When the stabilization vacuum is applied to the rear membrane, it causes the rear spoke to sagand the change attachment angles change at both ends. This change is approximately 10 degrees at the ring end, much greater than that experienced by the front spokes. The design accommodates this by use of a spherical mono-ball bearing at the two ends.

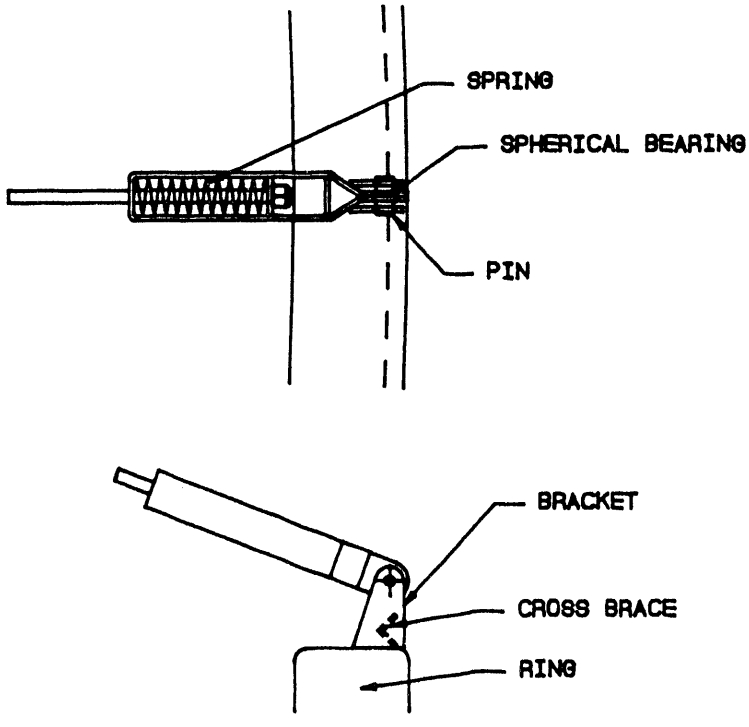

Figure 7.12 Rear-Spoke-to-Optical-Element Ring Attachment and Spring Element.

The attachment to the hub uses a spherical rod end (see Figure 7.13) that threads onto the spoke end directly. The rod-end eye is bolted to the reinforced hub in a similar fashion to the front-spoke attachment. The bolted joint is pre-tensioned to avoid gaps under any spoke load. The hub is reinforced at the spoke attachments.

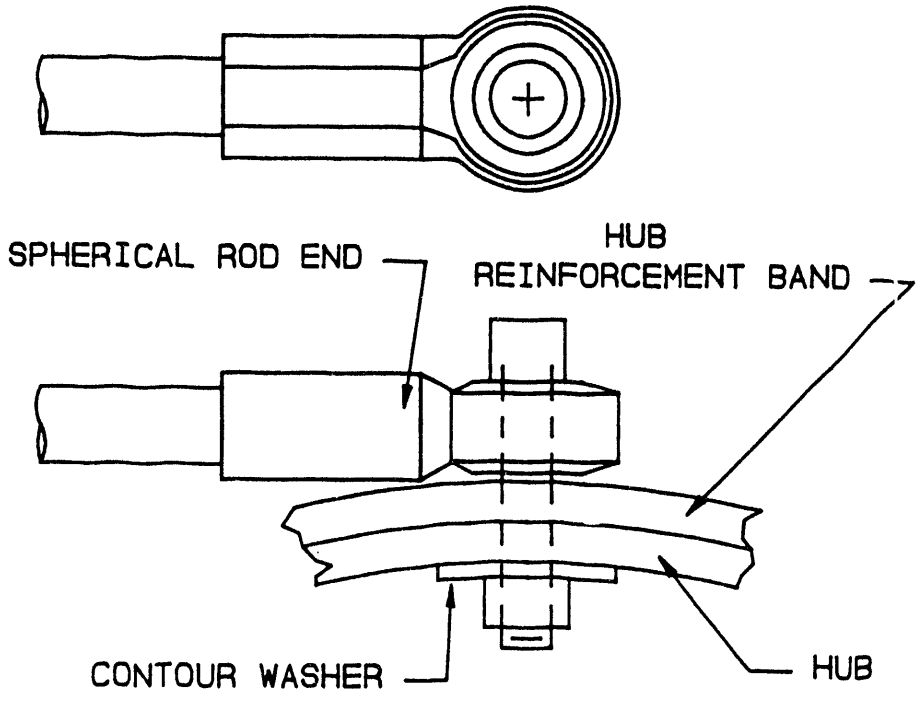

Figure 7.13 Rear-Spoke-to-Hub-Attachment.

7.4.3 Rear-Spoke Spring Assembly

The rear spokes require a spring and gap element to permit them to sag a controlled distance under the distributed loads rear-membrane, as discussed in Section 6.0. The sag reduces the spoke tension and the loads on the ring. It must be limited to prevent the rear membrane from contacting the back of the reflective membrane. The spring element permits an initial tension to be put into the rear spokes during assembly to provide structural stability for the optical-element structure. When stabilization vacuum is applied, the rear membrane is drawn inward causing the rear spokes to deflect and lengthen, which compresses the spring. There is a preset stop on each spoke to control the total deflection.

The spring assembly is shown in Figure 7.12 in the as assembled condition before stabilization vacuum is applied and before the spring is pre-tensioned At one end, a spherical bearing is installed to pin the assembly to the ring-mounting brackets. The threaded end of the spoke passes through the opposite end of the spring assembly. A nut and washer set permit tightening of the nut to compress the spring a prescribed amount to pretension the spoke. A sleeve placed

around the spoke inside of the spring serves as the stop. The length of this sleeve is predetermined to provide the desired gap when it is compressed to the pretension value.

7.4.4 Rear-Spoke Mounting Bracket

The rear-spoke mounting bracket is a simple weldment. It is cut from steel plate and standard angle. It is pre-welded and bored for the spoke pin. The subassembly is then welded to the ring. The bracket is sized so the rear membrane drapes over the bracket exactly as it drapes over the rear- membrane standoff rail.

7.5 Hub and Drive Interface

The hub is a tubular member with local reinforcing in several locations (see Figure 7.14). The outer end has an internal band added where the front spokes bolt in place. Near the rear end an external band is located where the rear spokes bolt to the hub. A third band reinforces the area near the center where drain holes penetrate the wall for membrane drainage. Also near the rear of the hub is an external ring to fasten for the rear membrane. There is a set of vertical blades that extend from the rear of the dish up into the hub to stiffen it. On the very rear of the hub is a pair of spherical bearings for the elevation axis and a lever arm for the elevation-actuator attachment.

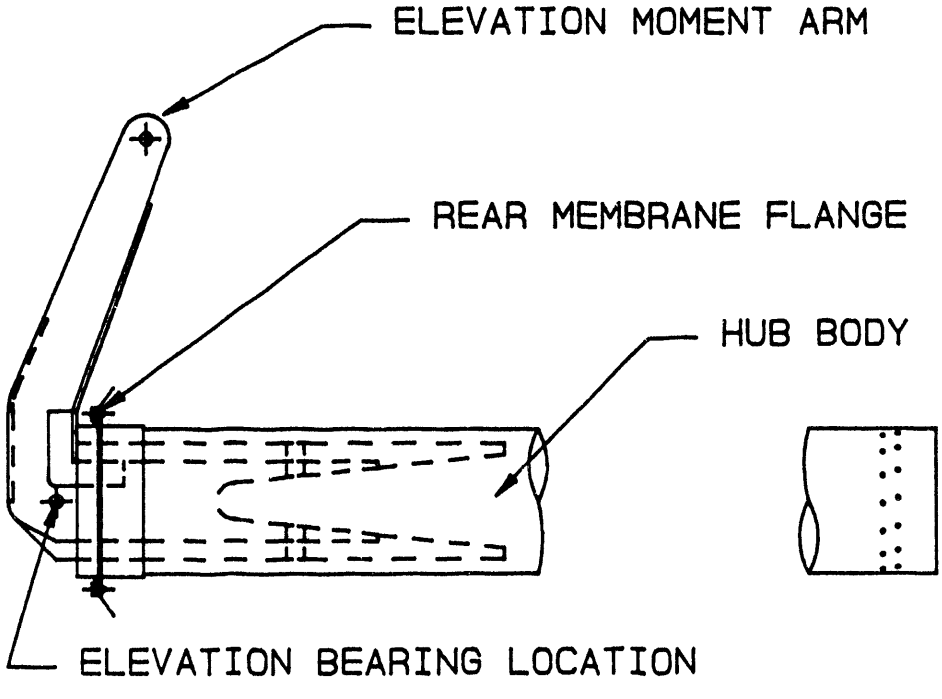

Figure 7.14 Hub and Hub-Reinforcement Details.

The main body of the hub is 610-mm (24-inch) diameter steel tubing (ASTM A-106, yield 241 MPa [35,000 psi]) with a 6 mm (0.25 inch) wall. This is a commercially available schedule 10 pipe material. Where low quantities may cause an availability problem, this diameter and thickness can also be brake formed from A-36 flat plate. The reinforcing rings and the membrane mounting ring are welded to the hub body.

The stiffening blades are sized to reduce the bending moment in the hub under worst case loading. The blades are shaped to provide a gradual change in net hub section modulus to avoid stress concentrations. The stiffening was defined by stress requirements, but also serves to reduce deflection of the hub and increase stiffness.

The lever arm and stiffening blades are welded as a complete subassembly prior to inserting them into the hub body. After insertion, the blades are stitch welded to the hub from the inside. Most welds can be made from the rear end of the hub. The hub is large enough to permit a person to enter it from the front end to weld the blade tips. The stiffening blades are integral with the elevation drive lever arm assembly. The loads are very high in this assembly so the integrity of the assembly is critical. Welds in the primary load path are minimized by cuttingeach lever arm and stiffener blade as a single piece from steel plate. At the inside corner of the blade/lever arm pieces, a doubler is welded in place to reduce stress concentrations. The weldment is designed to avoid critical bolted joints and expensive certified field welding. Elimination of field welding also permits high reliability surface finishing of the completed hub assembly for corrosion resistance. The specified finish is hot dip galvanizing.

The pivot axis for the elevation motion passes through the heel of the stiffener/lever arm assembly. The pivot is designed to use two mono-ball bearings. These bearings can accept very high radial loads and permit simplified fabrication and assembly because of their self-aligning capabilities. The bearing outer race is supported in an ear on the rotating azimuth stage and is retained by internal spring rings. The stiffening blades on the hub are arranged in two pairs. Each pair supports a pin that passes through the ball of the elevation bearing. The inner race is clamped to the pin using custom bushings. The bushings also serve to support the pivot pin in over-size holes in the stiffener heel. The holes are oversize to permit the entire spherical bearing to pass during removal and replacement.

The main body of the hub is 610-mm (24-inch) diameter steel tubing (ASTM A-106, yield 241 MPa [35,000 psi]) with a 6 mm (0.25 inch) wall. This is a commercially available schedule 10 pipe material. Where low quantities may cause an availability problem, this diameter and thickness can also be brake formed from A-36 flat plate. The reinforcing rings and the membrane mounting ring are welded to the hub body.

The stiffening blades are sized to reduce the bending moment in the hub under worst case loading. The blades are shaped to provide a gradual change in net hub section modulus to avoid stress concentrations. The stiffening was defined by stress requirements, but also serves to reduce deflection of the hub and increase stiffness.

The lever arm and stiffening blades are welded as a complete subassembly prior to inserting them into the hub body. After insertion, the blades are stitch welded to the hub from the inside. Most welds can be made from the rear end of the hub. The hub is large enough to permit a person to enter it from the front end to weld the blade tips. The stiffening blades are integral with the elevation drive lever arm assembly. The loads are very high in this assembly so the integrity of the assembly is critical. Welds in the primary load path are minimized by cuttingeach lever arm and stiffener blade as a single piece from steel plate. At the inside corner of the blade/lever arm pieces, a doubler is welded in place to reduce stress concentrations. The weldment is designed to avoid critical bolted joints and expensive certified field welding. Elimination of field welding also permits high reliability surface finishing of the completed hub assembly for corrosion resistance. The specified finish is hot dip galvanizing.

The pivot axis for the elevation motion passes through the heel of the stiffener/lever arm assembly. The pivot is designed to use two mono-ball bearings. These bearings can accept very high radial loads and permit simplified fabrication and assembly because of their self-aligning capabilities. The bearing outer race is supported in an ear on the rotating azimuth stage and is retained by internal spring rings. The stiffening blades on the hub are arranged in two pairs. Each pair supports a pin that passes through the ball of the elevation bearing. The inner race is clamped to the pin using custom bushings. The bushings also serve to support the pivot pin in over-size holes in the stiffener heel. The holes are oversize to permit the entire spherical bearing to pass during removal and replacement.

The lever arm consists of four blades reinforced with a web section on the front and back. The lever arm's function is to provide a moment arm and attachment point for the linear actuator that controls the optical element elevation angle. The outer end of the lever arm has a large diameter pin that passes through all four blade elements. The elevation jack screw attaches to this pin by means of a spherical rod end. The pin is removable for replacement of the spherical bearing. Sleeves on the pin keep the rod end centered on the pin. Collars of abrasion resistant, self-lubricating polymer capture the rod end and prevent it and the ball screw from twisting about the ball-screw axis during operation.

7.6 Vacuum Systems

The function and controls for the membrane stabilization vacuum-control system are described in Section 4.2. This section describes the physical mounting of the required hardware. The blowers are mounted on the azimuth stage of the drive so the connecting hose does not have to accommodate the relative motion between the pylon and the optical element. The same is true of the pressure transducer and high-vacuum limit switch. The signal and power wires for these devices are routed with the signal and power cables for the PCA, position encoders, and elevation motor.

The vacuum hoses for the sensors and blower all connect to the optical-element plenum via bulkhead fittings in the hub wall. To minimize field labor, these fittings are factory installed along with the required length of hose to reach each device. Installation and replacement of the rear membrane is simplified by not having to cut holes in the membrane and add bolted reinforcing flanges for tubing connections. Integrity of the membrane is not compromised by cutting holes in it for connections either.

The electrical devices are mounted within a NEMA enclosure to protect them from the weather. The blowers do not have sealed motors so they are also inside the enclosure. The enclosure has vent openings to permit the blower exhaust air to escape. The enclosure is mounted to the base plate of the elevation drive. Because the attitude of this part does not change with elevation angle, the required air exhaust ports always point downwards to prevent rain entry. Also the position sensitive, low-pressure-differential pressure transducers do not change orientation.

The sensors have their high-pressure ports vented to the outside of the enclosure so the back pressure from the blower exhaust does not disturb the differential pressure being measured. The ports are terminated in porous, sintered-bronze plugs that allow air to pass freely but prevent insects from making webs or nests in the tubing openings and blocking free flow of air. The low-pressure ports are connected to bulkhead fittings in the enclosure wall so final field connections can be made instantly without opening the enclosure. The enclosure is also pre-wired with a pre-cut length of cable attached for connection to the dish controller on the pylon base. No field connections need to be made at the top of the pylon.

8.0 Manufacturing Cost Estimates

There are three major components necessary for a solar dish engine technology to be commercially successful. These are performance, reliability, and total life-cycle cost. A critical factor for the total life cycle cost of the stretched-membrane dish technology is the manufactured cost. In this section, cost estimates will be presented for the first prototype and for a modest production volume of 100 dishes per year.

A description of activities required to fabricate a stretched-membrane dish is also included. Major assumptions as to manufacturing procedures and facilities that affect the costs estimates are also discussed.

8.1 Single-Prototype Fabrication

For a single prototype to be assembled, considerable investment in engineering and fabrication of new tooling is required. The actual dish fabrication takes place in two phases: shop fabrication of all components and subassemblies, and field assembly and installation. A subsequent period of shakedown testing and debugging should also be anticipated. The cost of these activities is summarized in Table 8.1 in 1992 dollars.

Table 8.1
Complete Costs for Fabrication of First 10.4-M Prototype Dish

ITEM	COST
Engineering of processes and tooling	$150,000
Tooling fabrication	$620,000
Optical element fabrication in Dallas	$411,000
Assembly & Installation *	$213,000
Test support, management, & reporting	$140,000
	$1,534,000

*Assumes installation at SNL, New Mexico

8.1.1 Engineering and tooling

Engineering of processes and tooling includes some refinements to the existing design plus the design of the 10.4-m membrane forming tooling, membrane rolling and unrolling system, field assembly tooling, portable departure bar milling machine, and membrane measuring system modifications.

The scale of the membrane forming operation is too large for Solar Kinetics' existing assembly area. A portion of SKI's existing outdoor test park will be used instead. Two possible approaches to the forming tooling are being considered. One would be a larger-scale version of the steel tooling ring with a reinforced fabric bottom membrane, as was used for the 7-m forming operation. This has the advantage of requiring a modest engineering development effort and may offer the possibility of sectional tooling for later relocation. The alternative is to use a concrete tooling ring set into the ground. The bottom may be a reinforced membrane or may be a simple liner with enough water to overcome the forming vacuum. The water approach eliminates the highly tensioned membrane with its attendant risk of failure and the high loads it imparts to the tooling. The sunken tooling ring would also permit most work to be easily performed from ground level, which is generally much more efficient.

The new tooling will be simpler than the 7-m tooling because it will have a permanent departure bar for supporting the membrane periphery during forming. The 7-m tooling supported the actual optical-element ring for this purpose.

After the tooling is installed, the forming operation will be enclosed in a rented, portable, wide span, sprung frame fabric building. The building is erectable in two days with minimal ground preparation. It is available with unsupported spans of 10 to 36m (60 to 120 feet) the narrow direction and in almost unlimited length. A 18 by 18m (60 foot by 60 foot) structure is planned. The entire end of the building can be opened for equipment access. Its covering is the same type of plasticized cloth from which the rear membrane is fabricated. After forming operations are complete, the same building will be knocked down, shipped to the field installation site, and re-erected for field assembly operations.

The membrane-rolling operation implemented at the 7-m scale was manageable, but required almost a dozen workers. The larger 10.4 m rolling operation is planned to use more powered controls and less brute strength. This will reduce risk to both personnel and the completed membrane. It will also serve as a development tool for the more practical production operations to follow. As much as possible, the same mechanisms will be used in the field for membrane unrolling.

For use in the field, assembly tooling will support the ring sections while they are welded together. After welding, it will also support the ring while the departure bar is milled and during the installation of metal membrane. The fixture will then lift the ring and membrane high enough for the hub to be inserted from beneath the membrane. This will permit the hub

and elevation moment arm to be factory assembled. It also reduces the risk to the membrane associated with the prototypical practice of lowering the hub down through the membrane center hole. The ring is then lowered to an intermediate height for the final assembly of the spokes and rear membrane.

The assembly tooling will be designed concurrently with the portable milling machine. The assembly-fixture ring supports must not interfere with the milling machine as it travels about the ring. The assembly tooling must anticipate the site conditions where the dish will be built. Many sites will not have a concrete floor. The tooling must not be dependent on such a foundation to maintain its accuracy.

The tooling will be fabricated at SKI in Dallas with some components subcontracted to local fabricators and machine shops. Some of the large items, such as the membrane rolling mandrel and the rotating reference arm, may be fabricated at the remote site along with the forming tooling.

8.1.2 Optical-Element Fabrication

The optical-element components and subassemblies will be fabricated in Dallas, primarily at SKI's facilities. Some items that require unusually large equipment will be subcontracted. These include:

a. section hot induction rolling,
b. spoke post-welding heat treatment, and
c. pylon fabrication.

Surface finishing for most parts will be hot-dip galvanizing, which will also be subcontracted.

Some operations such as the spoke welding might more efficiently be conducted by subcontractors experienced with certified welding of high-strength alloys. However, where this is a prototype of future production models, this is a good opportunity for the manufacturer to gain experience with the qualification procedures.

Forming and rolling the membrane will be conducted at a remote site in Dallas under a temporary shelter as previously described.

8.1.3 Field Assembly and Installation

For purposes of this estimate, it was assumed that the dish would be erected at SNL. Site operations include:

a. foundation installation,
b. area preparation for temporary assembly building,
c. building erection,
d. assembly tooling installation,
e. optical element assembly,
f. pylon and drive installation,
g. optical element installation, and
h. start-up.

The area for the temporary assembly building should be paved to minimize dust during the assembly. Anchors driven through the pavement will secure the temporary building. Actual erection of the building requires only two days.

Pylon and drive installation may occur at any time after the foundation concrete has cured. It may be most cost-effective to schedule it immediately prior to optical element installation. A crane will be required for both operations, so mobilization costs for the crane can be minimized by scheduling.

The temporary building handling crew should be scheduled just prior to this operation. The building must be removed for the crane to gain access to the optical element.

A temporary stabilization vacuum source must be connected to the optical element during its transport from the assembly tooling to the support pylon. This will ensure that any sudden movements or wind gusts during transport do not disturb the formed metal membrane.

8.2 Volume Production

While the goal of this technology is to provide bulk power on a large scale, this cannot be accomplished until the technology has proven itself, and the industry is capable of producing systems in large quantities. Before that can be achieved, dish systems will have to be fielded for sufficient time to demonstrate reliability, availability, and net power generation capability. During the introductory phase, unless a company or government is capable of sustaining very large long-term investments, the dish-engine systems will have to be cost-effective for the applications in which they are installed. These initial installations will be niche markets where conventional electric power is expensive, unavailable, or unreliable. The dish engine systems will have to compete with other emerging alternative energy technologies such as photovoltaics, wind, or simple fossil-fueled cogeneration. From this context, it can be seen that even

low-volume production of dish engine systems must be cost-effective for the target applications in order to provide a stepping stone to wide spread usage.

An annual volume of 100 dishes per year was chosen for development of manufacturing costs. This volume will permit almost all manufacturing operations to be brought in-house for reduced costs and better production and quality control.

The selling price for the installed collector (less receiver and engine) would be $73,000. This is equivalent to $857 per square meter of gross reflective aperture or $2900 per kW electrical power capacity. The components of these costs are summarized in Table 8.2

Table 8.2
Summary of Manufacturing Costs
(Rate of 100 Per Year)

Total Labor Cost	$ 10,766.00
Total Material Cost	55,442.00
Profit	6,620.00
Selling price	$ 72,828.00

These costs were determined by the following formulae.

1. Base labor rates:
   - Skilled labor — BLR-1
   - Semi-skilled labor — BLR-2
   - Unskilled labor — BLR-3
2. Burden: — BUR
3. Material Overhead: — MO
4. G & A — G
5. Profit — P

Total Labor =

Hrs-1 * BLR-1
Hrs-2 * BLR-2
Hrs-3 * BLR-3

Sub-total * (1 + BUR) * (1 + G) = TL

Total Material = Cost * (1 + MO) = TM

Selling price = (TL + TM) * (1 + P)

A separate overhead is used for labor and material due to the material intensive nature of this operation. Several large sub-components are purchased from other vendors. The components include significant labor for their manufacture, reducing the labor required in this operation. The values used for the rates and burdens (see Table 8.3) were based on SKI's experience in manufacturing engineered solar thermal products and systems.

Table 8.3
Values Used for Manufacturing Cost Estimating
(Rate of 100 Per Year)

Skilled labor rate	12.00	$/hr
Semi-skilled labor rate	7.00	$/hr
Unskilled labor rate	5.00	$/hr
Labor burden	0.60	
G & A	0.30	
Material OH	0.15	
Profit	0.10	

The profit of 10% ensures an adequate return on shareholder equity of five million dollars at an opportunity rate of 7.5% with a 50% risk factor.

The manufacturing cost is distributed between the major sub-systems of the dish (see Table 8.4). The manufacturing labor is based on engineering estimates presuming the existence of tooling that is still conceptual in nature at this writing. SKI's experience with fabricating, handling, attaching, and forming membranes is the basis on which the authors made these estimates.

Table 8.4
Selling Price Breakdown for Dish Subsystems
(Rate of 100 per Year)

Optical Element	22,705	31%
Drive	13,634	19%
Support	16,370	23%
Controls	5,377	7%
Assembly/installation	14,741	20%
Total	72,827	100%

Membranes are to be fabricated from coil stock on a long layout table with two traveling weld heads. This will permit two panels to be welded simultaneously. The welder will be a solid-state direct energy unit for higher frequency cycling than the transformer unit used on the prototypes. The table will have a powered take-up winder for the completed membrane and mandrel.

The membrane forming tooling will consist of a tooling ring sunken in the floor so that the edge where the membrane attaches is readily accessible. Two parallel tracks will straddle the tooling to support the membrane mandrels during installation and removal. The mandrels will have automatically coordinated travel and unwind/rewind functions. Multiple membrane edge grippers mounted on radially positioned actuators will apply biaxial tension to the membrane during fixturing.

Forming will be accomplished with the current combination of uniform and non-uniform pressures. Shape monitoring will be automated by use of ultrasonic non-contact range sensors placed at periodic radial locations under the membrane. These sensors will provide data for control of forming pressures and documentation of finished membrane shape. As more manufacturing data is accumulated, continuous improvement in membrane quality and repeatability will occur through more accurate compensation for variations in membrane material mechanical properties.

Of the other fabricating operations, the optical-element ring rolling will offer the greatest return by being in-house. A dedicated, induction-heated hot-rolling machine will be used for high accuracy and repeatability. Capital costs will be minimized if this machine is built for a single radius and tube cross-section. These parts will be rolled in-house to eliminate significant shipping and handling expenses in addition to eliminating vendor markups.

Another operation, which could be brought in-house to reduce redundant shipping and handling, is the hot-dip galvanizing finishing. Almost all steel parts require this finishing after fabrication and before final assembly. Careful review of the costs for setting up such an operation would be required. There may be considerable costs associated with environmental controls and procedures and personnel safety issues that a specialized vendor can address more effectively.

It is presumed in the cost estimates that the rear membrane fabrication will be performed in-house.

Only a few significant components will not be built in-house. One is the azimuth drive, as this requires considerable capital equipment and experience for casting and gear manufacture. The tracking controller may be another component that is more cost-effective to purchase, since the volume is low by circuit board fabrication standards and an existing manufacturer is extant.

9.0 Relation of 10.4-M Design to Previous Work

The 10.4-m design described in this report is a culmination of several development efforts. Various techniques and designs were tried in those efforts to determine the best, or at least a viable, solution to the innumerable design and fabrication challenges of this unique project. This section will describe how the current design builds on earlier design tools, concepts, and fabrication techniques. There are still many issues that require better understanding for this technology to be commercialized. These will be also discussed.

The term design tools is meant to include the analytical concepts used to predict collector performance and their embodiment software programs or written techniques. Collector performance includes structural response to loads, drive actuator geometry, and loads and collector energy balances. Collector performance measurement techniques are also included as design tools.

Design concepts are the physical relationships between the collector components. This includes such things as the load paths through the structure, type of drive selected, and trade-offs between manufacturability and weight minimization.

Fabrication techniques are concerned with manufacturability; i.e. how to achieve the required performance, and minimize the system costs. This includes such issues as predicting how the shape of larger membranes will be controlled during forming; how to minimize field erection time; and how to achieve least cost, highest reliability joining.

9.1 Design Tools

Experience with and measurements of the 7-m optical element have not revealed any shortcomings of the analytical techniques used in its design. In general, the 7-m design was successful both structurally and optically. While the general approach is sound, there still may be considerable conservatism in how the loads, stresses, and deflections are calculated. Some conservatism was intentional in the first-of-a-kind unit. Each future iteration should reduce the unneeded margins to increase cost-effectiveness.

In the current effort, the design tools used on the 7-m unit have been refined and additional analytical techniques have been applied to confirm the earlier methods. More extensive FEA modeling of the ring and its interaction with the spokes, membrane, and hub has been completed. More thorough application of wind tunnel test results have been made to predict wind loads at a variety of orientations. Results from several optical performance measurement techniques have been compared to each other and to theory.

predict wind loads at a variety of orientations. Results from several optical performance measurement techniques have been compared to each other and to theory.

After completion of the 7-m optical-element prototype, it was important to make the best practical measurement of its performance before initiating design of the next iteration. The measured performance would provide feedback to indicate where changes in the existing design theory should be investigated.

9.1.1 Measurement Techniques

Results from several measurement techniques used on the 7-m prototype were compared with each other. This was a significant step towards confirming their accuracy and demonstrating their value as tools to support further development activities. The measurement techniques referred to are the Video Ray Trace (VRT) system and two simpler systems used at SKI, plus the Beam Characterization System developed by SNL.

The VRT system reflected a computer-direct laser beam off a reflective membrane onto a target. A video camera viewing the target digitized the laser strike location, and the computer solved for the slope error at that point. This system is described more fully in previous report (2).

SKI uses a mechanical measurement system during forming. This system utilized finely graduated vertical rods running in carefully plumbed tracks to follow the membrane surface as it was pulled down during forming. An optical surveyor's level was used to view the graduated rods to determine the membrane displacement at selected radial positions. Slope was calculated from the displacement differences.

A third measurement method used a horizontal laser beam turned by a penta-prism to strike the membrane normal to the ring plane. The laser beam was reflected off a small mirror placed on the membrane directly under the prism and directed to a grid target. The prism and mirror were repositioned to selected radial and angular positions to define local membrane slope. The location of the reflected laser strike on the target grid permitted calculation of the membrane slope at each point of interest.

The BCS system is used on a completed concentrator operating on-sun. A video image of the concentrated flux on a temporary, temperature-controlled target is digitized and analyzed. The digital map of flux concentration is compared iteratively with a computer model of the reflector surface. Variables are changed to get a best fit between the measurements and the model results. A composite view of various reflector characteristics can then be inferred from the values used in the best fit model (3). This system measures the total error of the dish at the receiver plane.

whether still in the forming tooling, in the assembly tooling, or completed and mounted on a drive and support pylon. The VRT system is appropriate for a reflective concentrator. The BCS system is intended for fully operational dishes.

Confirmed multiple measurement tools to yield similar measurements for varying stages of concentrator fabrication is very valuable. For concentrator production, as in any manufacturing situation, in-process measurements made before the final system is completed are essential for cost-effective manufacturing. The information this data provides permits consistent final product performance in spite of intentional or inadvertent changes in raw material properties or the fabricating process.

Table 9.1 7 M Prototype Optical-Element Slope Error Measurements

METHOD	SLOPE ERROR	MEASURED UNCERTAINTY
BCS System	2.3 mrad	0.2 mrad *
Penta-prism system	3.1 mrad	0.6 mrad (2)
VRT System	3.6 mrad	0.5 mrad (2)

*Based on reported 8% uncertainty of peak flux measurement. (3)

9.1.2 Analytical Models

Many classical analytical techniques for stress and deflection calculation were applied to the 7-m dish design. This also required models for calculating the loads on the ring, spokes, and membranes using free body analysis to balance forces and sum moments. A computer worksheet entitled RINGSZ which combined the load calculations for the optical-element ring with several classical structural analysis formulas was described in Section 6. The summarization of many separate analyses into a single tool permitted quick iterations using various ring and spoke section properties and geometries to be compared under various wind, stabilization vacuum, and assembly pretension conditions.

Other worksheets were developed for calculating loads, stresses and deflections for the hub, PCA supports, pylon, and elevation drive. These all used classical approaches. Most had been at least summarily addressed in earlier phases of this work. The pylon stress and deflection calculations had been worked out by SKI for heliostat applications. WGA had worked out similar calculations for the faceted stretched-membrane dish support.

9.1.3 Rear Membrane Displacement

In Task 2, a model was developed to calculate the sag in the rear spokes when the rear membrane, drawn by the stabilization vacuum, acted on them. An additional FEA model of

9.1.3 Rear Membrane Displacement

In Task 2, a model was developed to calculate the sag in the rear spokes when the rear membrane, drawn by the stabilization vacuum, acted on them. An additional FEA model of the rear membrane was used to predict its response to uniform pressure loading. The results of these two approaches were superimposed to predict the degree of rear membrane displacement under stabilization vacuum. After the 7-m prototype was assembled, measurements were made of the actual spoke and membrane displacements. These measurements confirmed that the analytical tools were sufficiently accurate. This had been an important issue in the 7-m design because the rear membrane and the formed metal membrane were close together, any contact would have resulted in a local optical error. The sag of the membranes defined the height of the rear membrane standoff rail. For the 10.4-m design, this issue was much less critical because the membrane rear standoff rail height was driven by other considerations. Without the sag model, however, undue concern might have been given to the membrane spacing issue.

9.2 Design Concepts

Several fundamental design concepts were developed during the first two tasks of this effort. Since the 7-m prototype was built, several additional concepts were conceived and applied to the 10.4-m design. There were 4 major concepts developed in the early phases of this work, which are described in other reports (1, 2). These are as follows:

1. Free-form yielding of metal membranes to an accurate, parabolic contour.
2. Rolling a parabolic-formed metal membrane onto a rigid mandrel for transport and storage and unrolling it for assembly into a dish without damage. This permitted factory forming of the membranes for lower cost and increased process controllability.
3. Application of separate reflective polymer and metal membranes retained by edge clamping and light vacuum for a parabolic dish.
4. Application of a hub-and-spoke structure to supporting a parabolic reflector for a point-focus dish.

The successful demonstration of these concepts is the foundation for the current development work.

Experience with design and/or implemention of the prototype optical element and its components led to additional conceptual changes for the current design. These included:

1. Support of the optical element from a single point (cantilever drive);
2. High reliance on welded joints for improved manufacturing costs;
3. Field machining of departure bar after installation to ensure planarity and concentricity; and
4. Closed-loop control of stabilization vacuum.

9.2.1 Cantilever Support

The first 7-m optical element was mounted on a heliostat az/el drive using a large welded adapter. The support of the optical element was modeled after the conceptual design then planned for the final dish design. The adapter was a massive structure, although appropriately designed for a deflection limited application such as this. Inspection of this adapter plus analysis of the conceptual design and several other alternatives led to the realization that a single-point support eliminated redundant structural elements. It also reduced the stiffness requirements of the azimuth drive by reducing rotational inertia. More discussion of this issue is found in Section 3.

9.2.2 Welded Joints

The first optical element was designed with reliability as a prime objective. Many joints, which could have been welded, were bolted to eliminate weld qualification and the attendant testing and inspection requirements. This often required additional parts and more complicated joints than a welded joint requires. This was a cost-effective and appropriately cautious approach for a prototype. In a production operation, weld qualifying and inspection can reliably be assured using standard manufacturing procedures. This permits the use of fewer and simpler components for lower manufactured cost with no sacrifice in strength or reliability.

In the 10.4-m design, areas that use only welding include:

the front-spoke-brackets-to-ring attachment,
the rear-spoke-brackets-to-ring attachment,
the departure-bar-to-ring attachment,
the front-spoke ends clevis-to-spoke attachment, and
the departure-bar to ring attachment.

There are additional joints that rely on welding in the 10.4-m concentrator that do not exist in the 7-m prototype. All of these joints are conservatively loaded. The types of welds used are commonly used in many industrial applications. Only one joint could be considered unusually critical. The front spokes have welded splices along their length due to stock material length limitations for the high strength alloy. This area will require some post-welding heat treatment to maintain adequate yield strength. Only a mild level of

temper is required for the anticipated loads, so the heat treatment schedule is not unusual or difficult.

The departure bar will also be welded to the ring. This will eliminate the need to locate, drill, and tap hundreds of holes. It also allows the use of lighter wall tubing for the ring.

9.2.3 Departure Bar Machining

The departure bar concentricity and planarity are critical to assure accurate fit of the formed membrane to the optical element. The prototype used a segmented departure bar that was field installed. It required match drilling and tapping hundreds of holes in the optical-element ring. After it was bolted in place, continuous shimming was required to achieve planarity. This resulted in extensive field labor during dish assembly. In the new design, the departure bar is welded in place at the factory where labor is less expensive and more efficient. In the field, the ring sections are butt welded in an assembly fixture. A portable milling head then travels around the ring and machines the departure bar to the required planarity and concentricity. Little labor is required and high accuracy is assured without requiring fine tolerances on the initial field-ring assembly fixturing and welding.

9.2.4 Stabilization Vacuum Control

The 7-m diameter element had a fixed speed blower to maintain the stabilization vacuum. The adjustable speed blower was set to run at a speed that was just sufficient to keep up with the plenum and connection hose leak rates. This could cause problems, if unexpected changes in the system leak rate occurred, resulting in over or under vacuum. Since the focus of the dish was affected by the vacuum level, this could also affect the system performance without giving any signal to the operating controller. The new design uses a vacuum-sensing transducer to supply a feedback signal to the blower-speed controller to maintain a constant vacuum level.

9.3 Design Details

There were several lessons learned from the 7-m prototype experience that led to an improved design for the 10.4-m dish. Mostly, only small changes are involved although some result in marked improvements in the reliability and manufacturability of the newer design. The shop welding and field machining of the departure bar is one major design improvement discussed earlier.

9.3.1 Central Drain

The central drain detail on the 7-m prototype had a small concentric gap between the I.D. of the membranes and the hub O.D. This gap was the path for water drainage from the dish,

which stowed face up. Debris tended to collect at this low point and clog the drain holes leading out through the rear of the hub. This gap was too small to permit easy cleaning. The 10.4-m dish will not stow face up, so less demands will be placed on the drain. The gap between the membranes and the hub is increased 2 inches on the to facilitate cleaning. The gap will be covered with a removable grating to prevent the entry of debris.

9.3.2 Central Seal

The 7-m prototype central-membrane seals connected the space between the polymer and metal membranes to the main plenum. When the main plenum was evacuated, the space polymer-to-metal was also evacuated. When vacuum was reduced, the plenum filled first and then the polymer-to-metal space. This causes a problem in that the polymer membrane tends to draw the metal membrane out of shape as the vacuum behind the metal is reduced. A third problem occurred when the polymer membrane failed causing a large vacuum leak that bled off all stabilization vacuum. The new 10.4-m design permits the main plenum to be evacuated independently of the polymer-to-metal space. This means that if the polymer membrane fails, the stabilization vacuum on the metal membrane will not be lost. The new design also provides for the polymer-to-metal space to be positively pressurized independently of the main plenum to aid in separation of the front membranes for shut downs and/or servicing.

9.3.3 Rear-Spoke Springs

The rear-spoke spring gap element on the 7-m prototype was designed to permit simple adjustment of the spring pretension and the gap dimension without disassembly. The new design is a much simpler assembly because the relationships defining the required spring pretension and gap have been established and no adjustment after assembly is required.

9.3.4 Spoke-to-Hub Attachment

The 7-m diameter optical-element hub had large flanges at both ends for the spoke attachment. These flanges required extensive machining. Each spoke also required a machined stub to interface the flange to the spoke-clevis termination. The cost of these components is eliminated in the 10.4-m design. The spokes bolt directly to the hub as described in Section 7. There is a simple reinforcing band welded to the hub where the spoke-bolt holes penetrate to reduce local stresses. This change was accomplished by slightly rotating the points of attachment of the spokes at the hub end relative to their ring end to keep the spokes tangent to the hub. Also, the larger circumference hub provided more room for adjacent spoke ends such that they did not interfere.

9.3.5 Vacuum Blowers

The 7-m prototype used two identical blowers plumbed in parallel. This approach is also used on the 10.4-m design to provide redundancy for increased reliability. The new design also includes check valves at each blower so that, if a single blower fails, air will not leak and reduce the dish performance. The valves also permit replacement of one blower at a time without deactivating the stabilization vacuum.

9.3.6 PCA-Strut Attachment

The PCA struts on the 7-m prototype terminated at the ring end with rod ends threaded into the struts. This permitted adjustment of the effective strut length. It was necessary to unpin the rod end from the mounting bracket and the entire PCA support tripod tilted to accomplish this, however. The new design uses a turnbuckle-type arrangement with an intermediate, threaded part having right-hand outside threads and left-hand inside threads. The PCA support can be adjusted after it is pinned for a safer and more convenient installation.

9.3.7 Successful Details

Successful demonstration of various design details on the 7-m prototype dish was as important as defining needed dish improvements. What were simply design concepts when the 7-m dish was built can now be used again with confidence on the current and future designs. Some of these successes are as follows:

a. Polymer membrane perimeter clamping with "O" ring cord to avoid sharp line contact and assure good grip within an assembly;
b. Rear-membrane perimeter clamping using a simple channel to capture a sewn-in-hem rope. The channel transferred membrane tension loads to a simple rail. The assembly required no close tolerances and no critical bolting;
c. Indirect resistance welding of the formed metal membrane to the departure bar for fixturing during assembly;
d. Use of a departure bar with a sloped surface to match the membrane slope to achieve fixing of the metal and reflective membrane to the ring; and
e. Adjustable length PCA support struts to facilitate assembly.

9.4 Supporting Work by Others

Outside of Solar Kinetics, significant progress has been made in understanding dish concentrators further. Results of some of this work were used to define specifications for the current design and to check performance estimates made at SKI. Work done at SNL and at NREL (formerly SERI) has included modeling of receivers and reflective

concentrators. SNL's code, CIRCE, was used to estimate net energy supplied to the engine considering concentrator losses, receiver losses, and collector geometry. NREL's codes DISH and OPTDISH are referenced in Section 6. These were used to predict changes in reflector contour resulting from optical-element-ring deflections. Net energy delivered to the receiver was calculated for suspected worst case loading conditions.

10.0 7-M Reflective Membrane Replacement

Reflective polymer-membrane materials have not yet been demonstrated to have a service life equal to that of a solar concentrator structure. The 10.4-m design permits replacement of the reflective membrane to accommodate replacement during the lifetime of the dish. This section will describe work done to develop and demonstrate a technique for reflective film replacement.

10.1 Materials

The current benchmark for solar concentrator reflective surfaces is conventional glass mirrors, which may last up to 25 or more years. Some polymer reflectors have remained serviceable for 7 or more years where the film was adhered to a rigid metal substrate and not subjected to significant strain. Significant problems have been experienced with unsupported all-polymer reflective stretched-membranes even with relatively low strain levels. Ongoing development in this area by other solar companies shows continued improvement.

The current stretched-membrane dish design varies significantly from the applications mentioned above. This design does not attach the rear of the film to a metal surface, and it does impose significant strain in the film. It also uses a front-surface reflective film with no additional polymer film laminated to the back for reinforcement.

The selected reflective membrane uses two separate layers, a clear protective FEP Teflon (TM) membrane on top of a front-surface metalized (silver) PET film with a protective acrylic wash coat on top. The clear Teflon film is 0.05-mm thick and 95% transmissive. The reflective film is 3-M's Silverlux product that uses a 0.004-mm thick PET film.

Investigations at SKI, SNL, and NREL suggest that a common initiator of silver metallized acrylic film degradation has been moisture encroachment from unsealed edges or locally damaged areas. These observations were made on rear- surface metallized films glued to rigid substrates. This effort sought a way to prevent moisture from coming in contact with the metallization. A multi-layer polymer film was conceptualized with a transparent, weather resistant, and ultraviolet tolerant film outermost to serve as a moisture barrier and main structural film. The rear side of this would be metallized, preferably using silver for its high solar spectrum reflectivity. Behind the silver, another layer is necessary to isolate the silver from any moisture. This could be accomplished in two ways. Another polymer layer, either a coating or another film, is one means. Since many polymers are degraded by ultraviolet light and thin metallizations of silver have a window in their transmissivity in the ultraviolet range, an additional layer of metallization behind the silver was conceptualized to protect the rear most polymer layer. Multilayer-metallized-polymer films are produced today for specialized applications, many in the aerospace industry. Additional development may show that a metal layer alone is sufficient to protect the silver.

For the current work, funds were not available to fabricate a custom film, nor was this the thrust of this program. The approach selected was to use commercially available films to approximate the desired film. The activities associated with fabricating and installing this film would yield valuable lessons in the limitations and techniques required for field reflective film replacement.

Films considered for the outermost layer included Teflon, acrylic, polycarbonate, and Tefzel. Teflon was selected for its unique combination of high transmissivity, low moisture permeation, tolerance to ultraviolet light, and low elastic modulus. The latter property was significant for the double film approach because the stabilization vacuum would be used to pull the film down against the formed metal membrane. If the polymer membrane was too stiff, an increased vacuum would be required, which also raises the loads on the optical element components. Available metallized films all used polyester or acrylic substrates with relatively high moduli. Adding an additional high-modulus layer would require excessive vacuum for the 7-m structure.

Another important aspect of material selection was the ability of the film to be seamed. Film is not generally available in the widths required for an entire membrane and must, therefore, be fabricated to form a complete membrane. Small quantities of wide films are difficult to obtain. Past experience with joining polyester film for the original 7-m reflective membrane showed bond strengths equal to the parent material strength. Earlier testing of acrylic bonding never achieved adequate seam strength. In the current effort, ultrasonic welding of acrylic and polyester-metallized films to themselves was tried. Bond strengths were not acceptable. The selected method was the same as used on the original 7-m membrane and is described fully in Section 7.

Both the Teflon manufacturer and third party processors indicated very good bondability with the Teflon film using thermal welding. The low material modulus resulted in low tensions, further reducing the required bond strength. Samples supplied by vendors and tests performed at SKI confirmed the bondability.

The reflective film selected was SA95 because it was adequate and it was available. The 3M Company would accept a reasonable minimum order quantity without any special setup charge. This product is usually manufactured with a pressure-sensitive adhesive and a release liner on its back side. Material with no adhesive was obtained for this work. An existing manufacturer of concentrating trough solar collectors reports acceptable life of this film when used outdoors.

Concerns for the integrity of the protective coating on the silver existed even after the Silverlux selection. The film was not designed for this application. Installation of the membrane requires stretching the film approximately 2 percent. Microscopic observations of stretched film were inconclusive as to the effects of stretching effect on the coating integrity.

The Teflon membrane was to be manufactured by a third party experienced in that area. This company advised SKI that there would be some local material shrinkage along the seam resulting from the heating of the material during seaming. This was anticipated to be of little consequence because the material modulus is so low that the material could be readily stretched during installation. However, one seam would have to be completed in the field at the time of installation. This would require a different apparatus than the shop assembled seams used, although the loads on the field seam would be the same as on the main body of the membrane. In addition to this field seam, a reinforcing ring was added to the center of the membrane where the hole for the optical-element hub would be. Some significant shrinkage occurred there.

10.2 Membrane Fabrication

10.2.1 Transparent Top Membrane

The Teflon membrane was fabricated by a custom fabricator specializing in Teflon processing. The 0.05-mm thick film was overlapped approximately 13-mm. An impulse heat sealer was used to thermally bond the material to itself under controlled pressure, temperature and dwell time, followed by a cooling period while still clamped. The machine configuration was similar to a sewing machine to achieve continuous feeding of material through the heat sealing belts. The bond width is approximately 6-mm wide. Tensile testing proved its strength equal to that of the parent material.

A large area is required to fabricate the 7.6-m square membrane. As each strip of material was added, the new area of the membrane was rolled onto a mandrel parallel to the seam. This mandrel was small enough in diameter to pass through the throat of the impulse heat-sealer. This part of the operation went well and would require minimal process changes for future work. The work area was kept as dust-free as practical to keep the membranes clean. A method to improve cleanliness is discussed in the reflective-membrane fabrication description.

The membrane was successfully shipped by common carrier wrapped on a 100-mm diameter aluminum tube supported at each end concentrically within another 152-mm diameter tube. A sheath of polyethylene protected the Teflon from dust and abrasion. A wrap of bubble cushioning material prevented the Teflon from being pinched against the inside of the outer tube during any rough handling.

The center reinforcing rings were added at SKI. A manual heat-sealer was used for this purpose. The fixture provided a controlled temperature, clamping pressure, and dwell time. Each heat bonding cycle was followed by a cooling period when a metal heat sink was clamped against the freshly bonded area. Temperature, pressure, dwell time, heating and cooling dwell periods were varied to achieve the best bond with the least shrinkage. The fixture was not large enough to bond the entire reinforcing ring at once. The bond was made step-wise using a radially oriented heated shoe. Problems were encountered where the pressure was uneven

across the shoe such that one edge tended to press harder and cause a thinning of the membrane along that line. The fixture and the procedure was modified to minimize this effect. After installation, a rip initiated in the Teflon membrane possibly from one of these weakened areas in combination with stresses resulting from handling difficulties. The rip was approximately three inches long and it did not propagate. Future operations should use a suitable single-piece heated shoe to eliminate these edge effects.

The shrinkage, which occurred from the reinforcing ring bond, caused additional initial stress in the membrane immediately after installation. As the membrane was drawn down, the material yielded to relieve these stresses. This is probably not a major problem area for future membranes.

10.2.2 Reflective Membrane

The reflective membrane was fabricated at SKI. A temperature-controlled heated shoe was used to activate the thermoplastic adhesive. Heat was applied to the back side of the transverse tape with the membrane material reflective side down against a copper back-up bar covered with 3.2-mm neoprene tape protected by a woven Teflon tape. An impulse heat-sealer, such as used on the Teflon membrane, would give more consistent results and would be much faster for future membrane fabrication. The width of the heat element would need to be the same as the width of adhesive, 25-mm for this membrane.

The reflective film was supplied with a peal-off protective film on the reflective side to prevent damage from handling prior to installation. This liner was removed along each edge of the film where the heat effected zone from the adhesive activation would be. After the reflective membrane was completed, it was rolled onto a shipping mandrel along with the protective transparent membrane. The main body of the protective liner was removed during this operation. Removing the narrow strip of liner prior to the seaming operation was too labor intensive. The membrane was rolled from one mandrel to another several times in order to fabricate it reflective side down, gain access for center hole cutting and reinforcing, interleave it with the transparent membrane, and field install it from a mandrel with the reflective side facing correctly. This handling should be reduced for future membranes to reduce risk of accidental damage, abrasion of the reflective surface, and exposure to dust and dirt.

To reduce the buildup of static charge on the plastic film, and therefore, reduce dust attraction, an ionized air blower was used. The discharge of the blower was directed along the film during fabrication and handling. The blower volume and velocity was insufficient to cover the entire membrane from a single point, so the blower was moved as necessary to reduce the static charge on the entire membrane. This technique was effective and would be used again on future membranes.

The apparatus will be shrouded by a curtain of filtered and ionized air to keep the film clean. The release liner will be removed entirely just prior to seaming. The apparatus will feed the

adhesive and transverse fiber tape to reduce setup labor. After each reflective panel is added, the membrane will be wound onto a shipping mandrel simultaneously with the transparent membrane to reduce handling.

10.3 Field Installation

The replacement membrane was fabricated, as was the original membrane, in a conic shape. This reduced the degree of strain the membrane would experience as it was drawn by the stabilization vacuum down to the formed metal membrane. The cone depth was 85% of the total formed-membrane center depth. The replacement membrane was fabricated with one radial seam uncompleted, so the membrane could be installed around the central hub with the optical element fully assembled. The seam would be sealed after the membrane was in its final position. The original membranes were installed during initial dish assembly before the front spokes and central hub were installed. The membrane replacement work was planned to take place with the optical element supported in its normal fashion on the dish drive while the original installation occurred in ground level assembly tooling in the assembly building.

Placement of the new membrane was accomplished by rolling half of the membrane on one mandrel and the other half on a second mandrel. Each mandrel was being rolled parallel to the uncompleted seam until they met in the center. Each mandrel was supported from a rope at one end so that they hung vertically. With the dish facing the horizon, the mandrels where hoisted high enough that their bottom end cleared the dish's hub. They were then positioned such that they could be lowered with one mandrel on either side of the hub, the hub passing through the gap where the seam was not completed. When the hub was centered in the pre-cut hole in the membrane, one mandrel at a time was unrolled, and the periphery of the membrane temporarily secured to the optical-element ring as it was payed off. This operation was complicated by the presence of the front spokes. To permit the mandrel to be rolled outwards away from the hub, it was built with a telescoping extension at the bottom end. The upper end of the mandrel was shorter than the material wound upon it and simply hung from a rope. As the mandrel was rolled away from the hub, the support rope was passed manually past each upper spoke by workers on an adjacent boom lift. The lower extension was lifted, by a worker on the ground, up over each spoke. This system was arguably acceptable for a prototypical operation. It was very labor intensive in preparation and implementation, and fraught with difficulties and potential risks to the membrane. Successful operation was dependent on very calm winds. Four workers were required and two personnel boom lifts. The operation was planned successfully to avoid any pe sonnel risk. There were, however, several possibilities for errors in handling which could, result in serious damage to the new membrane or to the existing formed metal membrane. Later discussions will describe how this procedure can be replaced with a less time consuming and risky one.

To complete the last radial seam of the replacement membrane required installation of a temporary radial beam to be installed in the ring plane of the dish, directly in line with the seam. This beam would serve as a back-up bar for the reflective membrane adhesive activation

and for the Teflon membrane thermal bonding. The beam would initially be installed attached to the hub at one end and supported on the optical-element ring at the other end.

A length of transverse fiber tape and adhesive was fixtured to the bar with low-tack tape. The reflective membrane seam was closed a short length at a time and a temperature-controlled heated shoe was positioned to activate the adhesive. The heated shoe was held in place by an air cylinder to assure correct clamping pressure. The air cylinder reacted against a second beam also aligned with the seam, but on the front side of the membrane. This seaming operation differed slightly from the shop fabrication in that the heat was applied from the front side of the membrane. This made checking the seam integrity more difficult because the wetting of the thermoplastic adhesive could not be observed through the silver. The reflective film did not permit this.

During the previous operation, the Teflon membrane was folded back on either side of the seam to provide working room. To seal the Teflon membrane, the back-up bar was withdrawn from its first position and reinstalled at the same radial location in front of the now complete reflective membrane. The Teflon seaming proceeded using the same apparatus with different temperature, clamp force, and dwell time settings.

In addition to completing the radial seams in the main body of each membrane, the reinforcing rings at the center had to be seamed. This was complicated by their multi-layer construction. A single seam would have caused a weak point and rendered pointless the existing reinforcement. Each seam in the reinforced area was overlapped to retain the doubling effect over 360 degrees. This was done immediately before each radial seam was begun. Working space and access to this center area was quite limited. In some areas, a backing surface was held in place manually and a hand-held heated shoe used in place of the normal tooling because of limited access.

During the entire field operation, a fitted canvas cover was placed over the front spokes. The dish was oriented to face the horizon with a temporary scaffold positioned at the bottom center reaching up to the hub. The uncompleted seams were also at this "six o'clock" position. A large radial seam in the cover could be folded back to allow access to the seaming area. The cover had sufficient extra material to permit it to be wrapped around the entire scaffold to provide extra shelter for the seaming operation.

The cover not withstanding, the wind caused considerable inconvenience to the installation and seaming operations. Even light winds readily move the very thin membrane material disturbing fixturing at the seam or confounding careful manual handling operations. It was difficult to avoid flagging and local creasing of the membrane material. Likewise, it was difficult to keep the perimeters of the membranes (polymer and metal) tightly together as was proposed to eliminate dirt from entering.

10.4 Lessons Learned From Field Experience

The membrane replacement operation took over two weeks in the field. Some of this time was spent solving typical on-site problems that inevitably arise when specialized equipment is setup in the field for the first time. Several weather-related delays occurred when it was too windy to work with the membrane material outdoors or the wind was great enough to require stowing the dish and clearing the area per site operational procedures. The selected approach required too much on-site labor and was too sensitive to weather conditions. It would not be appropriate for replacing the reflective surface on a commercial dish because of unacceptably high cost and risk.

That a membrane can be replaced was demonstrated. That a new membrane will smoothly pull down and assume the formed metal-membrane contour was demonstrated. A seam failure in the reflective membrane occurred shortly after installation. This was most probably due to a lapse in proper adhesive joint preparation and or adhesive activation procedures. SKI has had very good reliability with this adhesive system in the past.

Two major assumptions originally made in planning membrane replacement need to be re-evaluated. The first is that the optical element should remain on the drive. The second is that the front spokes should not be removed.

If the optical element were removed from the drive, most work could be done from an easily erected 1.4-m scaffold with greatly improved efficiency. Much time is lost in getting to and from working positions with man-lifts and tall scaffolds. Working at height requires appropriately greater deliberation of movement, and often requires one worker to be idle while waiting for the other. Working at height often requires one worker to perform a task that typically would require two workers. If the optical element were lowered to the ground, it may be practical to erect a tent or sprung-structure supported fabric building over it to prevent weather related delays and difficulties.

If the front spokes are not an obstacle, the polymer membranes could be completed 100% in a factory setting. This would permit better process control, use of less expensive labor, use of fewer total labor hours. The membranes may require an innovative means for shipping since a conic shape will not roll on a simple cylindrical mandrel without some folds. This should be a surmountable problem given that membranes formed to a parabolic shape can be rolled onto custom contoured mandrels.

Experience with the original assembly of the optical element suggests that removing all the front spokes may permit the ring to distort either radially or in planarity. When the spokes were originally tensioned, the ring concentricity and planarity were monitored and modified through several iterations of spoke tensioning. It was found that the final shape of the ring was path dependent varying with the order and degree of spoke tightening. An alternative to removing all the front spokes at once is to remove one spoke at a time. The polymer membrane

would be slipped over each spoke, which would then be re-connected and re-tensioned. Subsequently, the next spoke would be removed, etc. In this way the ring never sees a significant difference in external loads. To assure the final state is the same as the initial state, each spoke tension would be measured immediately prior to its removal and again during retensioning.

A suitable ultrasonic method of bolt tension determination is now commercially available. A transponder is attached to one free end of a bolt or spoke for the 7-m prototype. Sound waves are transferred into the spoke that are reflected back from the far end of the bolt. The time required for the reflection to return indicates the bolt length. As the bolt is tightened and stretched, this time interval increases giving a measurement of bolt tension.

To support a continuing manufacturing operation for stretched-membrane dishes, some investment in capital equipment would be required. In addition to the factory equipment, a set of mobile equipment for membrane replacement efforts is required. This equipment would all be designed to fit in a single ISO container or conventional semi-trailer. The only additional equipment required would be a locally obtained crane.

The replacement membrane manufacturing operation will require no changes from the original equipment membranes, so the same production equipment will used.

A fixture for supporting the optical element at ground level will be fabricated. It will stabilize the optical element with support points on the ring as well as at the rear of the hub for increased stability on uneven ground. It will not use the main bearings as supports, but will adapt to the rear hub and moment arm weldment directly. This will permit inspection and replacement of the pivot bearings while the optical element is dismounted.

Quick setup staging to create a circular access platform around the ring will be included. The deck height will be approximately 1.4-m above ground level. A four-wheel, self-propelled, boom type man-lift will be included in the equipment for accessing the front of the hub when the optical element is facing up in its fixture. An inclined cantilevered ladder will be included to provide worker access to the membrane center when the optical element is mounted on the drive. This will be necessary for servicing and securing the central seal components. The scaffold used for the prototype operation was too time consuming to set up and did not allow easy access to the central seal area. It could be adjusted vertically, but could not be moved horizontally enough to get close to the membrane center.

A temporary vacuum source and control system will be part of the field equipment. It will allow quick switch-over to the moveable vacuum source so the optical element will have stabilization vacuum during its removal and servicing, if required. This will also permit the dish vacuum system to be conveniently checked and serviced while the dish is removed.

The field equipment will include a three-point spreader for lifting the dish. It will have a lifting eye for crane attachment. The spreader arms will position chains to clear the PCA and attach to a lifting bracket on the front of the hub. The PCA would remain in place. The local crane will not have to supply any additional hardware.

The equipment will also include a sprung-arch, supported-fabric enclosure to provide shelter from wind and precipitation during the membrane replacement. No additional equipment is required to assemble this structure beyond hand tools and possibly the boom lift.

A proposed site-work schedule is shown in Table 10.1. This presumes a minimum of three workers plus the crane operator when required. Actual crane time would be about 5 hours for a routine operation where the dish is serviced adjacent to the support pylon. A larger crew would reduce the total duration of the operation and would permit more simultaneous servicing of the rest of the dish systems. If more than one dish were at a single sight, additional efficiencies could also be expected.

Table 10.1 Proposed Schedule for Routine Membrane Replacement.

Day 1

Arrive on site.
Break out equipment from container.
Inspect dish.
Position fixture for dish support.
Erect access scaffolding around optical-element support fixture.
Attach temporary vacuum source to optical element.
Position cantilever ladder and remove appropriate central seal components.

Day 2

Position crane.
Rig optical element for lifting.
Set optical element in support fixture.
Erect sprung-arch, fabric-support shelter.
Remove old reflective membrane.

Day 3

Clean formed metal membrane.
Remove clamp bars.
Deploy new membrane over optical element, outside front spokes.
Measure existing front-spoke tensions.

Day 4

Install membranes by sequential removal of front spokes.
Clamp membrane periphery to optical-element ring.

Day 5

Complete membrane installation
Remove sprung-arch, fabric-support shelter.
Set optical element back onto drive.

Day 6

Complete rear-seal component installation.
Reconnect permanent vacuum control.
Check dish performance.
Pack equipment into container.

This plan is most suitable for dishes not located in extremely remote areas. Where cranes are unavailable or very expensive to mobilize, the extra effort of performing the work with the optical element supported on the drive would be justifiable. A temporary ring support could be installed to reduce and make more uniform the spoke loads during their individual removal while fitting the new membrane. Since both membranes are complete and shipped rolled together, they will be easier to handle and there will be less opportunity for dirt to get between the membranes. Since no time will be required to seam the membranes, their exposure to wind damage during installation will also be reduced.

10.5 Summary of Film Replacement

The membrane replacement effort was very informative, while not an unqualified success. Handling problems concerning light membranes, even in light winds, were underestimated. Experience demonstrated that insufficient time was devoted to optimizing the field seaming apparatus. It was also realized that this process would retain some risks and expense even at its best, due to the need for extensive field work over or near the formed metal membrane.

Shipping 100% complete membranes to the field was recognized as being preferable to splitting the membrane fabrication into two operations. More mechanical work would be required on site in sequentially removing and replacing the spokes. This is judged to be a more appropriate field task, however, than bonding the polymer membranes. It should also shorten the total time the polymer membranes are unsecured and exposed to potential damage.

Re-examination of the option of removing the dish from the drive suggests that with an experienced crew and appropriate equipment, this could be done efficiently. This option would be selected in the future.

An important accomplishment is the demonstration that a dual-layer membrane can be drawn down to the formed metal membrane free of wrinkles or air pockets. It is also significant that all the membrane seals can be effectively reestablished. It remains to be seen if the transparent membrane reduces weather related degradation of the reflective membrane.

Figure 10.1 shows the 7-m prototype with the new reflective membrane fully installed. The smooth, continuous lines of images reflected by the mirror suggests that the metal membrane is quite rugged. Only minor damage was apparent from several months without stabilization pressure.

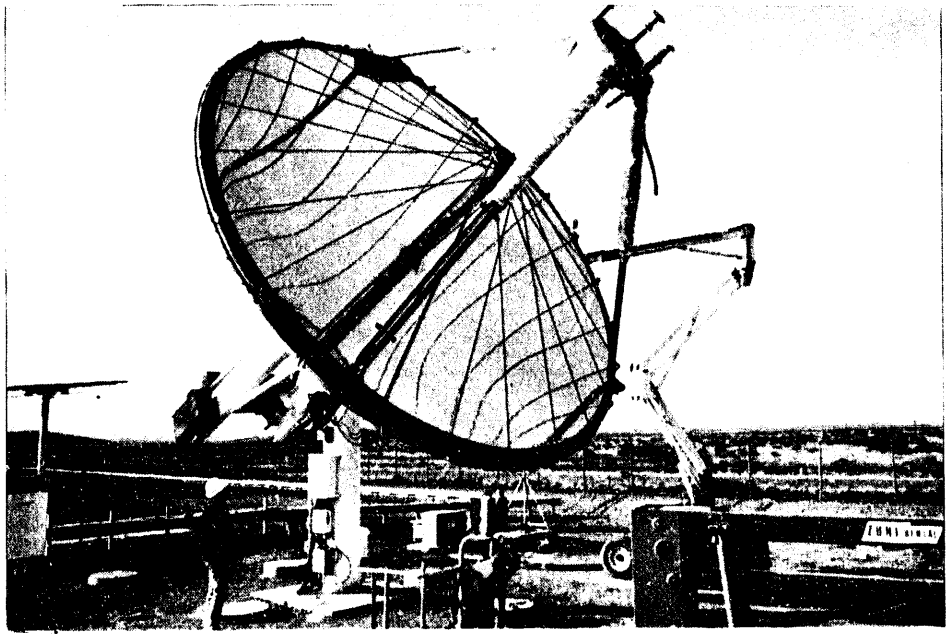

Figure 10.1 New Reflective Film Installed on Existing 7-m Prototype.

11.0 Summary

A 10.4-m concentrating solar collector system utilizing stretched-membrane technology has been designed. The design is based on considerable investigation, experimentation, and experience from researchers and engineers in the solar industry, telecommunications industry and United States national laboratories. The design philosophy was based on commercial production and sales.

The philosophy of design has been to use conservative estimates of loads and stresses. Safety factors from the AISC code are used throughout as minimum values. Greater factors are used on all welds and on components whose loading is less well defined. Wind load estimates are based on data that has been used extensively for successful design of antenna structures in the telecommunications field.

The materials selected are readily available from commercial sources with the exception of long-life reflective film. Almost all other materials and components are available from multiple manufacturers. The materials specified are robust and used in a manner consistent with common industrial practices.

The purchased components such as actuators, controls, motors, etc. are also common commercial items. One exception to this is the tracking controller that is currently being manufactured by only one firm. This controller design may be licensed very reasonably from the Department of Energy's Sandia National Laboratories. The azimuth drive is also a sole source component. High-stiffness, high-precision, high-torque rotating platforms are not unavailable from or unfamiliar to a number of other competent manufacturers, should a need arise. Other purchased components were selected specifically for their availability, as well as their cost-effectiveness for the application.

The unique nature of stretched-membrane technology means that some special fabricating techniques are required, particularly for membrane forming and handling. Membrane forming was the subject of considerable earlier successful efforts in this program. The balance of the structure, however, applies conventional metal working techniques such as casting, machining, shearing, bending, heat treating, and welding to the unique membrane support structure.

The use of proven materials, components, and manufacturing processes will reduce the cost required to field prototype and early market concentrator systems. Equally important, it

The use of proven materials, components, and manufacturing processes will reduce the cost required to field prototype and early market concentrator systems. Equally important, it will ease the task of selling these units to customers appropriately cautious about investing in a new technology.

An equally important component for successful sales of this technology is performance. Results of performance testing of the 7-m prototype optical element demonstrate very good optical performance. Measurements of the flux distribution profile at the focal point combined with sophisticated computer models of receiver and engine performance indicate that the dish will integrate very well with receivers and engines currently under development and testing. From a performance perspective, this concept scales to larger sizes very readily.

Long-term as well as initial performance is critical to the solar collector systems' marketability. This means that reliability is very important. Reliability is a function of design, materials, and fabrication techniques. The detailed design of the concentrating collector and its support system has been carefully considered and analyzed. Reliability of the structure is not expected to be a problem.

A more fundamental question is the inherent reliability of the stretched-membrane concept. There are two main issues that affect the reliability of this design concept. One is the vulnerablities of the metal membrane to environmental hazards such as wind blown debris and hail and to loss of vacuum. The second issue is associated with the potential for developing an acceptably long lasting reflective polymer membrane. Alternately, is some other reflective surface applicable to this approach such as mirrored micro-glass.

Only experience with large-scale optical elements exposed to true operating environments will unequivocally answer the first question. The existing 7-m optical element is an excellent tool for initial investigation of this issue. Thorough measurement and analysis of its flux distribution was made when it was new. Now that it has had extended exposure to the weather, these measurements should be made again and compared. The unit has spent considerable time with inadequate stabilization vacuum, and on at least one occasion had excessive rain accumulation on the formed membrane when a drain was not working. Current performance data would be very valuable in determining how robust this design is. An argument could be made that these occurrences were prototypical and would never happen to a more serviceable design incorporated in a properly attended power/profit producing energy collection system. However, they do represent two realistic situations future dishes could experience. When available, larger optical elements should also be exposed to unusual extreme operating conditions to determine their sensitivity to such conditions.

The issue of acceptable reflective surface materials needs to be addressed through further investigation and development. Some work on reflective polymer films is currently being funded by the Department of Energy through NREL. This work is not specifically aimed at films for stretched-membrane dishes. It is likely that more work will be required with considerable investment of money and time to demonstrate the performance, longevity, and manufacturability of acceptable materials.

The stretched-membrane concentrator concept offers excellent optical performance very well matched to a variety of receiver and engine designs. The design is readily scalable to a wide range of sizes. Costs to manufacture the dish are not prohibitive at the important low, early market volumes. Costs to set up manufacturing are also reasonable. No technical barriers to manufacturing have been identified.

12.0 References

1. Development of a Stretched-Membrane Dish-Phase I, SAND88-7035 (Solar Kinetics, Inc., Dallas, Texas), Albuquerque, NM:Sandia National Laboratories, March 1989.

2. Development of a Stretched-Membrane Dish, SAND88-7031, (Solar Kinetics, Inc., Dallas, Texas), Albuquerque, NM: Sandia National Laboratories, October 1989.

3. J. W. Grossman, R. M. Houser, W. W. Erdman, Testing of the Single-Element Stretched-Membrane Dish, SAND91-2203, Albuquerque, NM: Sandia National Laboratories, February 1992.

4. W. H. Heller, Joseph S. Peters, Development of a Low-Cost Drive Mechanism for Solar Heliostat, Final Report, SAND90-5753, Albuquerque, NM: Sandia National Laboratories, February 1989.

5. V. R. Goldberg, John L. Ford, Arnold E. Anderson, Design of the Support Structure, Drive Pedestal, and Controls for a Solar Concentrator, SAND91-7007, Albuquerque, NM: Sandia National Laboratories, August 1991.

6. A. B. Maish, The Solartrak Solar Array Tracking Controller, SAND90-1471, Albuquerque, NM: Sandia National Laboratories, July 1991.

7. .J. A. Peterka, Z. Tan, B. Bienkiewicz, and J. E. Cermak, Wind Loads on Heliostats and Parabolic Dish Collectors, Final Subcontract Report, SERI/STR-253-3431, Golden, CO: Solar Energy Research Institute, November 1988.

8. "Final R&D Report on Wind Loading of Parabolic Antenna," Report #G3712.18.01A, January 10, 1972.

9. A. Anderson, P.E., "Wind Load Report for SKI 13-Meter Facet," December 27, 1990.

10 .Design and Cost of the First Commercial Stretched-Membrane Heliostat, SAND90-7038 (Solar Kinetics, Inc., Dallas, Texas), Albuquerque, NM: Sandia National Laboratories, July 1991.

11. K. Beninga, R. Davenport, and J. Sandubrae, Selection and Design of a Stretched-Membrane Heliostat for Today's Markets, SAND89-7040, Albuquerque, NM: Sandia National Laboratories, January 1990.

12. V. R. Goldberg and J. W. Anderson, "Final Report, SKI SMD Pylon and Foundation, Doc. #WGA/062992-01, July 7, 1992.

13. W. C. Young, Roark's Formulas for Stress and Strain, 6th ed., New York: McGraw-Hill, 1989.

14. Manual of Steel Construction, 8th ed., Chicago: American Institute of Steel Construction, Inc., 1980.

15. Sergent, Hauskins, and Beckwith, "Report on Soil Conditions at SNLA," #E83-1179, December 7, 1993.

16. C. L. Mavis, 10 MWe Solar Thermal Central Receiver Pilot Plant Heliostat and Beam Characterization System Evaluation, SAND 87-8003, Albuquerque, NM: Sandia National Laboratories, December 1986.

17. "PCA Structural Support Design and Analysis," HLA Engineers, Inc., October 29, 1991.

18. L. D. Jaffe, Optimization of Dish Solar Collectors With and Without Secondary Concentrators, DOE/JPL-1060-57, Pasadena, CA: Jet Propulsion Laboratory, May 15, 1982.

19. A. C. Ratzel, et. al., CIRCE: A Computer Code for the Analysis of Point-Focus Solar Concentrators, Solar Engineering Proceedings - 1987, Vol. 1., pp. 136-145.

20. T. R. Mancini, "Optical and Thermal Performance of a Faceted, Stretched-Membrane Dish Concentrator," Rough Draft, Albuquerque, NM: Sandia National Laboratories, December 1989.

21. Development of a Stretched-Membrane Dish, Phase II, Task 2, Topical Report, SAND90-7036 (Solar Kinetics, Inc., Dallas, Texas), Albuquerque, NM: Sandia National Laboratories, July 1991.

22. C. Kutscher, Solar Energy Research Institute, "Calculation of Rear Cable Deflection for Dish," inter-office memorandum, September 11, 1987.

23. S. P. Timoshenko, Theory of Elastic Stability, 2nd ed., New York: McGraw-Hill, 1988.

24. L. M. Murphy, Moderate Axisymmetric Deformations of Optical Membrane Surfaces, SERI/TP-253-3020, Golden, CO: Solar Energy Research Institute, February 1987.

25. ANSYS User's Manual, Revision 4.3A4, Swanson Analysis Systems, Inc., December 1, 1988.

26. C. R. Steele, C. D. Balch, et al., Membrane Dish Analysis: A Summary of Structural and Optical Analysis Capabilities, NREL/TP-253-3432, Golden, CO: National Renewable Energy Laboratory, November 1991.

27. T. Wendelin, National Renewable Energy Laboratory, personal correspondence to Paul Schertz, Solar Kinetics, Inc.

28. Personal correspondence from Gary Jorgensen (NREL) to Paul Schertz (SKI).

APPENDIX A
Wind Tunnel Data Application

The methods listed here were used to convert the forces and moments predicted in the wind loading consultant's data files to other similar dishes. The methods will accommodate differing diameters and wind speeds. All forces and moments used were about a point in the center of the dish face.

Subscript 1 = source data

Subscript 2 = new data

Force = force exerted by wind on dish in direction indicated.
Area = total dish projected area exposed to wind.
Wind Speed = wind speed in azimuth direction.
Moment = moment about axis of interest.
Dia. = gross outside diameter of dish.

$$\text{Force}_1 * \frac{(\text{Area}_2)}{(\text{Area}_1)} * \frac{(\text{Wind Speed}_2\ \hat{}2)}{(\text{Wind Speed}_1\ \hat{}2)} = \text{Force}_2$$

$$\text{Moment}_1 * \frac{(\text{Area}_2)}{(\text{Area}_1)} * \frac{(\text{Wind Speed}_2\ \hat{}2)}{(\text{Wind Speed}_1\ \hat{}2)} * \frac{(\text{Diam}_2)}{(\text{Diam}_1)} = \text{Force}_2$$

For the data as reported from the consultant and for the final dish design, the conversion factors are as follows:

D_1	=	511.68"
D_2	=	409.5"
Area_1	=	1,427 sq.ft.
Area_2	=	915 sq.ft.
Wind Speed_1	=	20 mph

Final design at 50 mph.

$F_1 * 4.251 = F_2$
$M_1 * 3.506 = M_2$

Final design at 90 mph

$F_1 * 13.774 = F_2$
$M_1 * 11.360 = M_2$

These formulas are used in the SKI Lotus model "DRVLOAD.WK1"& "PYLONA.WK1".

APPENDIX B
Load Determination for Drive

The methods described here were used to translate the forces and moments reported by the wind loading consultant to the drive mechanism that supports the dish's optical element. Some reference is required here to the methods described previously in Appendix A for scaling the forces and moments at the dish face.

The scaled lateral forces translate directly from the dish face center to the drive.

Azimuth moments on the drive result from two sources. The moment the wind exert at the dish face are translated directly to the drive axis. Additionally, drag and yaw forces acting at the dish face are acting at some moment arm from the drive azimuth axis. These moments vary with dish orientation and must be separately calculated for each combination of azimuth and elevation angles.

Similarly, the elevation moment has components resulting from drag and lift forces acting through varying moment arms in addition to the wind moment. Gravity forces also contribute to the total elevation moment.

INPUTS

L	=	Elevation axis to ring plane offset
L_{cg}	=	Elevation axis to dish center of gravity offset
W	=	Weight of optical element, PCA and PCA support
EL_n	=	Elevation angle of specific case being considered
AZ_n	=	Azimuth angle of specific case being considered

INTERMEDIATE RESULTS

Gravity moment at EL = 0

M_G	=	$W * L_{cg}$
C_F	=	Coefficient for scaling forces as defined in Appendix A.
C_M	=	Coefficient for scaling moments as defined in Appendix A.

NOTATION

F		=	Force
M		=	Moment
F1		=	Source force value
M1		=	Source moment value
F2		=	Converted force value
M2		=	Converted force value
Subscripts	D	=	Drag
	L	=	Lift
	Y	=	Yaw
	TOT	=	Total
	G	=	Gravity
	n	=	case number
Superscript	′	=	indicates "at drive"

FINAL RESULTS

Forces on drive

$F2'_{Dn} = C_F * F1_{Dn}$

$F2'_{Ln} = C_F * F1_{Ln}$

$F2'_{Yn} = C_F * F1_{Yn}$

Moment converted

$MEL2'_n = C_M * MEL1_n$

$MAZ2'_n = C_M * MAZ1_n$

Moment on drive

$MEL2'_{Dn} = L * F2_{Dn} * SinEL_n * CosAZ_n$

$MEL2'_{Ln} = L * F2_{Ln} * CosEL_n$

$MEL2'_{Gn} = M_G * CosEL_n$

$MEL2'_{TOTn} = MEL2'_n + MEL2'_{Dn} + MEL2'_{Ln} + MEL2'_{Gn}$

$MAZ2'_{Dn} = L * F2_{Dn} * CosEL_n * SinAZ_n$

$MAZ2'_{Yn} = L * F2_{Yn} * CosEL_n * CosAZ_n$

$MAZ2'_{TOTn} = MAZ2_n + MAZ2_{Dn} + MAZ2_{Yn}$

These formulas are used in the SKI Lotus model "DRVLOAD.WK1" & "PYLONA.WK1".

APPENDIX C
Load Determination for Foundation

The methods described here were used to translate the forces and moments reported by the wind loading consultant to the support pylon foundation interface. Some reference is required here to the methods described previously in Appendix A for scaling the forces and moments at the dish face.

The scaled lateral forces translate directly from the dish face center to the drive. Vertical forces are the sum of the lift and the combined optical element, drive, and pylon weight. The azimuth drive moment translates directly to the foundation. Elevation and cross-elevation moments must account for the height from the pylon base to the dish face center. These moments have components resulting from the drag, yaw, and lift forces.

NOTATION

Most notation used in this section is the same as defined in Appendix B.

H		=	height
O		=	offset
MTW		=	twist moment about dish axis
Subscripts	v	=	vertical
	h	=	horizontal
Superscript	′	=	indicates "at drive"
	″	=	indicates "at pylon base"

INTERMEDIATE RESULTS

O_v	=	$L * SinEL_n$
O_h	=	$L * CosEL_n$
H	=	$H_{pylon} + O_v$

FINAL RESULTS

Loads at pylon base.

Elevation base moment

$MEL2''_{Dn}$	=	$H * F2_{Dn}$
$MEL2''_{Ln}$	=	$O_h * F2_{Ln}$
$MEL2''_{TOTn}$	=	$MEL2_n + MEL2''_{Dn} + MEL2''_{Ln} + MEL2'_{Gn}$

Cross-elevation base moment

$MCRS2''_{Yn}$	=	$H * F2_{Yn}$
$MCRS2''_{TOTn}$	=	$MTW2_n + MCRS2''_{Yn}$

These formulas are used in the SKI Lotus model "PYLONA.WK1"

APPENDIX D
SOFTWARE DESIGN TOOLS

DISHECON	Calculates return on investment for ongoing manufacturing and sales operation. Calculates profit, margin, dividends taxes. Input; start-up costs, material costs, labor costs, rates and burdens, inflation, sales volume, depreciation, tax rates, discount rate.
DRVLOAD	Converts wind tunnel data on model to reactions on the optical element drive at the elevation axis. Fixed inputs; wind tunnel model forces and moments. Variable inputs; diameter, weight, C.G. position, wind speed, elevation axis Z position.
EFF	Provides power collection calculation based on the Jaffe model of single-element concentrators and the Mancini model of receiver losses.
FINLRING	Calculate stresses, stress factors and deflections in ring. Inputs; spoke and membrane geometry, spoke initial tension, wind speed/direction, ring cross section, material properties, stabilization vacuum.
FINLWGHT	Weight and center of gravity of optical element, PCA support, PCA and support pylon.
HUB	Calculates actual and allowable stresses and factors of safety. Variable inputs: hub geometry, dish orientation, optical element weights and C.G.s, and spoke tension. Fixed inputs: data from LTV wind tunnel tests and model forces and moments. Intermediate results are used as inputs to model in Engineering Software. The net reaction is the force on the cantilever beam. The compression force from the spokes is multiplied by the predicted deflection to calculate the end moment used in the model.
HUB SHADE	Calculates shading effect of concentrated light by the hub.
JACKLOAD	Determines jackscrew loads and elevation axis bearing loads. Input; elevation axis position, jack screw pivot position, pivot C-C- distance, gravity moment, wind loads, wind velocity, bearing spacing.

PCALEG	Apply AISC code column criteria to PCA leg. Input; compressive load, moment load, strut geometry, cross section, material properties.
PCAREACT	Calculates the loads acting on the ring from a tripod PCA support. Includes effects of gravity and wind. Strut spacing is a variable as well as elevation angle.
PYLONA	Predicts pylon loads from wind load data.
RINGSZ	Provides ring stresses by component. No PCA loads or gravity loads are modeled. Front spoke loads are modeled as point forces which react to prevent free body translation. Rear spoke leads are calculated with same method as SPOKESAG.WKS. Front membrane loads are reaction to pressure. Front or rear wind is allowed. Stresses (and deflections) are calculated based on a location at the midspan between spokes on the top inside corner.
RNGLD	Generates wind loads on the ring for evaluation by finite element analysis. Inputs are in the form of wind induced normal and moment loads. Output provides pill box distribution of wind load including stabilizaiton pressure loads.
SHADOW	Estimates shading by spokes, seams, PCA, and PCA supports.
SPOKESAG	Provides rear spoke deflection and stresses as a function of effective spoke stiffness, initial tension, dish size and geometry. Also provides calculation of front membrane-to-rear spoke clearance.
T4INX	Provides input to CIRCE.
T4OPTX	Manipulates output from CIRCE and combines with Mancini receiver model.
TORSFREQ	Determines natural frequency of optical element and of entire concentrator. Limited to rotational mode about vertical axis with dish facing zenith. Variables include ring weight, ring diameter, number of spokes, hub diameter, drize stiffness, pedestal diameter and more.
XXSCC	Converts finite element output date to a more usable format. It takes as input ring-centroid deflection data. As output, it provides departure point defleciton relative to original location and also relative to a plane defined by the three PCA attachment points.

APPENDIX E

Analysis of dish performance impact due to ring deflection (Case D7) By NREL

Mr. Paul Schertz
Solar Kinetics, Inc.
10635 King William Drive
Dallas, TX 75220

Dear Paul,

This letter along with the enclosed figures and tables document my membrane dish performance analysis of the ring deformation which you modeled using finite element analysis.

In your letter you provided the anticipated performance of the undistorted dish (i.e., a parabola with 2.5 mr slope error and 1.5 mr specularity error). In order to establish this as a baseline, I replicated this case with DISH and OPTDSH. As you might be aware, the structural code DISH, which analyzes the effects of ring deformation on the membrane, starts with a perfect parabola *before* stabilization pressure is applied. As you know, the unloaded membrane shape in your case is chosen to result in a perfect parabola *after* being pressure stabilized. This situation can be modeled to good approximation however, by applying a slight edge pull to the membrane bringing it back to a parabolic shape while under stabilization pressure. This edge pull can be calculated and is known as the membrane solution displacement. It is covered in Balch's papers on the subject. I believe we have provided you with copies of these at some time in the past. If not, let me know and I can send them to you.

This baseline case was then modeled with DISH and the output analyzed with OPTDSH. I used the system characteristics which you provided: 2.5 mr slope error, 1.5 mr specularity error, 82% reflectivity, 10% blockage, direct normal flux of 1050 W/m^2, and 750 ^oC receiver temperature. In addition, a standard gaussian sun size of 2.73 mr was used. The spot diagram at the target plane (or receiver aperture) and a plot of the thermal (or collector) efficiency are provided in the first two graphics. A maximum performance of 66.3% was obtained at an aperture radius of 0.13 m. In your letter you mentioned a 65.4% efficiency at a 0.34 m aperture diameter or 0.17 m aperture radius. It was not clear whether this represented the optimum case or a set receiver aperture. The OPTDSH results show a 63.8% efficiency at 0.17 m aperture radius. In any event, given the different modeling procedures, I believe the agreement is quite good. Also, emphasis should be placed on the performance difference between the baseline and the deformed case, not on the absolute numbers. To assure that this DISH modeled membrane shape is a good parabolic approximation, I used OPTDSH to analytically model the perfect parabola with the same set of random optical errors. The two performance curves were basically identical.

Having established the baseline case, the finite element displacement data were then fit to arrive at the Fourier coefficients required by the DISH program. Only the Z and R displacements were fit as we discussed over the telephone. This turned out not to be a problem. The effect of the rotations and the circumferential displacements would be relatively insignificant compare to that of the Z and R displacements. The DISH output was then analyzed again with OPTDSH and the results shown in the next two figures.

The spot diagram shows that most of the distortion occurs near the edge as one would expect. Since the Z displacement tracks the R displacement, more or less, and the periodicity of the displacements is approximately n=2, the spot at the target plane shows the two distinct lobes at 0^{o} and 180^{o} and the secondary lobes at 90^{o} and 270^{o} which would result. Only rays reflected from the outer region of the dish between 4.16 m radius and 5.20 m radius are effected. One can overlay the two spot diagrams to make this even more apparent. In fact, although the resolution of the plot legend does not show this, the DISH analysis shows that the decay distance for these edge effects is on the order of 0.4 m. In other words, the distortions die away within 0.4 m of the ring. This 0.4 m wide zone, however represents 14 % of the mirror area and thus it does have an effect on the overall performance of the dish. The overall thermal efficiency decreased from 63.8% at 0.17 m aperture radius to 59.7%.

I hope this analysis meets your needs. If you have any questions or would like to discuss the analysis further, please do not hesitate to call me.

Sincerely,

Tim Wendelin

Tim Wendelin

Enclosure: As stated.

SKI dish; no ring deformation

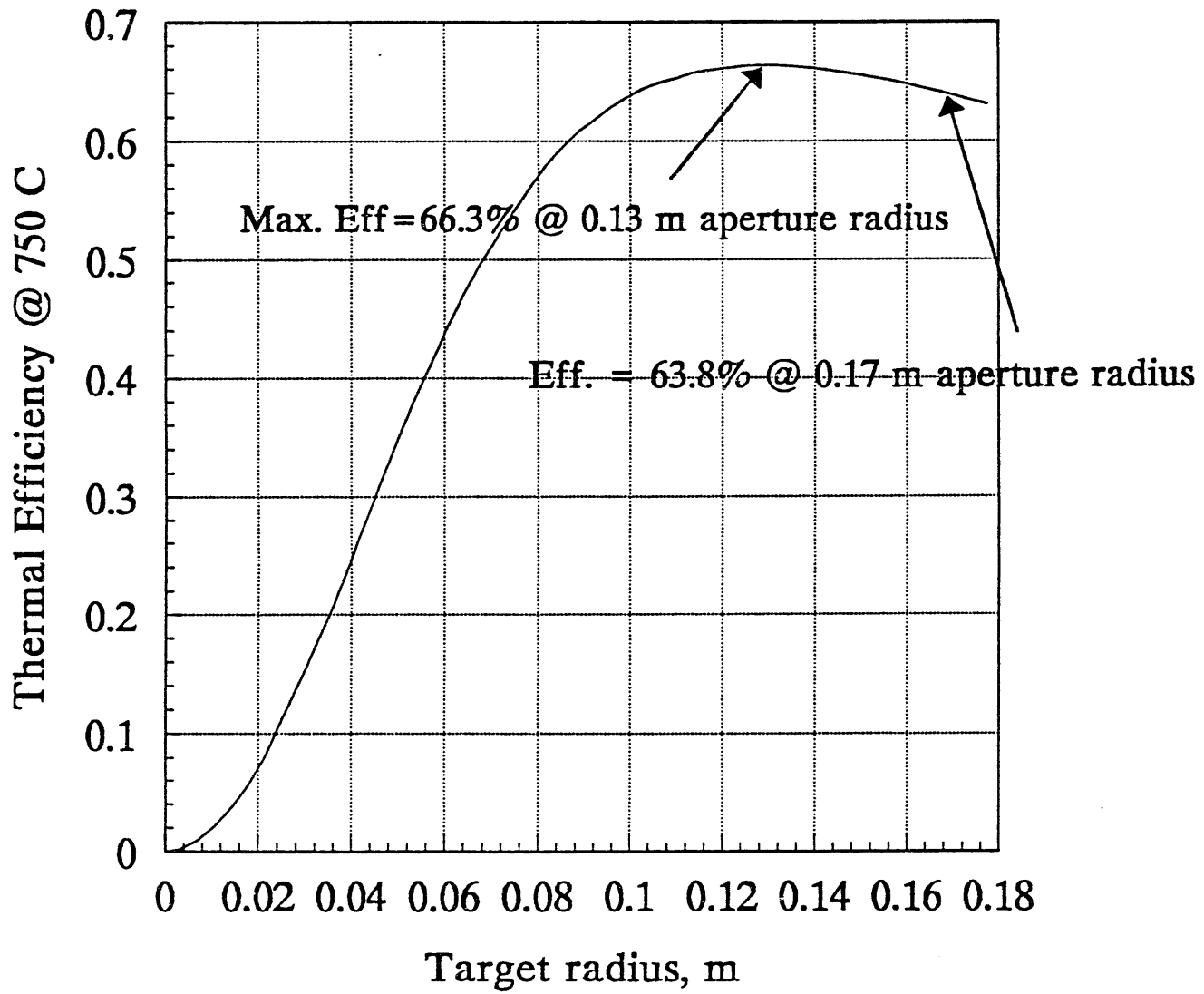

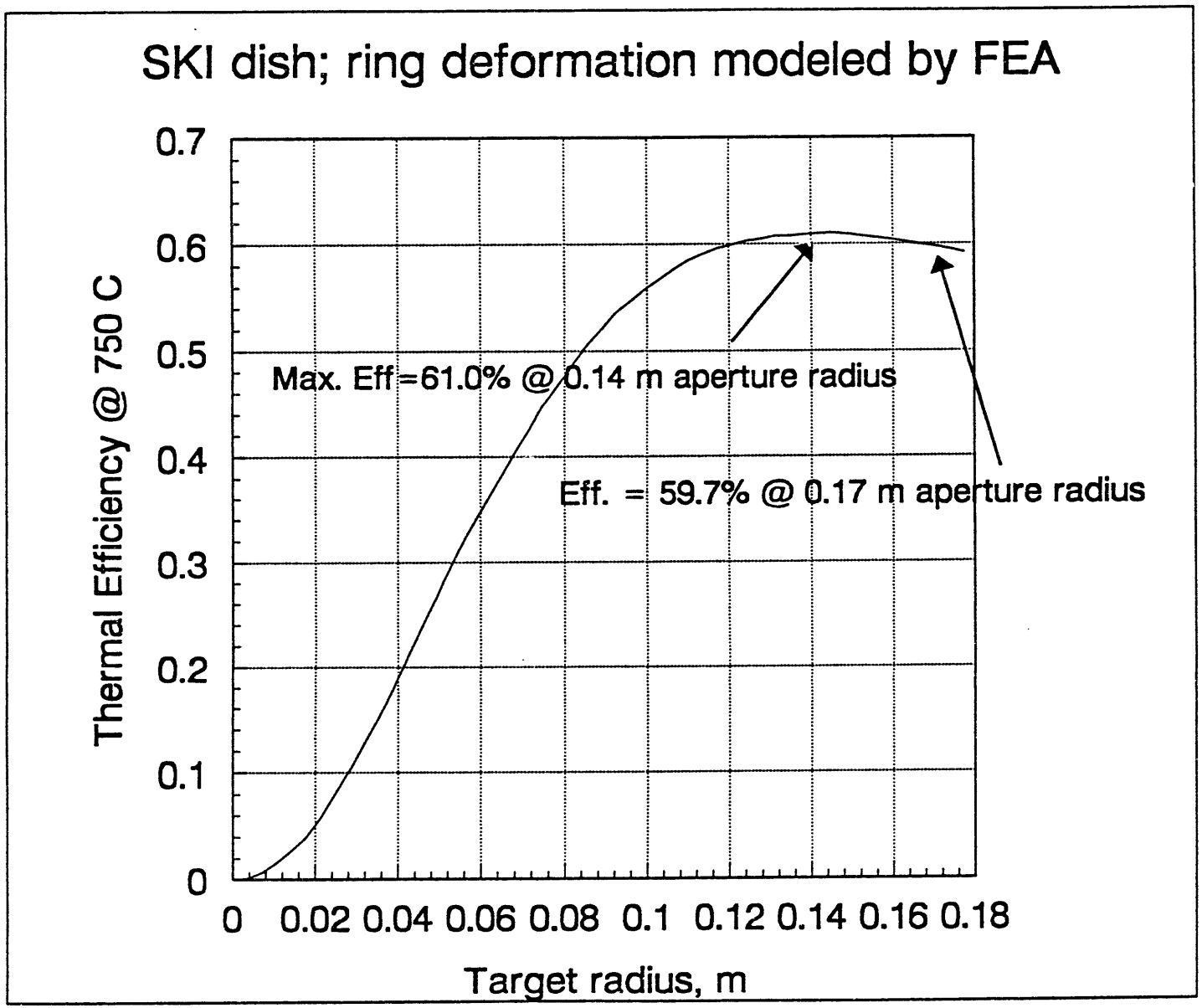
SKI dish; ring deformation modeled by FEA
Thermal Efficiency @ 750 C
0.7
0.6
0.5
0.4
0.3
0.2
0.1
0
Max. Eff=61.0% @ 0.14 m aperture radius
Eff. = 59.7% @ 0.17 m aperture radius
0 0.02 0.04 0.06 0.08 0.1 0.12 0.14 0.16 0.18
Target radius, m

SKI dish; membrane solution (i.e. parabola); no ring deformations.

Optical Performance

R	Eff.
.0000	.0000
.0035	.0025
.0071	.0097
.0106	.0218
.0142	.0378
.0177	.0565
.0213	.0814
.0248	.1126
.0284	.1432
.0319	.1742
.0355	.2060
.0390	.2418
.0426	.2793
.0461	.3158
.0497	.3534
.0532	.3871
.0568	.4201
.0603	.4514
.0639	.4816
.0674	.5088
.0710	.5333
.0745	.5564
.0781	.5785
.0816	.5996
.0852	.6164
.0887	.6316
.0923	.6438
.0958	.6555
.0994	.6659
.1029	.6749
.1065	.6822
.1100	.6875
.1136	.6950
.1171	.6994
.1207	.7039
.1242	.7080
.1278	.7115
.1313	.7144
.1349	.7162
.1384	.7180
.1420	.7192
.1455	.7202
.1491	.7211
.1526	.7217
.1562	.7225
.1597	.7229
.1633	.7232
.1668	.7235
.1704	.7237
.1739	.7238
.1775	.7239

SKI dish; membrane solution (i.e. parabola); no ring deformations.

Thermal Performance

R	Eff.
.0000	.0000
.0035	.0024
.0071	.0096
.0106	.0215
.0142	.0372
.0177	.0555
.0213	.0800
.0248	.1108
.0284	.1408
.0319	.1712
.0355	.2022
.0390	.2373
.0426	.2739
.0461	.3095
.0497	.3460
.0532	.3787
.0568	.4105
.0603	.4405
.0639	.4695
.0674	.4953
.0710	.5183
.0745	.5398
.0781	.5604
.0816	.5797
.0852	.5948
.0887	.6082
.0923	.6184
.0958	.6282
.0994	.6366
.1029	.6433
.1065	.6485
.1100	.6515
.1136	.6566
.1171	.6586
.1207	.6606
.1242	.6622
.1278	.6630
.1313	.6631
.1349	.6621
.1384	.6610
.1420	.6593
.1455	.6572
.1491	.6550
.1526	.6524
.1562	.6500
.1597	.6470
.1633	.6439
.1668	.6407
.1704	.6374
.1739	.6339
.1775	.6303

SKI dish; membrane solution + ring deformation modeled with FEA

Optical Performance

R	Eff.
.0000	.0000
.0035	.0009
.0071	.0063
.0106	.0163
.0142	.0283
.0177	.0409
.0213	.0593
.0248	.0823
.0284	.1055
.0319	.1310
.0355	.1564
.0390	.1858
.0426	.2180
.0461	.2464
.0497	.2772
.0532	.3074
.0568	.3363
.0603	.3605
.0639	.3871
.0674	.4122
.0710	.4375
.0745	.4634
.0781	.4845
.0816	.5048
.0852	.5260
.0887	.5427
.0923	.5605
.0958	.5736
.0994	.5873
.1029	.5983
.1065	.6104
.1100	.6207
.1136	.6291
.1171	.6366
.1207	.6424
.1242	.6487
.1278	.6531
.1313	.6586
.1349	.6613
.1384	.6658
.1420	.6696
.1455	.6727
.1491	.6746
.1526	.6764
.1562	.6778
.1597	.6796
.1633	.6808
.1668	.6818
.1704	.6834
.1739	.6846
.1775	.6855

SKI dish; membrane solution + ring deformation modeled with FEA

Thermal Performance

R	Eff.
.0000	.0000
.0035	.0009
.0071	.0062
.0106	.0160
.0142	.0277
.0177	.0399
.0213	.0579
.0248	.0805
.0284	.1031
.0319	.1279
.0355	.1526
.0390	.1813
.0426	.2126
.0461	.2401
.0497	.2699
.0532	.2990
.0568	.3267
.0603	.3496
.0639	.3750
.0674	.3987
.0710	.4225
.0745	.4469
.0781	.4663
.0816	.4850
.0852	.5044
.0887	.5193
.0923	.5352
.0958	.5463
.0994	.5579
.1029	.5668
.1065	.5766
.1100	.5847
.1136	.5908
.1171	.5958
.1207	.5991
.1242	.6028
.1278	.6046
.1313	.6073
.1349	.6072
.1384	.6088
.1420	.6096
.1455	.6097
.1491	.6085
.1526	.6071
.1562	.6052
.1597	.6037
.1633	.6015
.1668	.5991
.1704	.5971
.1739	.5947
.1775	.5919

SKI dish; membrane solution + ring deformation modeled with FEA
Dish Radius= 5.20; Focal Length= 6.24; Target Distance= 6.24

# RAYS:
Traced=10000
Reflected=10000
Showing=10000

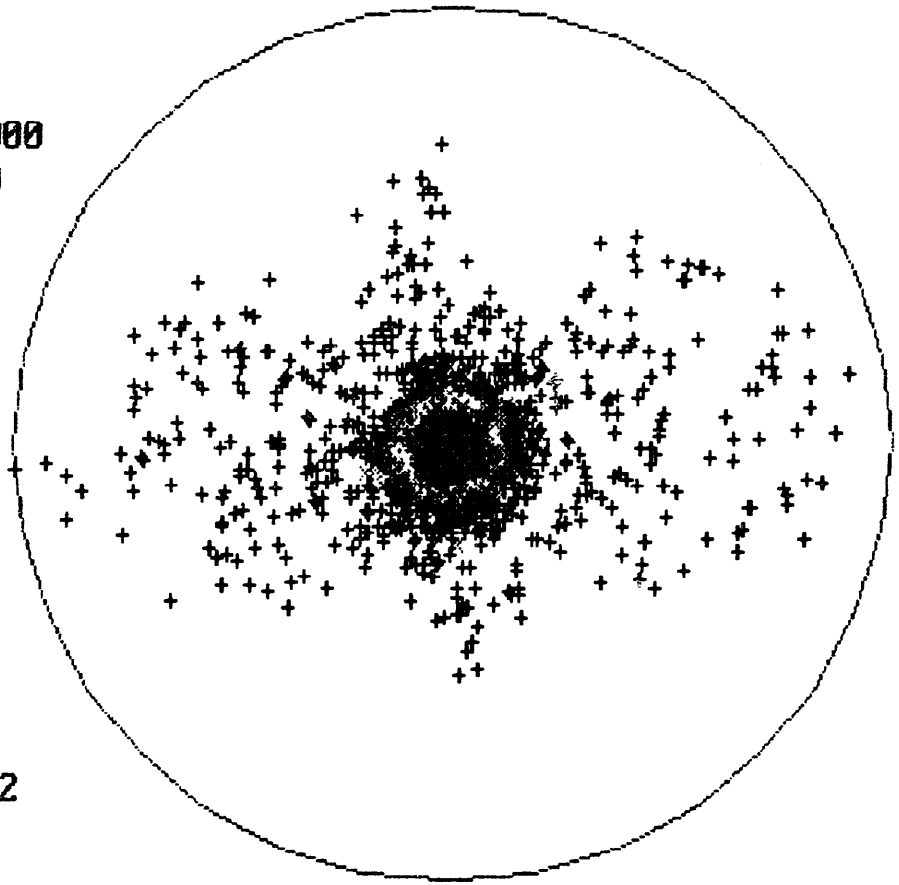

\+ 5.20 - 4.16
x 4.16 - 3.12
□ 3.12 - 2.08
* 1.04 - .00

IGRID=-1
NR= 0
NT= 1

ISEED= -123
MAX RAD= .972

RAD= .972; RMS RAD= .118; RMS DEV= .087

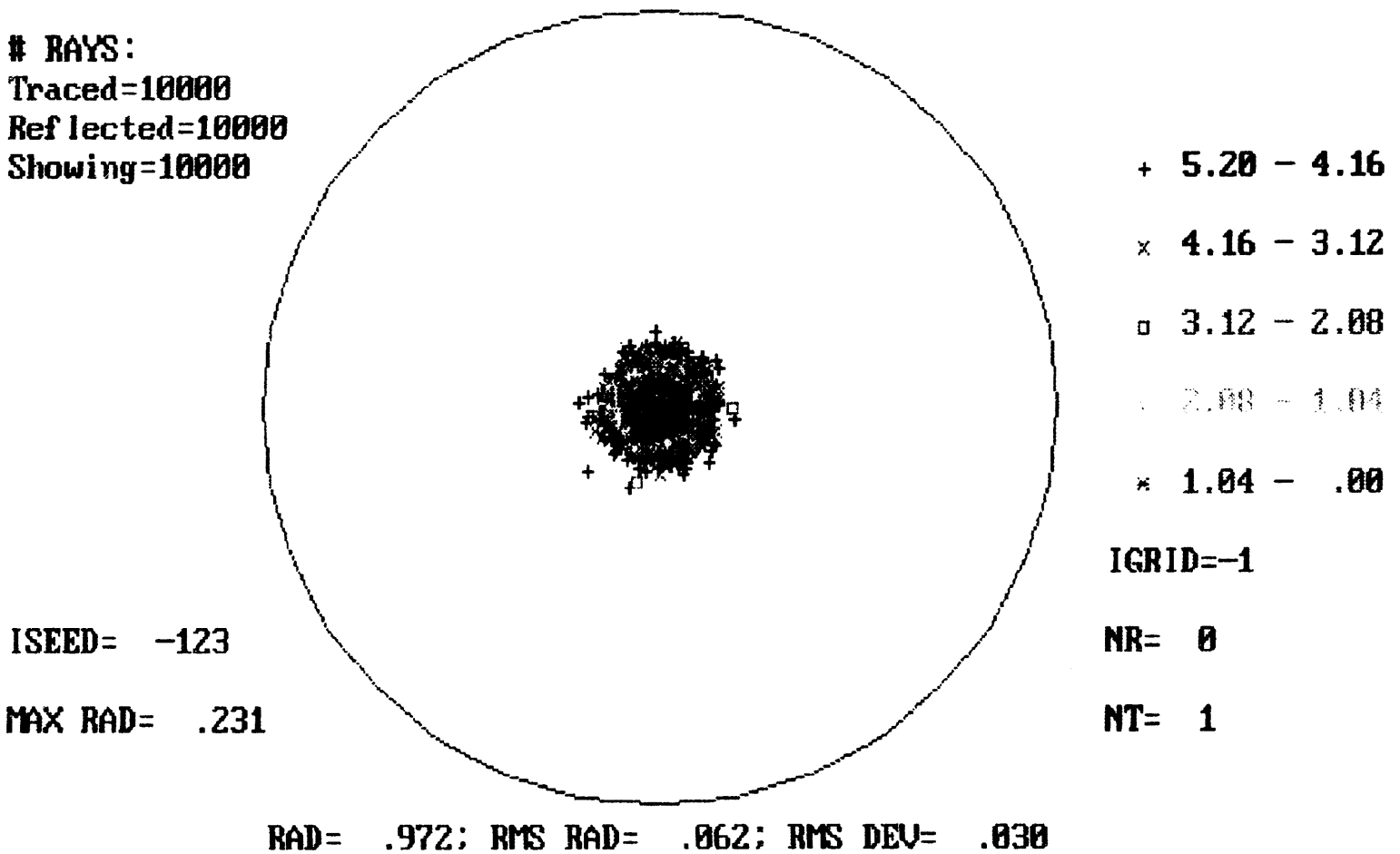
SKI dish; membrane solution (i.e. parabola); no ring deformations.
Dish Radius= 5.20; Focal Length= 6.24; Target Distance= 6.24
# RAYS:
Traced=10000
Reflected=10000
Showing=10000
+ 5.20 - 4.16
x 4.16 - 3.12
□ 3.12 - 2.08
2.08 - 1.04
* 1.04 - .00
IGRID=-1
ISEED= -123
NR= 0
MAX RAD= .231
NT= 1
RAD= .972; RMS RAD= .062; RMS DEV= .030

UNLIMITED RELEASE
INITIAL DISTRIBUTION

U.S. Department of Energy (5)
Forrestal Building
Code EE-132
1000 Independence Avenue, SW
Washington, DC 20585
Attn: G. Burch
S. Gronich

U.S. Department of Energy (2)
Forrestal Building
Code EE-13
1000 Independence Avenue, SW
Washington, DC 20585
Attn: R. Annan

U.S. Department of Energy (2)
Albuquerque Operations Office
P.O. Box 5400
Albuquerque, NM 87115
Attn: G. Tennyson
N. Lackey

U.S. Department of Energy
San Francisco Operations Office
1333 Broadway
Oakland, CA 94612
Attn: R. Hughey

Arizona Dept. of Commerce
3800 N. Central, Suite 1200
Phoenix, AZ 85012
Attn: F. Mancini

Battelle Pacific Northwest Laboratory
P.O. Box 999
Richland, WA 99352
Attn: D. Brown

California Polytechnic University
Dept. of Mechanical Engineering
3801 West Temple Avenue
Pomona, CA 91768
Attn: Dr. Wm. B. Stine (10)

Central and Southwest Services
Mail Stop 7RES
1616 Woodall Rogers Freeway
Dallas, TX 75202
Attn: Edward L. Gastineau

Clever Fellows
Innovation Consortium, Inc.
R.D. 1, Box 410, River Road
Melrose, NY 12121
Attn: J. A. Corey, P.E.

Cummins Power Generation (2)
MC 60125
P. O. Box 3005
Columbus, IN 47202-3005
Attn: R. Kubo

Cummins Power Generation South
150 Tannehill Drive
Abilene, TX 79602
Attn: M. McGlaun

Dynatherm Corporation
1 Beaver Court
P.O. Box 398
Cockeysville, MD 21030
Attn: David Wolf

Electric Power Research Institute
P.O. Box 10412
Palo Alto, CA 94303
Attn: J. Schaeffer

Energy Technology Engr. Center (2)
Rockwell International Corp.
P. O. Box 1449
Canoga Park, CA 91304
Attn: W. Bigelow
R. LeChevalier

Karl Thomas Feldman, Jr. Ph.D., P.E.
Mechanical Engineering Consultant
1704 Stanford Dr. NE
Albuquerque, NM 87106

Florida Solar Energy Center
300 State Road, Suite 401
Cape Canaveral, FL 32920
Attn: Library

Georgia Power
7 Solar Circle
Shenandoah, GA 30265
Attn: W. King

Institute of Gas Technology
34245 State Street
Chicago, IL 60616
Attn: Library

Jet Propulsion Laboratory
4800 Oak Grove Drive
Pasadena, CA 91109
Attn: M. Alper

Lawrence Berkeley Laboratory
MS 90-2024
One Cyclotron Road
Berkeley, CA 94720
Attn: A. Hunt

Los Alamos National Laboratory
MS-E13
Los Alamos, NM 87545
Attn: M. Merrigan

McDonnell-Douglas Astronautics Company
5301 Bolsa Avenue
Huntington Beach, CA 92647
Attn: R. L. Gervais,
J. Rogan,
D. Steinmeyer

Mechanical Technology, Inc. (2)
968 Albany Shaker Road
Latham, NY 12110
Attn: G. Dochat
J. Wagner

NASA Lewis Research Center (4)
21000 Brook Park Road
Cleveland, OH 44135
Attn: R. Shaltens
J. Schrieber

National Renewable Energy Laboratory (6)
1617 Cole Boulevard
Golden, CO 80401
Attn: T. Williams
L. M. Murphy
G. Jorgensen
T. Wendelin
A. Lewandowski
M. Bohn

Northern Research and Engineering Corp.
39 Olympia Avenue
Woburn, MA 01801-2073
Attn: J. Kesseli

Power Kinetics, Inc.
415 River Street
Troy, NY 12180-2822
Attn: W. E. Rogers

Research International
18706 142nd Avenue NE
Woodinville, WA 98072
Attn: E. Saaski

Science Applications International Corporation
15000 W. 6th Avenue, Suite 202
Golden, CO 80401
Attn: Kelly Beninga

Science Applications International Corporation
Mail Stop 32
10260 Campus Point Court
San Diego, CA 92121
Attn: B. Butler

Solar Energy Industries Assoc. (2)
777 North Capitol St. NE
Suite 805
Washington, D.C. 20002
Attn: S. Sklar
K. Sheinkopf

Solar Kinetics, Inc. (2)
P.O. Box 540636
Dallas, TX 75354-0636
Attn: J. A. Hutchison
P. Schertz

Stirling Technology Company (3)
2952 George Washington Way
Richland, WA 99352
Attn: Maurice A. White

Stirling Thermal Motors (2)
275 Metty Drive
Ann Arbor, MI 48103
Attn: Lennart Johansson

Stirling Machine World
1823 Hummingbird Court
West Richland, WA 99352-9542
Attn: Brad Ross

Sunpower, Inc.
6 Byard Street
Athens, OH 45701
Attn: W. Beale

Tech Reps, Inc. (2)
5000 Marble NE, Suite 222
Albuquerque, NM 87110
Attn: J. Stikar

Thermacore, Inc. (2)
780 Eden Road
Lancaster, PA 17601
Attn: Donald Ernst

University of Houston
Solar Energy Laboratory
4800 Calhoun
Houston, TX 77704
Attn: J. Richardson

University of Minnesota
Dept. of Mechanical Engineering
111 Church St., SE
Minneapolis, MN 55455
Attn: E. A. Fletcher

Australian National University
Department of Engineering
Physics
P. O. Box 4
Canberra ACT 2600 AUSTRALIA
Attn: S. Kaneff

DLR
Pfaffenwaldring 38-40
7000 Stuttgart 80 GERMANY
Attn: R. Buck

Energy Research Centre
R. S. Phy. Sc.
Australian National University
Canberra ACT 2601 AUSTRALIA
Attn: K. Inall

Dr. David Hagen
134 Kitchener St.
Garran, ACT 2605
AUSTRALIA

Pacific Power
Park and Elizabeth Streets
GPO Box 5257, Sydney
New South Wales 2001, Australia
Attn: Peter Lynch

Schlaich, Bergermann & Partner
Hohenzollernstr. 1
D - 7000 Stuttgart 1 GERMANY
Attn: W. Schiel

1513	D. R. Adkins
1513	R. E. Hogan
1513	V. J. Romero
1513	R. D. Skocypec
1561	E. L. Hoffman
1561	C. M. Stone
1833	J. A VanDenAvyle
2756	G. S Phipps
4313	J. F.Muir
6000	D. L.Hartley
6115	W. C. Ginn
6200	D. E. Arvizu
6201	P. C. Klimas
6213	A. R. Mahoney
6215	C. P.Cameron
6215	K. S .Rawlinson
6215	Library (5)
6216	C. E.Tyner
6216	C. E.Andraka
6216	R. B.Diver
6216	T. R.Mancini
6216	D. F. Menicucci
6216	J. B. Moreno
6216	T. A. Moss
6216	Library (5)
7141	Technical Library (5)
7151	G. C. Claycomb
7613-2	Document Processing for DOE/OSTI (10)
8523-2	Central Technical Files

☆ U.S. Government Printing Office 1994-573-110-02058

END

DATE
FILMED
5/4/94